Comparative Study between Steel-Free and Steel Reinforced Concrete Bridge Deck Slabs Subjected to Fatigue Loading

By:

Cody Scaletta

A Thesis Submitted to the Faculty of Graduate Studies of

The University of Manitoba

in partial fulfilment of the requirements for the degree of

Master of Science

Department of Civil Engineering

Faculty of Engineering

University of Manitoba

Winnipeg, Manitoba, Canada

This Thesis is dedicated to my grandfather, August Scaletta, for all the time we've spent together, whether it be gardening, working in the garage, or picking blueberries, but most of all for always teaching me that nothing is impossible.

Abstract

This experimental program was designed to provide increasing evidence that second generation steel-free concrete bridge decks are a practical alternative to conventional steel reinforced concrete bridge decks. The bridge deck in this experiment was cast monolithically with one half consisting of a second generation steel-free concrete bridge deck and the second half a conventional steel reinforced concrete bridge deck. A constant cyclic load was applied to each segment at an identical magnitude to compare the two bridge decks in terms of endurance, durability, deflection, crack width, reinforcement strain, concrete strain, and overall performance.

The test results obtained in this experimental program confirm the notion that second generation steel-free concrete bridge decks are a safe and reliable alternative to conventional steel reinforced concrete bridge decks, and furthermore should become more widely accepted and practiced in the field of bridge engineering. The mode of failure for both segments was punching shear failure.

Acknowledgements

Above and beyond all I would like to thank my advisor Dr. Aftab Mufti for providing me with this opportunity of a lifetime, and for teaching me to always seek new challenges and achieve higher levels. I would also like to thank him for his advice, encouragement, and continual support throughout my graduate studies, and undergraduate studies. And not to mention the significant financial support required to make a project of this magnitude possible.

I would also like to throw a huge thank you to Chad Klowak, the University of Manitoba W.R. McQuade Heavy Structures Laboratory Manager, for the endless contributions he offered to ensure this project was a success. I am also grateful for all the assistance I received from the technical staff of the W.R. McQuade Heavy Structures Laboratory, namely, Mr. Grant Whiteside. A noteworthy thank you also goes out to Mr. Timothy Reeve, a fellow student at the U of M, for assisting in the installation of dozens of instruments and gauges throughout the project. Mrs. Charleen Choboter was also extremely helpful with all the coordination and paperwork that was involved in this project.

Finally, I would like to thank my mother, Julie Scaletta, for providing me with a roof over my head and keeping this hungry student well fed throughout my many years of university; as well as my father, Curtis Baylak, for the financial support that helped this once poor student through two engineering degrees.

Table of Contents

Table of Figures

Table of Tables

Chapter 1

Introduction

1.1 General

It is now well established that reinforcing concrete bridge decks with steel can have severe consequences. In particular, the Canadian climate can be very unforgiving. Winter conditions can leave ice covered bridges and unsafe conditions. The most cost effective method to deter ice is to use de-icing chemicals, however, small cracks in bridge decks act as an opening for the de-icing chemicals to enter and cause havoc. Chloride, which is present in de-icing chemicals, is very aggressive towards unprotected steel. When steel is exposed to chloride, oxidation occurs and causes the steel to corrode, more commonly known as rusting. Corrosion decreases the net cross-sectional area of the steel reinforcement, weakening the bond with the surrounding concrete. The gross cross-sectional area, i.e. steel plus rust, on the other hand expands and causes the concrete to swell and eventually crack. These cracks rapidly decrease the durability of the concrete, which leads to further crack propagation. The resulting inadequacy in strength of the steel can eventually lead to mechanical failure. These safety concerns usually lead to costly maintenance repairs. To add to the issue, corrosion of steel is not the only culprit for concrete cracking, as cracks can appear due to concrete shrinkage during curing, and large variations in temperature.

In the early 1990's, a group of Canadian researchers developed a state of the art method, coined "first generation steel-free bridge decks", to eliminate the corrosion issues related to internally reinforced concrete bridge decks. [Mufti et al., (1993)] demonstrated that it was entirely possible to reinforce concrete bridge decks externally, allowing for the complete elimination of internal reinforcement. In order

to subdue thermal and shrinkage cracks, relatively inexpensive low modulus fibres such as polypropylene were mixed in with the concrete during mixing. This concept brought many advantages to the table, including lower construction costs, improved durability and lower maintenance costs.

Over the course of five years (1995-1999), four highway bridges, one forestry bridge and one wharf were designed and constructed using the steel-free concept. Structurally and durability wise, the structures have performed very well, however several minor serviceability issues such as the appearance of rather large longitudinal cracks in the central soffit region of some of the decks, due to vehicular traffic, compelled researchers to reevaluate the steel-free concept. [Memon, (2003)] discovered that the addition of two layers of orthogonally placed glass fibre reinforced polymer (GFRP) grids was sufficient to minimize shrinkage, thermal and fatigue induced cracks to within an acceptable margin as governed by standard reinforced concrete limits. This new development in steel-free bridge deck design was coined “second generation steel-free bridge decks” due to its addition of GFRP crack control grids.

1.2 Concept

A steel-free concrete bridge deck is one that is completely devoid of internal steel reinforcement and responds to loading in an arching fashion rather than traditional flexure. In order to understand the behavior of a steel-free bridge deck, consider the section shown in Figure 1.1. Note that the common method to describe the orientation of a bridge deck is to refer the flow of traffic as the longitudinal direction, while the transverse direction is considered perpendicular to the flow of traffic.

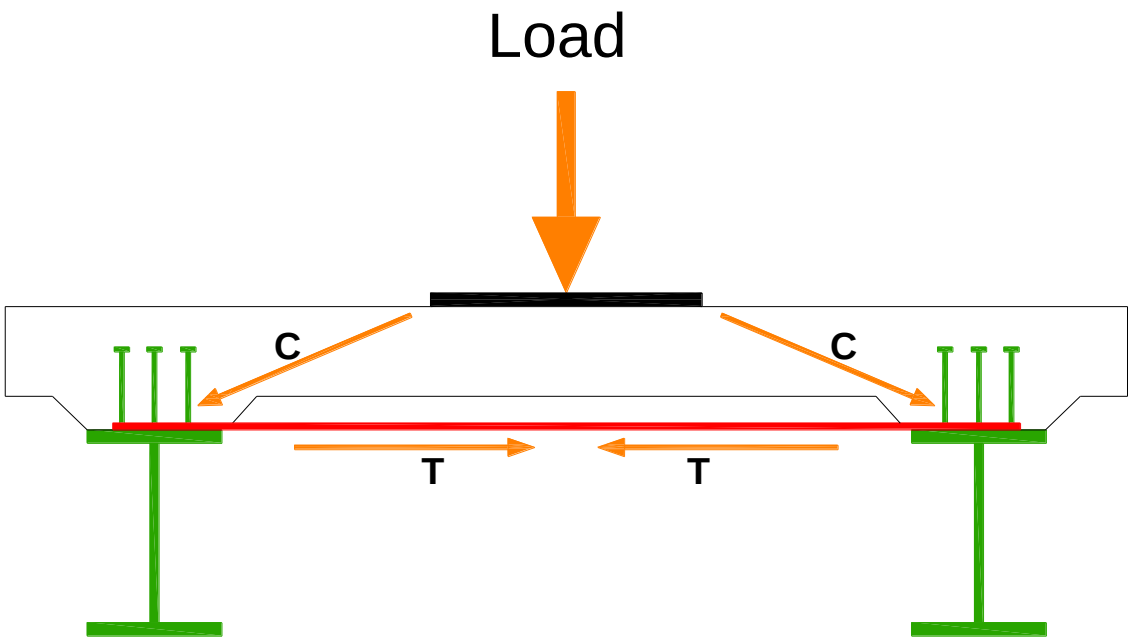

Figure 1.1 Arching action in a steel-free bridge deck slab under concentrated load

The development of internal arching action is highly dependent on the confinement provided in the longitudinal direction and the lateral restraint provided in the transverse direction of a concrete deck. A slab-on-girder system comprises of a monolithic concrete slab and at least two adjacent parallel girders. Confinement in the longitudinal direction is obtained when the slab and girders are made composite through the use of shears studs. When wheel loads are applied to a bridge deck, the load transfers from the deck to the girders. Initially, the bending of the deck causes the girders to rotate outwards in the transverse direction, as shown in Figure 1.2. By installing transverse steel straps to the top flange of the girders through means of welding or partial studs, outward rotation of the girders is restricted and lateral restraint is provided. Although the greatest percentage of lateral restraint is linked to the steel straps, a substantial portion is also contributed through the beam like behavior of the top flange of the girders. Finally, when the wheel load exceeds the ultimate capacity or fatigue life of the deck, a cone shaped portion of concrete roughly the size of the contact area of a wheel punches through the deck and signifies failure.

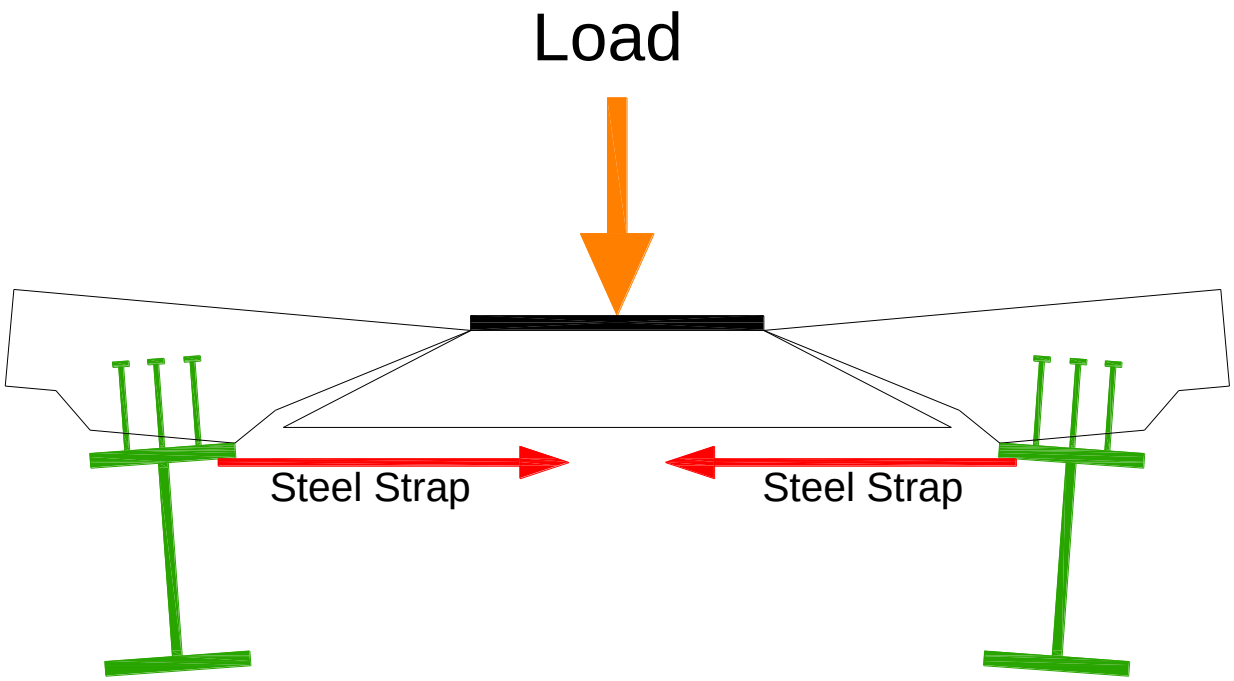

Figure 1.2 Girder rotation in a steel-free bridge deck slab under concentrated load

The events leading to the failure of a steel-free concrete bridge deck can be simplified as follows:

1. Vehicles travel over the bridge and apply direct wheel loads to the surface of the deck.
2. The load travels directly from the wheels, through the concrete and to the girders in the form of compression.
3. The load than transfers from the concrete to the shear studs, which forces the top flanges of the adjacent girders to rotate outwards.
4. The outward rotation of the flanges causes the attached welded or partially studded transverse steel straps to counteract in tension.
5. Once the concrete is in compression and the steel straps are in tension, the structure acts predominantly as an arch.
6. When the applied loading exceeds the ultimate capacity or fatigue life of the deck, failure in the form of a shear punch cone occurs.

1.3 Purpose of this Study

This study was developed to compare the following two Canadian Highway Bridge Design Code (CAN/CSA-S6-00) designed concrete bridge decks under identical fatigue loading,

1) Conventional steel reinforced concrete bridge deck, and
2) Steel-free concrete bridge deck (second generation steel-free concrete bridge deck),

for the purpose of determining if the steel-free concrete bridge deck design is equivalent and/or superior in nature in terms of endurance, durability, deflection, crack width, reinforcement strain, concrete strain, and overall performance. With limit states design criteria in mind, a second comparison is sought to ensure that both designs meet serviceability and ultimate limit state criteria as presented in the CAN/CSA-S6-00. In order to maintain relevancy with more recent design codes, the test results from both bridge decks will be compared with the serviceability and ultimate limit state design requirements found in the CAN/CSA-S6-06. When limit state design requirements are not provided in the CAN/CSA-S6-00/06, design limits from the American Concrete Institute (ACI 440.1R-01), and the ISIS Canada Research Network Design Manual No. 3 (Reinforcing Concrete Structures with Fibre Reinforced Polymers) are referenced.

1.4 Research Objectives and Scope

The main objective of this program is to confirm that the overall performance of the CAN/CSA-S6-00 designed steel-free concrete bridge decks match or exceed that of the CAN/CSA-S6-00 conventionally designed steel reinforced concrete bridge decks, under the exact same fatigue loading scheme and magnitude. While doing so, this program also intends to subject both bridge decks to specified design loads and check the test results, in terms of maximum deflection, maximum crack width, maximum reinforcement strain, and maximum concrete strain, with corresponding Ultimate Limit State (ULS), Serviceability Limit State (SLS), and Fatigue Limit State (FLS) requirements laid out in the CAN/CSA-S6-00/06 design codes. When limit state design requirements are not provided in the CAN/CSA-S6-00/06,

design limits from the American Concrete Institute (ACI 440.1R-01), and the ISIS Canada Research Network Design Manual No. 3 (Reinforcing Concrete Structures with Fibre Reinforced Polymers) are referenced.

This program also serves as a testament to the conclusions found in similar comparison studies which used finite element analysis, PUNCH program software, and fatigue life estimation models to predict punching shear capacities, deflections, and fatigue life cycles for steel-free and conventional steel reinforced concrete bridge decks. On the other hand, this study is not designed to provide any new, or expand any existing, theoretical or experimental models. Albeit, this study does plan to use finite element analysis, and existing PUNCH program software and fatigue life estimation models, as a theoretical and experimental guide to develop a new test program that will provide valuable data, from two very carefully planned and monitored fatigue tests. The results will aim to provide evidence for the argument that steel-free concrete bridge decks are a comparable and/or superior design to conventional steel reinforced concrete bridge decks.

The concrete bridge deck developed in this study is designed in two sections so that only two tests can be performed in terms of internal panel fatigue loading. Due to the unpredictable nature of fatigue loading, each bridge deck will be allotted a certain time period or number of cycles to achieve failure. If failure is not reached within a reasonable time period or number of cycles, fatigue loading will cease, and the Segment will be tested to failure through incremental static loading.

Before testing, during loading, and after failure, there will be data, photos, and videos collected to ensure that both tests are accurately monitored for deflection, crack widths, reinforcement strains, concrete strains, and any other data and information that will provide for a meaningful and justifiable conclusion.

Chapter 2

Literature Review

2.1 Concrete Bridge Deck Slab Design Methods

Three concrete bridge deck slab design methods are discussed in this section:

1) Flexural Design Method
2) Empirical Design Method
3) Steel-Free Design Method

2.1.2 Flexural Design Method

Traditionally, concrete bridge deck slabs were designed based on flexural bending theory. This meant that concrete bridge deck slabs resting on two or more parallel girders would act in the same manner, in the deck's transverse direction, as a simply supported or continuously supported beam would under applied loading. Therefore, any load applied between two girders would contribute a positive bending moment to the central region of the deck and a negative bending moment over the girders. Furthermore, theory states that the "sagging" action created by positive bending moments would cause longitudinal cracks to develop on the soffit of the deck near the central region, while the "hogging" action due to negative bending moments would lead to the development of longitudinal cracks on the top surface of the deck over the girders, as shown Figure 2.1. In order to minimize or completely alleviate the longitudinal cracks mentioned above, steel reinforcement was strategically placed, as shown in Figure 2.2.

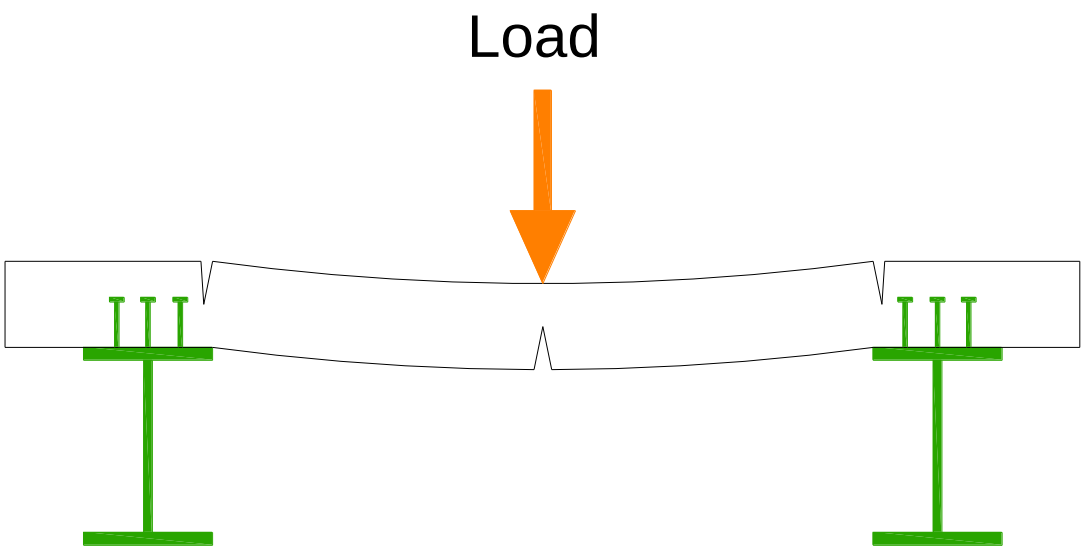

Figure 2.1 Longitudinal cracking in a flexural designed bridge deck slab under concentrated load

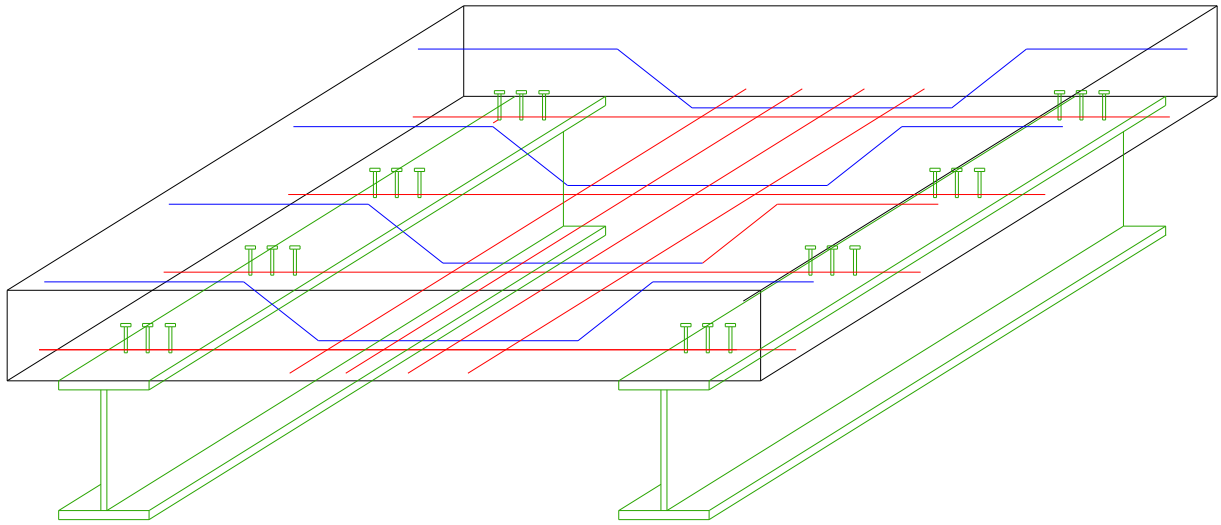

Figure 2.2 Typical bridge deck slab using flexural design method. Blue signifies top bent reinforcement, red signifies bottom reinforcement

The flexural design method was used for many slab-on-girder bridge decks throughout the early and mid-twentieth century and over time has proven to be a safe and reliable design. The American Association of State Highway and Transportation Officials (AASHTO), as well as the Canadian Highway Bridge Design Code (CAN/CSA-S6-06) still offer the flexural design method as a viable design option. However, several disadvantages accompany this design including a significantly high reinforcement ratio of about 3.2% to 4.0% of the total volume of the concrete, which results in high material and construction costs.

2.1.3 Empirical Design Method

During the 1970's, extensive research undertaken by the Ministry of Transportation of Ontario and Queen's University lead to a completely new understanding of how composite slab-on-girder bridge deck systems respond to vehicular movement. During that period, highway bridges throughout Ontario were being permitted to support twice the maximum axle weights recommended by AASHTO and remarkably were fairing rather well. This prompted the Ministry of Transportation of Ontario to obtain a deeper understanding of the behavior and capacity of AASHTO-designed concrete bridge decks.

Experiments conducted at Queen's University lead researchers to believe that slab-on-girder bridge decks failed not in flexure, but rather in a localized punching manner, as shown in Figure 2.3. [Hewitt and Batchelor (1975)] presented evidence that slab-on-girder bridge decks, when properly confined, develop what is called "compressive membrane forces" directly under the load. Remarkably, these "compressive membrane forces" significantly enhance the deck's ultimate capacity. Previously unaware to designers, the bottom transverse reinforcement intended to resist tensile forces which concrete cannot, in addition act as a tie to facilitate arching behavior. However, through experimentation, it was shown the arching action is highly dependent on the confinement of the structure, thereby emphasizing the importance of constructing the deck and the girders as a composite system. In conclusion, the composite nature between the deck and girders, along with the tying action of the bottom transverse reinforcement,

combine to create a path for the load to travel from the point of application towards the girders and finally through the bottom reinforcement, thus initiating the arching action or otherwise coined “compressive membrane forces”, as illustrated in Figure 2.4.

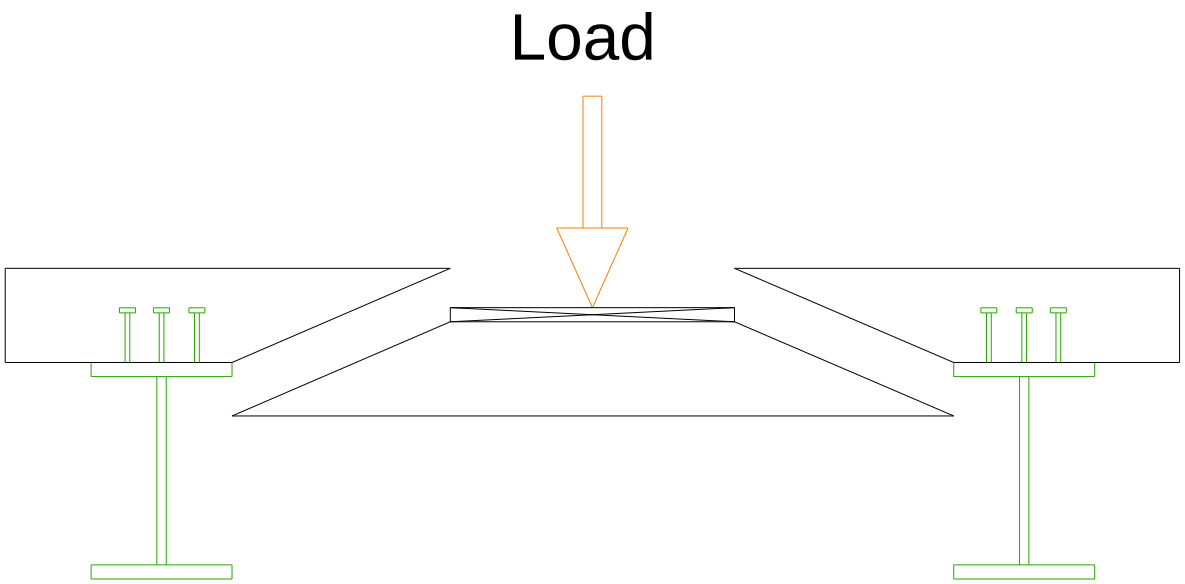

Figure 2.3 Punching shear failure in an empirically designed bridge deck slab under concentrated load

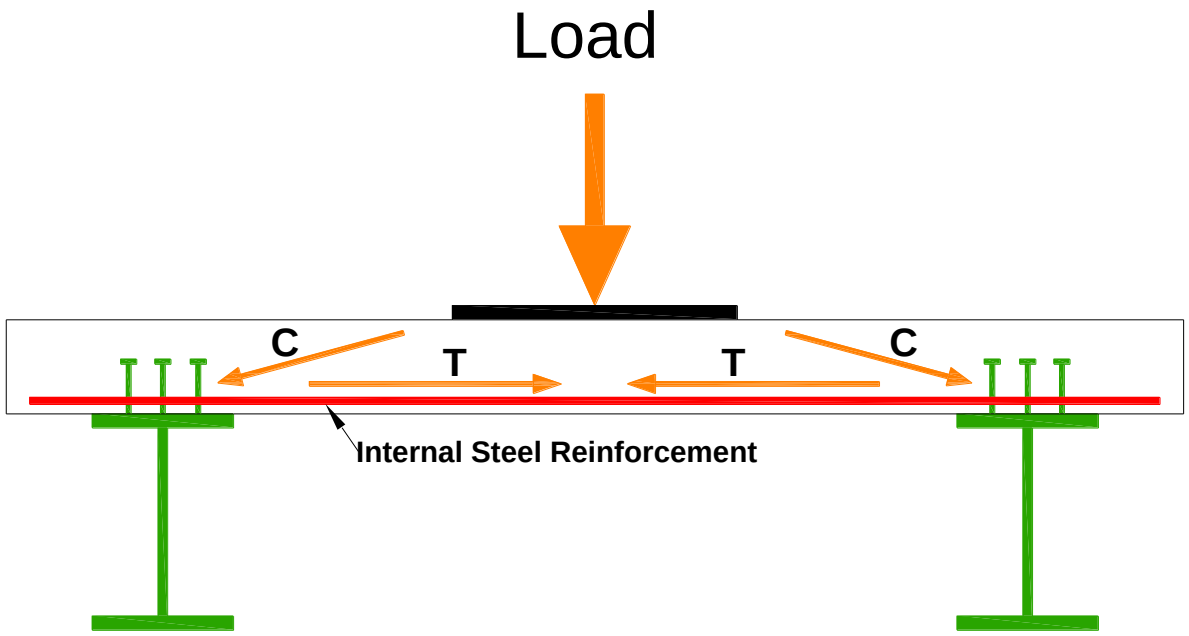

Figure 2.4 Arching action in a conventional steel reinforced bridge deck slab under concentrated load

[Dorton et al., (1977)] expanded the investigation by constructing a prototype test bridge. Evaluating varying slab thicknesses and reinforcement ratios under applied loading were among some of the focal points. It was established that a minimum of 1.2% total reinforcement distributed isotropically in four layers satisfied ultimate and serviceability requirements with a generous margin of safety. The research of [Hewitt and Batchelor (1975)] and [Dorton et al., (1977)], among others, motivated the Ontario Highway Bridge Design Code (OHBDC, 1979) to include provisions for the newly developed empirical design method. [Bakht and Markovic (1986)] prepared an exquisite, highly detailed report outlining all the past research and discoveries that ultimately lead to the development of the empirical design method. Figure 2.5 illustrates a schematic of an empirically designed slab-on-girder bridge deck.

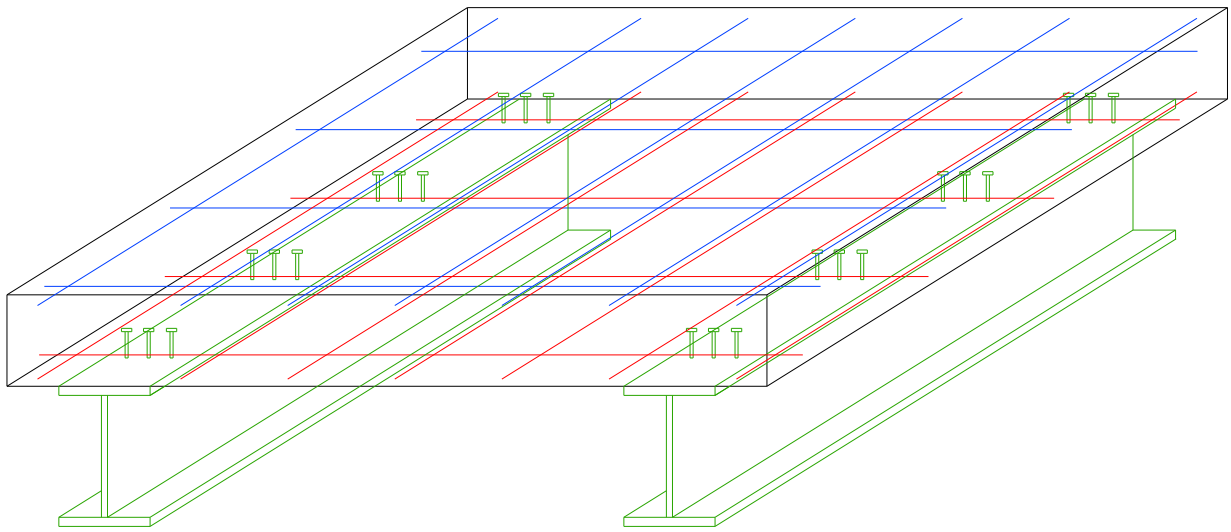

Figure 2.5 Typical bridge deck slab using empirical design method. Blue signifies top reinforcement, red signifies bottom reinforcement

2.1.4 Steel-Free Design Method

Following its inception into the Ontario Highway Bridge Design Code (1979), the empirical design method maintained superiority for many years due to its lower reinforcement ratios, easier construction and reduced costs. Unfortunately, because of extensive maintenance issues caused by internal steel corrosion, constant repairs to concrete decks began to outweigh the initial benefits of the empirical design method. By the early 1990's, researchers were once again in pursuit of a bridge deck design that was cost efficient, easy to construct and most importantly, could minimize or eliminate the costly inconvenience of internal steel corrosion. In order to avoid the corrosion concerns related to empirically designed bridge decks, [Mufti et al., (1991)] proposed a ground breaking new concept coined "steel-free bridge decks". Unlike the empirical design method, this design method did not require any internal steel reinforcement.

2.1.4.1 First Generation Steel-Free Bridge Deck Slabs

[Mufti et al., (1993)] demonstrated that compressive membrane forces are also present in composite slab-on-girder bridge decks that are reinforced with external transverse steel straps. The absence of internal steel reinforcement removes the tendency for corrosion to develop within the concrete. Steel free concrete bridge decks use the same arching behavior to resist loads as empirically designed decks, however, the method of confinement for the two differ in several aspects. Both the empirical and steel-free design methods require the concrete deck to be composite with the steel girders via shear studs; this creates the necessary confinement in the longitudinal direction. In addition, both methods require the concrete deck to be confined in the transverse direction; this is where the two methods differ. The empirical method uses internal steel reinforcement to establish arching behavior, while the steel-free method uses external transverse steel straps welded to the top flange of adjacent girders. Figure 2.6 demonstrates a steel-free bridge deck transversely reinforced with steel straps; notice the absence of internal steel reinforcement.

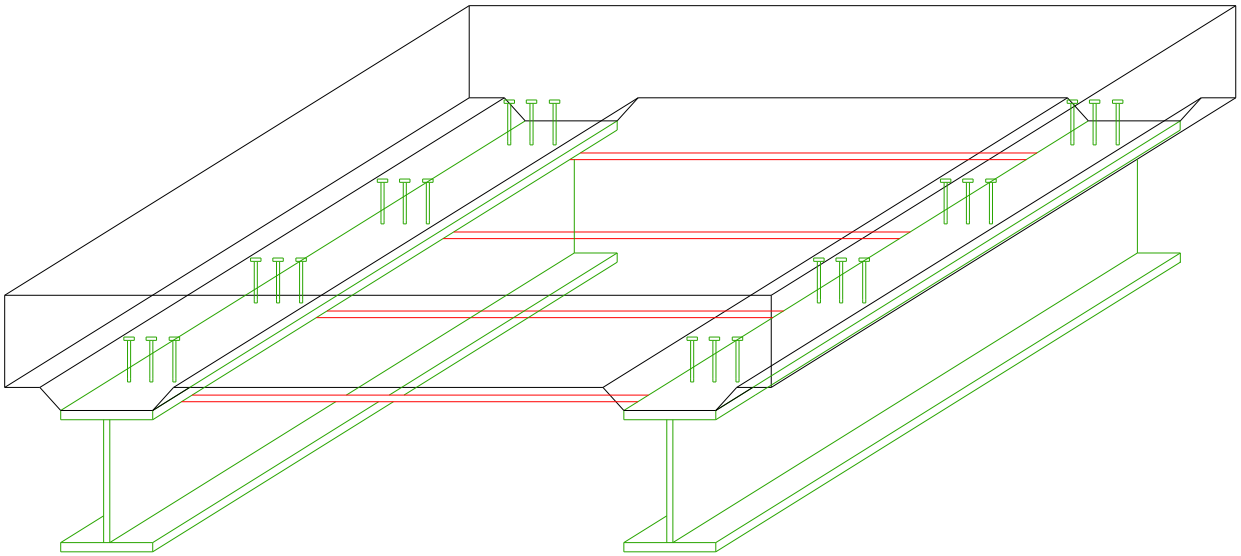

Figure 2.6 Typical bridge deck slab using first generation steel-free design method. Red signifies bottom transverse steel straps

First generation steel-free bridge deck slabs required low modulus fibres such as polypropylene to be added to the concrete mix to prevent shrinkage and thermal cracking. The Salmon River Bridge was the first field application of a steel-free bridge deck. It was constructed in 1995 on the Trans-Canada Highway in Nova Scotia. Shortly after the bridge was opened to traffic, approximately 1 mm wide longitudinal cracks started to develop on the soffit of each steel-free span, roughly in between the girders, [Mufti et al., (1999)]. Presumably the cracks formed as a direct result of fatigue due to vehicular movement. Besides creating public unease and being aesthetically unpleasing, the cracks do not pose any safety concerns, nor do they reduce the structural integrity of the structure. The incident lead researchers to speculate that a superior, more versatile secondary reinforcement was needed to prevent fatigue, shrinkage and thermal cracking; this lead to the development of second generation steel-free bridge deck slabs in the early 2000's. First generation steel-free bridge deck slab provisions were first added into the Canadian Highway Bridge Design Code (CAN/CSA-S6-00) in 2000.

2.1.4.2 Second Generation Steel-Free Bridge Deck Slabs

[Memon et al., (2003)] demonstrated that two layers of orthogonally placed glass fibre reinforced polymer (GFRP) grids satisfactorily controlled thermal, shrinkage and fatigue cracking. Figure 2.7 demonstrates a second generation steel-free bridge deck; notice the nominal addition of GFRP crack control grids. GFRP's main attributes include complete resistance to corrosion and similar modulus of elasticity values as concrete. [Memon (2005)] compared an empirically designed bridge deck slab versus a second generation steel-free bridge deck slab of equivalent ultimate capacity. The steel-free bridge deck with nominal crack control GFRP responded to several times more cycles than the empirically designed bridge deck under identical loading conditions. Provisions for the design of second generation steel-free bridge deck slabs can be found in Clause 16 of the Canadian Highway Bridge Design Code (CAN/CSA-S6-06).

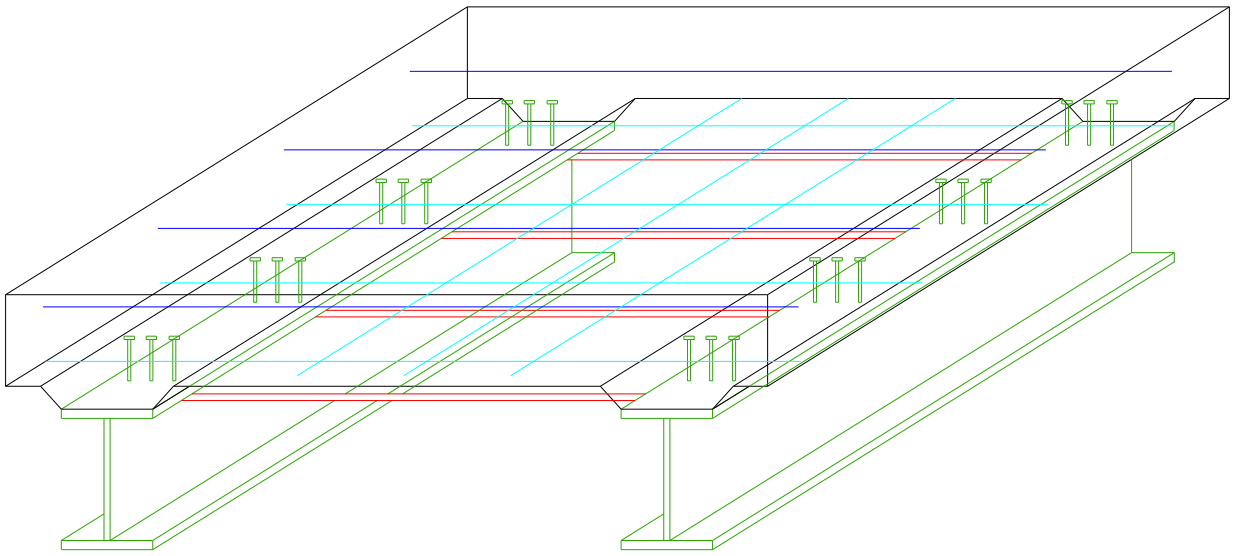

Figure 2.7 Typical bridge deck slab using second generation steel-free design method. Red signifies bottom transverse steel straps, dark blue signifies top GFRP crack control reinforcement, and light blue signifies bottom GFRP crack control reinforcement

2.2 Rational Model and Finite Element Analysis of Concrete Bridge Deck Slabs

[Kinnunen and Nylander (1960)] described a rational model for predicting the punching shear strength of reinforced concrete bridge deck slabs. This model considered the stresses in the internal reinforcement as one of the key parameters. Following the work of [Mufti et al., (1993)], it became apparent there was a need for a new and improved model that could predict the punching shear strength of steel-free concrete bridge deck slabs, where the absence of internal steel reinforcement made past models obsolete. [Wegner and Mufti (1994)] demonstrated that is was possible to predict the punching shear strength of steel-free concrete bridge deck slabs using nonlinear finite element analysis; unfortunately several modeling parameters were rather sensitive and required tedious fine tuning in order to produce good correlations. Using the research findings of [Kinnunen and Nylander (1960)], [Hewitt and Batchelor (1975)], [Wegner and Mufti (1994)] and others, [Newhook (1997)] proposed an improved model that considered the external lateral restraint conditions of a steel-free concrete bridge deck slab. The model was mainly an adaptation of previous models and considered many of the same parameters and components. A full description of the rational model can be found in [Newhook (1997)].

2.2.1 Characteristic Concrete Bridge Deck Slab Behavior

Confined concrete bridge deck slabs possess very distinct cracking patterns that are the same for slabs reinforced internally and externally. [Kinnunen and Nylander (1960)] and later, [Newhook (1997)], describe with detail the progression of cracking in concrete bridge deck slabs. Shortly after loading commences, longitudinal cracks appear on the soffit of the deck roughly between the girders. As loading increases, radial cracks begin to develop directly beneath the load on the soffit of the deck and radiate outwards in all directions. The radial cracks soon become full depth cracks and continue their outward migration. At a substantially higher load, circumferential cracks extending roughly the span of the girders form on top of the deck and encircle the load patch. Furthermore, the final crack to form prior to punch failure is an inclined shear crack. This crack begins on the soffit of the deck, located roughly the equivalent

distance from the load patch to the haunch or the inside portion of the top flange, depending on the design of the deck; the shear crack than propagates diagonally upwards and inwards towards the point of load application. Once the inclined shear cracks develop completely, they mark the boundary where the punch cone separates from the rest of the deck during punching failure. Prior to failure, the radial, circumferential and inclined shear cracks mentioned above make up the outline for a series of wedges that form around the load patch. The wedges then rotate around a center of rotation until they reach a point of equilibrium. The center of rotation is roughly located at the point where the wedges intersect with the loaded area; this area is believed to be in a state of three-dimensional compressive stress.

2.2.2 PUNCH Program

The rational model proposed by [Mufti and Newhook (1998)] lead to the development of a computer program known as PUNCH. The purpose of PUNCH was to provide researchers and bridge designers with a tool capable of predicting the behavior of externally reinforced steel-free concrete bridge decks with reasonable accuracy.

As with any computer software, PUNCH requires a number of modeling parameters be inputted prior to running the program. The key geometric properties include depth of concrete, d, area of tire print, A, diameter of equivalent circle for loaded area, B, and longitudinal distance from wheel load to nearest strap, D. The key material properties include compressive strength of concrete, f'c, rectangular stress block parameter, β_1, concrete confinement constant, k, and yield strain of steel strap, ε_y. Finally, arguably the most important input parameter of all, the transverse or lateral restraint stiffness, K.

The transverse restraint stiffness, K, is the fundamental parameter that governs the ultimate capacity at which an externally reinforced concrete bridge deck slab will fail in punching. The degree of lateral restraint can be attributed primarily to confinement provided by the external transverse steel straps, and to a lesser degree the stiffness of top flange of the girders. There are two recommended ways to calculate the value of K. For experimental purposes and accuracy in mind, [Newhook (1997)] presents a formulation that compares the actual lateral restraint provided by the external steel straps and the girders to a beam on elastic springs model; the springs represent the straps and the beams represent the girders. For a conservative estimation of restraint stiffness, [Newhook (1997)] also provides a more design oriented method to calculate K; this time K is in the form of an equation. The second method only considers the properties of the external steel straps. The equation for K is given as,

$$K = \frac{E \cdot A_s}{0.5 \cdot S_l \cdot S_s}$$

where E, A_s, S_l, and S_s represent the modulus of elasticity of the strap, the area of the strap, the length of the strap and the longitudinal spacing of the straps, respectively. This equation underestimates the degree of restraint stiffness and therefore results in lower outputs when dialed into the PUNCH program; for example, the PUNCH program will estimate a relatively lower ultimate punching shear capacity than the true ultimate punching shear capacity. A list of past theoretical and experimental comparisons has been compiled and is presented in Table 2.1, [Mufti and Newhook, (1998)] and [Memon (2005)].

Table 2.1 Comparison of theoretical and experimental results; Reproduced from [Mufti and Newhook (1998)] and [Memon (2005)]

Test	f'c N/mm^2	Girder Spacing mm	Straps mm^2 @ mm c/c	Deck Depth mm	K N/mm^2	P Theor kN	P Exp kN	P Theor / P Exp
Half-Scale (Mufti et al. 1993; Newhook et al. 1995)								
1	45.0	1067	640 @ 457	100	630	415	418	0.99
2	46.1	1067	640 @ 547	100	630	409	418	0.98
3	41.8	1067	640 @ 547	95	630	362	370	0.98
4	41.8	1067	640 @ 547	95	630	362	388	0.93
5	43.0	1067	640 @ 610	95	472	315	313	1.01
Skewed (Bakht and Agarwal 1995)								
6	55.0	800	608 @ 400	80	921	388	323	1.20
7	55.0	800	608 @ 400	80	921	388	352	1.10
Full Scale (Thorburn and Mufti 1995; Newhook abd Mufti 1996; Mufti et al. 1999)								
8	27.0	2000	2500 @ 1000	175	705	1147	1127	1.02
9	27.0	2000	1250 @ 1000	175	460	930	923	1.01
10	27.0	2000	950 @ 1000	175	370	830	911	0.91
11	27.0	2000	650 @ 1000	175	300	730	844	0.86
12	27.0	2000	650 @ 1000	175	300	730	576	1.27
13	27.0	2000	650 @ 1000	175	300	730	715	1.03
14	39.0	2700	1250 @ 1200	300	297	1269	1275	1.00
15	39.0	2700	650 @ 1000	300	86	937	951	0.99
Repaired (Thorburn and Mufti 2001)								
16	27.0	2000	2500 @ 1000	175	700	1143	785	1.46
17	27.0	2000	650 @ 1000	175	300	730	687	1.06
Reinforced Concrete (Mufti et al. 1999; Bakht and Lam 2000)								
18	30.0	2000	Steel Rebar	175	211	819	808	1.01
19	30.0	2000	Steel Rebar	175	218	834	793	1.05
20	35.0	2000	Steel Rebar	175	218	888	888	1.00
21	35.0	2000	GFRP Rebar	175	211	873	756	1.15
22	-	2133	Steel Rebar	190	200	627	631	0.99
23	-	2000	Steel Rebar	150	428	629	622	1.01

2.3 Fatigue Effects on Concrete Bridge Deck Slabs and Related Research

Several key theses and published papers have been written over the years that discuss the effects of fatigue on concrete bridge deck slabs. [Perdikaris and Beim (1988)] studied the effects of fatigue on internally reinforced deck slabs under pulsating loads. [Selvadurai and Bakht (1996)] noted the effects of fatigue on steel-free deck slabs subjected to simulated rolling wheel loads. [Matsui et al. (2001)] also researched the effects of fatigue on steel-free bridge deck slabs, however, the decks were tested under sequential wheel loading. [Limaye (2004)] analyzed the crack response of steel-free concrete bridge deck slabs under cyclic loading and additionally explored the idea of GFRP and steel crack control grids. [Memon (2005)] compared the fatigue life of steel reinforced and steel-free concrete bridge deck slabs under cyclic loading, along with evaluating different crack control methods.

2.3.1 Selvadurai and Bakht (1996)

As a result of the research done by [Perdikaris and Beim (1988)], there was a strong desire to accurately replicate the running movement of a commonly used dual truck tire. In order to do so, an innovative simulation of a rolling wheel was developed. The simulation composed of four actuators attached to four stationary pads, each representing the contact area of a dual tire as it would appear in the field. Loading of the pads occurred sequentially in a strategic pattern that closely mimicked the actual passage of a wheel on a concrete bridge deck slab. The ability to reach speeds of up to 40 km/hr made the rolling wheel simulation an attractive apparatus for researchers; unfortunately a maximum of 98 kN limited the range of damage that could be achieved on a full scale bridge deck slab.

In the mid 1990's, engineers were still very skeptical of the steel-free concept. Fatigue studies on steel reinforced concrete bridge deck slabs had already been carried out in numerous experiments; whereas similar studies for steel-free concrete bridge deck slabs were essentially nonexistent. In the absence of experimental fatigue data, a full sized steel-free slab-on-girder concrete bridge deck was constructed at

Carleton University for this reason. The concrete deck alone measured 6,000 mm in the longitudinal direction, 3,000 mm in the transverse direction, and maintained a uniform thickness of 175 mm. The two supporting girders rested 2,000 mm apart center to center, while the 127 x 25 mm transverse steel straps were spaced at 750 mm intervals. Composite action between the girders and the concrete deck was provided by shear studs. The concrete slab was mixed with 0.88% by volume of 35 mm fibrillated polypropylene fibres to control shrinkage and thermal cracking. Finally, diaphragms were installed at each end of the deck to provide support to the free edges of the deck.

The concrete deck mentioned in the previous paragraph was tested using the simulated rolling wheel technique. At first, two million passes of each 53, 71 and 89 kN were applied to the deck, followed by four million passes of 98 kN. The maximum observed wheel load in Canada was around 100 kN and considering at the time the OHBDC (1992) specified that a steel-free bridge deck slab must have adequate fatigue strength to sustain two million passes of 75 kN, the experiments confirmed that steel-free bridge deck slabs perform confidently well under fatigue loading. Several longitudinal and transverse cracks appeared during the early stages of testing; however, they did not appear to increase in size or affect the structural integrity of the deck.

Because the deck under review was still in rather good condition, an extra three fatigue tests were conducted. First, the original transverse steel straps were removed and replaced with straps only half the size of the originals and the deck was tested an additional four million passes of 98 kN. The only effect this had was a minor increase in deflection. The second test involved submerging the deck under a layer of water and subjecting it to four million passes of 98 kN. Submerging the deck under water appeared to have no effect on the deck. Thirdly, the transverse straps were removed altogether, leaving only the end diaphragms for transverse confinement; once again four million passes of 98 kN was applied to the deck and once again the deck survived, only this time the deck sustained a 40% increase in deflection. Overall,

the deck withstood a total of sixteen million passes of 98 kN and remarkably did not show any sign of distress. Once the researchers were satisfied with the fatigue results, the deck was failed based on serviceability criteria at a load of 390 kN.

A second model mirroring the first deck described above was constructed; the only difference being the second model did not contain any crack control polypropylene fibres. The second model was also subjected to two million passes of each 53, 71 and 89 kN, followed by four million passes of 98 kN. The results were similar to the first model and it was concluded that steel-free slab-on-girder concrete bridge decks, with or without crack control fibres, comfortably met the requirements specified by the OHBDC (1992).

2.3.2 Matsui et al. (2001)

In the early 2000's, a group of researchers working out of Osaka University in Japan set out to quantify the fatigue life of steel-free concrete bridge deck slabs. An actual running wheel system was chosen to replicate the movement of a truck wheel on a bridge deck.

In total, three 150 mm thick steel-free concrete deck slab models were casted. All three models sat on two parallel girders spaced 1.8 m center to center. Each model measured 3.1 m longitudinally and 2.1 m transversely. 50 x 9 mm steel straps were bolted to the girders; the bolts also acted as shear studs. Shrinkage and thermal cracks were controlled by adding small fibres into the concrete mix at a percent by volume of 0.55%. Finally, the models were designated PFRC1, PFRC2, and PFRC3. Specimens PFRC2 and PFRC3 were near identical, while PFRC1 differed in the fact that its edge beams were kept detached from the deck.

The loading assembly comprised of an actual wheel powered by a hydraulic jack capable of swaying back and forth along an overhead frame. The hydraulic jack was also attached to a reciprocating leverage arm that was attached to another arm that rotated around a motor located on the outskirts of the bridge deck.

The reciprocating arm propelled the hydraulic jack back and forth, providing a 2 m stroke in the longitudinal direction, from one end of the deck to the other end. The wheel travelled on a steel track running parallel to the girders, situated roughly midway between the girders, on the top of the deck.

The following table lists the applied loads and corresponding number of cycles, as well as the failure mode of all three models.

Table 2.2 Loading compilation; Reproduced from [Matsui et al. (2001)]

Designation	Wheel load (KN)	Loading Passes
PFRC1	118 147 176	20,000 20,000 218,000 Bending failure
PFRC2	118 147 176	20,000 20,000 474,000 Punching shear failure
PFRC3	118 147	20,000 980,000 not failure

As indicated in Table 2.2, PFRC1 failed in bending failure, PFRC2 failed in punching shear and PFRC3 was not loaded to failure. All three models developed Y-shaped cracks on the soffit of the deck near the edge beams. For PFRC1, failure occurred when a triangular portion, outlined by the Y-shaped cracks, separated from the rest of the deck. PFRC2 also failed in conjunction with the Y-shaped cracks; however, punching shear failure was the culprit.

In conclusion, many of the cracks appearing on the deck, particularly the Y-shaped cracks, exceeded conventional reinforced concrete crack widths at serviceability limit state; this was contributed to the absence of internal reinforcement in the steel-free bridge deck slabs. Furthermore, the difference in loading of PFRC models 2 and 3 (474 000 cycles @ 176 kN for PFRC 2 and 980 000 cycles @ 147 kN for

PFRC 3) clearly demonstrates that increasing or decreasing load values, even by a small margin, drastically affects the resulting number of cycles to failure.

2.3.3 Limaye (2004)

It was now becoming well known to researchers that longitudinal and transverse cracks appearing on the top and bottom of steel-free concrete bridge deck slabs under cyclic loading did not necessarily affect the structural integrity of the structure, however, the cracks were exceeding serviceability limits and were being considered an uncanny sight to the public. Consequently, a research program was developed to first, study the initiation and propagation of cracks and second, investigate a technique capable of reducing the width of cracks to below an acceptable limit.

Execution of the program was carried out at Dalhousie University in Nova Scotia. A full scale steel-free concrete bridge deck model, measuring 12.2 m longitudinally and 3 m transversely, was constructed and divided conceptually into four sections, designated Panels A, B, C, and D, each measuring 3.05 m longitudinally and 3 m transversely. The entire fibre reinforced slab maintained a uniform thickness of 175 mm. The supporting parallel girders were spaced 2 m center to center, leaving the deck slab to cantilever 500 mm beyond the centerline of each girder. Each panel was externally restrained with three 50 x 16 mm transverse steel straps spaced 1.02 m center to center.

All four panels served a specific purpose and were tested under cyclic loading in two phases. Although the panels were identical geometrically, they differed internally. Panel A was completely void of internal reinforcement and served mainly to observe the crack initiation and propagation under cyclic loading. Panel B was also completely void of internal reinforcement; however, a pre-induced longitudinal crack was introduced to the soffit of the deck by installing a 75 mm high crack trainer spanning the length of the panel prior to casting the concrete. The purpose of the pre-induced crack was to study the effect of a full depth crack under cyclic loading. Panel C and D were both designed with the ambition to determine a

method that minimized cracking and reduced the overall width of cracks under cyclic loading. Panel C was casted with an internal orthogonal bottom layer of 16 mm diameter GFRP bars spaced at 500 mm in the transverse direction and 850 mm in the longitudinal direction. Panel D was casted with an internal isotropic bottom layer of 10M steel reinforcing bars spaced at 300 mm in both directions. The internal reinforcing GFRP and steel bars were considered secondary reinforcement, strictly serving the purpose of crack control; while the external transverse steel straps acted as the primary reinforcement, thereby defining the ultimate capacity of the deck. Table 2.3 outlines the fatigue program performed on each panel; the table shows the number of cycles per load value, as well as when failure occurred in each panel.

Table 2.3 Summary of failure data for panels; Reproduced from [Limaye (2004)]

	Number of load cycles							
Peak load (kN) (t)	393 (40)	638 (65)	785 (80)	883 (90)	981 (100)	1030 (105)	1079 (110)	1218 (124)
Panel A	50,000*	10,000	2,000	1,243 (F)	---------			
Panel D	1,700*	---------	---------	5,000	41	50	108 (F)	
Panel C	1,700*	---------	---------					
Panel B	1,700*			---------	1		1	1 (F)

* 1,700 load cycles applied in Phase – I
(F) Denotes failure at that peak load

Several important conclusions were drawn from the test program. First, one layer of bottom crack control reinforcement was able to significantly reduce the widths of longitudinal cracks by dispersing what would normally be one large longitudinal crack into numerous small insignificant cracks, only noticeable upon close visual inspection. The internal crack control reinforcement also enhances the confinement of the system and mildly contributes to the punching strength of the deck slab. Both steel and GFRP crack control reinforcement worked effectively; however, in the grand scheme of things, and considering the larger percent volume of steel compared to GFRP, GFRP performed moderately better when it came to crack

widths and extent of cracking. According to the punch tests performed on Panel B, a full depth crack does not affect the strength of the deck.

2.3.4 Memon (2005)

Realizing the significance of crack control reinforcement in steel-free bridge deck slabs, a new program entertaining the use of GFRP and CFRP reinforcements was devised. The program was aimed at comparing the behavior and fatigue life of GFRP and CFRP crack control reinforced steel-free concrete bridge deck slabs versus a conventionally steel reinforced concrete bridge deck slab.

The bridge deck used for this experiment was conceptually divided into three sections, designated segments A, B, and C, each measuring 3 m by 3 m. The overall dimensions of the full scale bridge deck slab measured 9 m longitudinally and 3 m transversely. The entire concrete slab maintained a uniform thickness of 175 mm. Although the deck was casted as one single structure, all three segments were designed differently. Segment A was a conventionally designed steel reinforced concrete deck slab and was considered the base for comparison for the two steel-free concrete bridge deck slabs. Segment A consisted of two isotropic layers of 15 M steel bars spaced at 300 mm in both directions for primary reinforcement. Segment B was a steel-free designed concrete bridge deck slab consisting of two orthotropic layers of #3 (9.53 mm) crack control CFRP bars spaced at 200 mm in the transverse direction and 300 mm in the longitudinal direction. Segment C was also a steel-free designed concrete deck slab; however, Segment C consisted of two orthotropic layers of #4 (12.7 mm) crack control GFRP bars spaced at 150 mm in the transverse direction and 200 mm in the longitudinal direction. Both Segment B and C were primarily reinforced through arching action with 25.4 mm by 38.1 mm external transverse steel straps spaced at 1,000 mm center to center. Cyclic loading was applied through a hydraulic actuator with a 610 mm x 305 mm loading pad.

In order to compare the sections experimentally, all three segments underwent similar loading programs, as shown in Table 2.4. Loading took place in three consecutive steps; the applied loading in steps 1, 2, and 3 were 245, 490, and 588 kN respectively. Segments A and B did not partake in the testing of step 2 because the lack of evidence for failure in segment C at 490 kN indicated there was no need to. Several conclusions were drawn from the testing. First, it was safe to say that after 1,000,000 cycles at 245 kN, all three segments satisfied serviceability limits for deflection, crack widths, steel reinforcement strains and steel strap strains. Second, although all three segments were identical with respect to geometry and concrete properties, the differences in confinement significantly affected the overall fatigue resistance of each segment. Finally, all three segments failed in punching shear.

Table 2.4 Fatigue program; Reproduced from [Memon (2005)]

	Number of Load Cycles		
Loading Set	1	2	3
Peak Load (kN) (t)	245 (25)	490 (50)	588 (60)
Segment A	1,000,000	---------	23,162 (F)
Segment B	1,000,000	---------	198,863 (F)
Segment C	1,000,000	1,000,000	420,683 (F)

(F) Denotes failure at that peak load

2.4 Fatigue Life Estimation Models for Steel-Free and Steel Reinforced Concrete Bridge Deck Slabs

Many researchers have tried to quantify the fatigue life of steel reinforced and steel-free concrete bridge deck slabs into a simple expression. Several notable attempts are present in the following papers and theses:

- Batchelor and Hewitt (1974) – Tested reinforced concrete slabs.

- Young and Chang (1998) – Tested reinforced concrete slabs.
- Matsui et al. (2001) – Tested reinforced concrete.
- Mufti et al. (2002) – Tested concrete cylinders.
- Memon (2005) – Tested steel-free concrete slabs.
- El-Ragaby et al. (2007) – Tested GFRP reinforced concrete slabs.

All six references listed above propose different fatigue life evaluation models; however, each expression considers the same relationship between two key variables. Each expression relates the ratio of applied load, P, over the estimated static failure load, P_s,(P/P_s), to the number of load cycles (N) to failure. It should be noted that the tests in the following experiments were performed on several different apparatus' including reinforced concrete slabs, concrete cylinders or steel-free concrete slabs.

2.4.1 Batchelor and Hewitt (1974) Estimation Model

[Batchelor and Hewitt (1974)] investigated the fatigue life of five small scale reinforced concrete slabs. The slabs were all approximately 1/8th the size of s full scale concrete bridge deck slab and were comprised of two internal reinforcement configurations; the slabs were designed with either isotropic or orthotropic internal reinforcement. The tests and analysis' conducted, resulted in the following expression.

$$\frac{P_f}{P'_s} = 1.0 - 0.102 * N + 0.006 * N^2 \qquad \textbf{Equation 2.1}$$

Where,

P_f = applied load

P'_s = estimated static failure load

N= log number of load (P) cycles to failure

2.4.2 Young and Chang (1998) Estimation Model

Similar to [Batchelor and Hewitt (1974)], [Young and Chang (1998)] conducted fatigue tests on reinforced concrete slabs. The slabs tests in this experiment were approximately 1/3rd the size of a full scale bridge deck slab. [Young and Chang (1998)] proposed the following expression.

$$log\left(\frac{P}{P_s}\right) = -0.066 * \log(N) + log(1.4461) \qquad \textbf{Equation 2.2}$$

Where,

P = applied load

P_s = estimated static failure load

N = log number of load (*P*) cycles to failure

2.4.3 Matsui et al. (2001) Estimation Model

Recognizing the lack of knowledge and research regarding the fatigue life of steel-free concrete bridge deck slabs, [Matsui et al. (2001)] devised an experimental program that involved the testing of three full scale steel-free specimens under running wheel load. The results generated the following expression.

$$log\left(\frac{P}{P_{sx}}\right) = -0.07835 * log(N) + \log(1.52) \qquad \textbf{Equation 2.3}$$

Where,

P = applied load

P_{sx} = static punching shear capacity

N = number of wheel load (*P*) passes to failure

2.4.4 Mufti et al. (2002) Estimation Model

An outside the box approach to determining the fatigue life of steel-free concrete bridge deck slabs was carried out by [Mufti et al. (2002)]. The experimental program included the fatigue testing of an arbitrary sample size of standard 35 MPa concrete cylindrical specimens. The results indicated that the cylindrical specimens failed at a specific number of cycles, directly related to the applied load used. The applied loads

used were a percentage of the estimated static load capacity. In the end, a revised edition of Matsui's expression (Eq. 2-3) was put forth.

$$\frac{P}{P_s} = 1.0 - \frac{ln(N)}{30}$$ **Equation 2.4**

Where,

P = applied load

P_s = static punching shear capacity

N = number of load (*P*) cycles to failure

2.4.5 Memon (2005) Estimation Model

Realizing the lack of research into the formation of an expression for the fatigue life of steel-free bridge deck slabs, [Memon (2005)] proposed the following expression to predict the number of load cycles to failure for steel-free and steel reinforced concrete bridge deck slabs. The expression was formed based on the testing conducted on a of a full scale concrete bridge deck specimen divided into a steel-free designed section and a steel reinforced designed section.

$$n = 10^{c*\sqrt{\frac{1}{\frac{P}{P_S}} - 1}}$$ **Equation 2.5**

Where,

P = applied load

P_s = static punching shear capacity

c = 5.737 (for GFRP)

c = 4.4138 (for Steel Reinforced)

n = number of load (*P*) cycles to failure

In addition, a secondary expression was proposed that expanded on the expression originally formed based on the work done by [Mufti et. al (2002)].

$$\frac{P}{P_s} = 1.0 - \frac{ln(N)}{M}$$ **Equation 2.6**

Where,

P = applied load

P_s = static punching shear capacity

M = 26.5 (for GFRP)

M = 20.5 (for Steel Reinforced)

N = number of load (*P*) cycles to failure

2.4.6 El-Ragaby et al. (2007) Estimation Model

[El-Ragaby et al. (2007)] proposed the following expression to predict the number of load cycles to failure for GFRP reinforced and steel reinforced concrete bridge deck slabs.

$$\frac{P}{P_u} = 0.0034 * (logN)^2 - 0.11873(logN) + 1.0752$$ **Equation 2.7**

Where,

P = applied load

P_u = static punching shear capacity

N = number of load (*P*) cycles to failure

2.5 Steel-Free Bridge Decks in Canada

Over the years, numerous steel-free concrete bridge decks have been constructed throughout Canada. The steel-free design has proven so far to be an efficient and cost effective alternative to conventionally designed concrete bridge deck slabs. Since the implementation of the steel-free bridge decks into the field in the mid and late 1990's, feedback from observations and regular assessments has shown very positive results.

2.5.1 Salmon River Bridge

The very first steel-free concrete bridge deck implemented into the field was the Salmon River Bridge situated in Nova Scotia, Canada. The bridge was spanned into two simply supported sections, both spanning 32.2 m. The two sections were designed differently in that the first section was designed with conventional steel reinforcement, while the second section incorporated the steel-free concept. With the absence of internal steel reinforcement, the steel-free deck slab was restrained through arching action provided by transverse steel straps welded to the top flange of adjacent steel plate girders. The transverse steel straps were of size 100 x 12 mm and were spaced at 1.2 m center to center. The girders were spaced at 2.7 m center to center. In order to accommodate external geometrical constraints, the deck was skewed at an angle of 22°. The steel-free deck slab consisted of fibre reinforced concrete, casted to a thickness of 200 mm, and with a polypropylene fibre content of 0.55% the volume of concrete. The bridge was open to traffic in December, 1995.

After many years being subjected to heavy traffic and countless freeze thaw cycles, several field assessments were carried out on the Salmon River Bridge, [Mufti et al., (1999)]. The results have been mostly positive, barring several serviceability issues. Wide longitudinal full depth cracks on the soffit of the deck, roughly midway between the girders, were reported on the steel-free slabs. Although the longitudinal cracks may be an unsightly aesthetic issue for the public, the structural integrity of the deck appeared to be very much intact.

2.5.2 Chatham Bridge

The Chatham Bridge, located on the Kent County Road No. 10 in Chatham, Ontario, was nearing the end of its service life. The bridge was a key element for the very busy expressway No. 401. In the fall of 1996, a rehabilitation project began that saw the replacement of the four original concrete deck spans with two new conventionally steel reinforced sections and two new steel-free sections. The supports for the decks

were spaced at 13, 20, 20 and 13 m longitudinally from one end to the other. The new steel-free concrete slabs were constructed and designed for the exterior 13 m spans, while the conventionally steel reinforced segments were placed in the longer middle spans. The outer steel-free deck slabs were 175 mm thick and rested on parallel girders spaced at 2.1 m center to center. The steel-free deck slabs were externally restrained with 20 x 50 mm galvanized steel straps welded to the top flange of the adjacent steel girders. In order to facilitate easy removal of the formwork, the slabs sat on elevated haunches attached to the girders through the use of shear studs; this allowed for ample room between the straps and the soffit of the slabs. The cantilever overhangs supporting the barrier walls on each side of the bridge deck were also designed to avoid the use of any internal steel reinforcement. Because a negative moment develops over the girders for the cantilever overhangs, tensile reinforcement is needed in these zones. Instead of reinforcing the negative moment zones with steel reinforcement, a CFRP grid was placed near the top surface. In order to subdue shrinkage and thermal cracking, polypropylene fibres were added into the concrete mix at a total volume content of 0.55%.

2.5.3 Crowchild Trail Bridge

The Crowchild Trail Bridge was constructed in Calgary, Alberta. Unlike the Salmon River Bridge and the Chatham Bridge, the Crowchild Trail Bridge was entirely designed using the steel-free concrete bridge deck concept. Three spans at distances of 30, 33, and 30 m made up the full longitudinal length of the bridge. The thickness of the concrete deck was a uniform 185 mm and the supporting parallel steel girders were spaced 2 m center to center. The deck slab was restrained by 50 x 25 mm transverse steel straps which were studded at the ends in order to bond with the concrete slab. The deck was designed as a continuous slab over the supports; this created negative moment regions over the supports. To avoid the use of tensile steel reinforcement in the negative moment zones, tensile GFRP reinforcement was used as an alternative. GFRP grids were also used for the negative moments created by the cantilever

overhangs. The concrete used for the slabs was mixed with polypropylene fibres at a percent by volume of 0.44% in order to reduce shrinkage and thermal cracking.

2.5.4 Waterloo Creek Bridge

Waterloo Creek Bridge was the fourth application of the steel-free bridge deck slab and was opened to traffic in early 1998. The bridge was constructed in British Columbia, Canada. Unlike the three previously discussed steel-free concrete bridges, the Waterloo Creek Bridge was supported on precast concrete girders. The concrete girders were spaced 2.8 m center to center and in order to make the concrete slab and the concrete girders composite, shear studs were placed into the top flange of the concrete girders. The bridge and girders consisted were stretched over one simply supported span of 25 m. The 190 mm steel-free concrete slab was casted with haunches to separate the 50 x 25 mm studded transverse steel straps from the soffit of the deck. Instead of using small fibres to control shrinkage and thermal cracking, low reinforcement ratios of tensile steel reinforcement was placed in segments near the girders, along with four longitudinal GFRP bars positioned above each girder.

2.5.5 Lindquist Creek Bridge

For the Lindquist Creek Bridge, located in British Columbia, researchers and engineers wanted to develop a completely new method to design and construct steel-free concrete bridge deck slabs. Because patents on cast-in-place steel-free deck slabs were already in existence, as well as the patent for precast reinforced concrete panels, the idea of precast steel-free panels was brought forth. The Lindquist Creek Bridge was the first application of the precast steel-free panel. The Lindquist Creek Bridge, being a forestry bridge, was designed as a single lane, single span structure. The deck itself was 150 mm thick, and embedded in it was 25 x 50 mm transverse steel straps spaced at 1.0 m center to center. In order for the precast deck to become composite with the adjacent girders, circular holes in the bottom of the precast panels were left void so they could be positioned on top of the shear studs and finally, grout was pumped into the

voids to fix a bond between the deck and girders. A large spacing of 3.5 m center to center was used for adjacent girders. The deck was opened to traffic in December, 1997. One of the main advantages of precast steel-free panels is that they can be opened to traffic within 24 hours succeeding the erection of the structure.

Chapter 3

Design and Detail of Experimental Program

3.1 General

Chapter 3 outlines the design and detail of the concrete bridge deck constructed for the purpose and objective of this experimental program.

3.2 Steel Girders

Supporting the bridge deck, were two W920 x 387 parallel steel girders spaced at 2,500 mm center to center. Each girder measured 9,000 mm in length and was simply supported on two concrete blocks that were stressed to the structural floor; 19 mm web stiffeners were situated along the length of the girders. In order to facilitate composite action between the bridge deck and the girders, 22 mm diameter by 200 mm long nelson shear studs were welded to the top flange of the girders; the nelson studs sat 110 mm apart in the transverse direction and 400 mm apart in the longitudinal direction. Figure 3.1 provides a plan view and side view of the girder configuration, along with shear stud and web stiffener detailing. The sectional properties and limit state design values of the steel girders are shown in Table 3.1. The shear and moment resistances, along with the permissible deflection found in Table 3.1 were computed according to CAN/CSA-S16-01.

Table 3.1 Steel girder properties and limit states design values

Steel Girder	W920 x 387	Units
Cross Section Area	49400	mm^2
Depth (d)	920	mm
Flange Width (b)	420	mm
Flange Thickness (t_f)	36.6	mm
Web Thickness (w)	21.3	mm
Moment Resistance	5500	kN-m
Shear Resistance	4020	kN
Permissible Deflection	25	mm

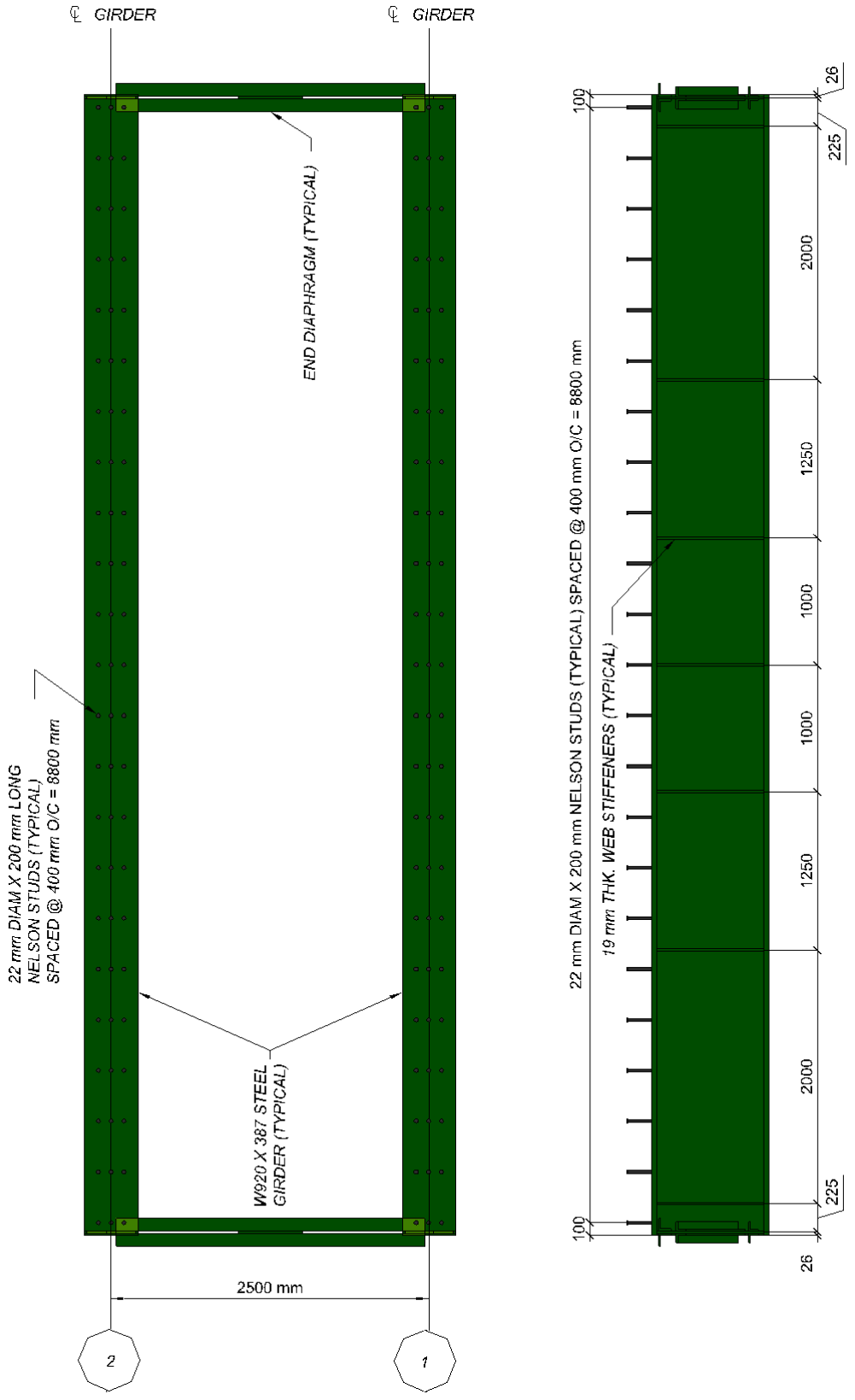

Figure 3.1 Plan and side view of girder configuration schematic used in this experiment

3.3 Concrete Details

The full-scale concrete bridge deck slab built for this experiment measured 9,190 mm in length and 6,500 mm in width, as shown in Figure 3.2. The slab itself maintained a constant thickness of 200 mm, except for an additional 75 mm haunch used to prop the deck slab above the girders. In total, approximately 17.5 m^3 of concrete was required for the construction of the concrete portion of the bridge; including both deck slab and barrier walls. Figure 3.3 illustrates a cross-section view of the concrete deck slab and barrier walls (reinforcement excluded). The specified concrete mix design and concrete properties are outlined in Table 3.2. Concrete cylinder testing resulted in the data shown in Table 3.3.

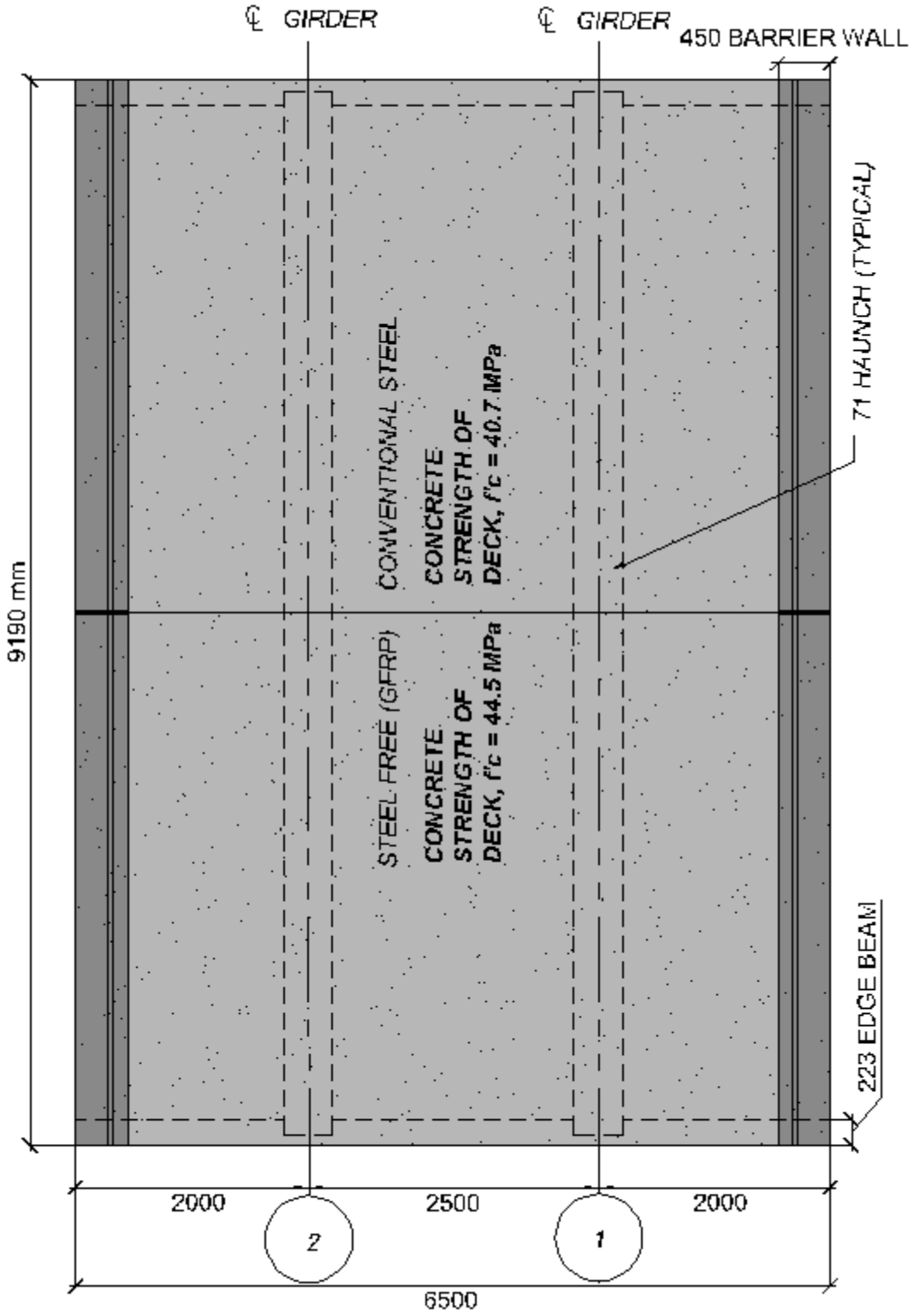

Figure 3.2 Plan view of concrete bridge deck slab schematic used in this experiment

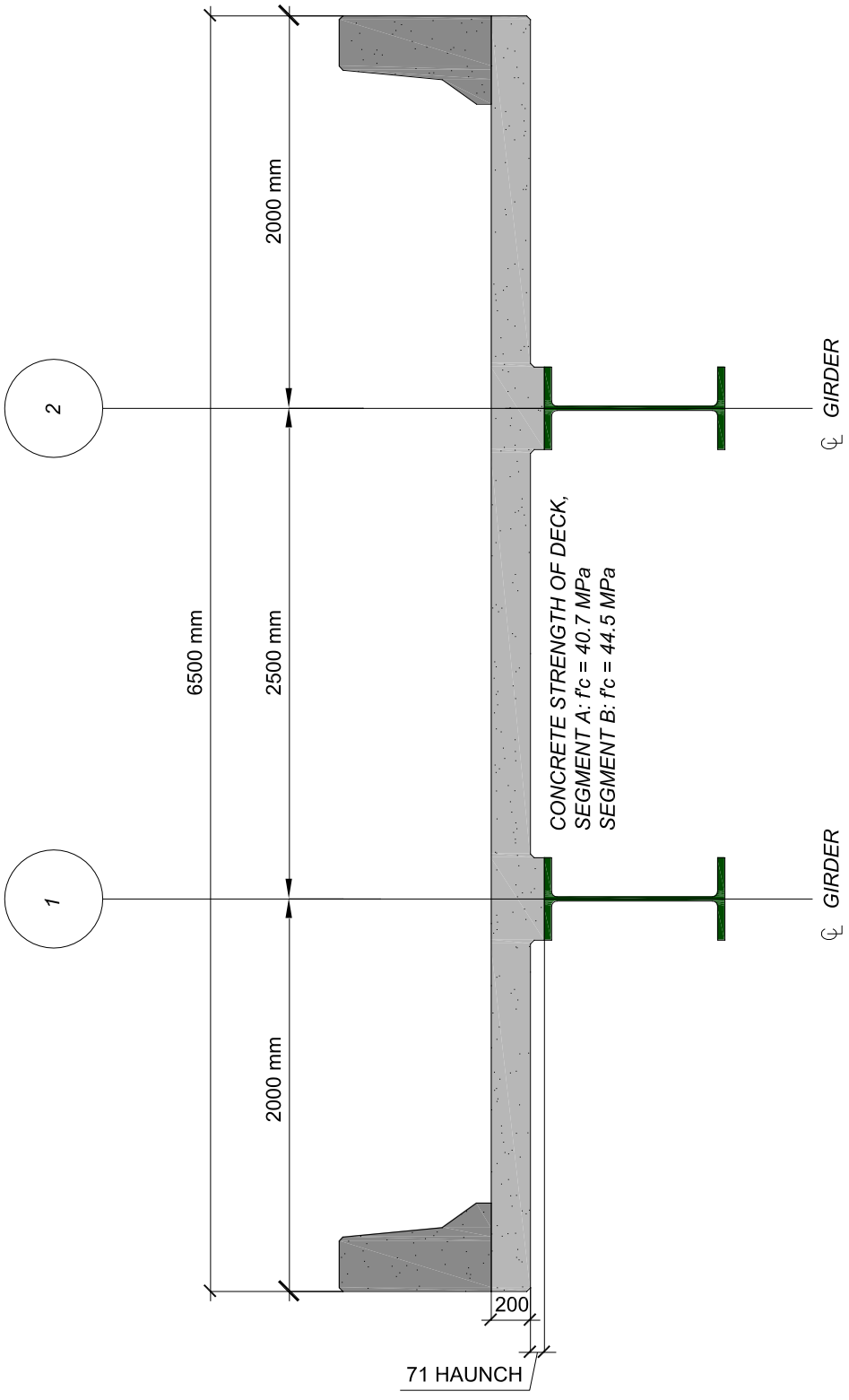

Figure 3.3 Cross section view of concrete bridge deck slab schematic used in this experiment

Table 3.2 Concrete mix design and concrete properties

Component	Value	Unit
Specified Design Strength	35	Mpa
Cement Content (Type 10):	380	kg/m^3
Water Content:	152	kg/m^3
Water/Cement Ratio:	0.4	
Air Content:	(4 - 6)	%
Course Aggregate:	1055	kg/m^3
Fine Aggregate:	765	kg/m^3
Max. Aggregate Size:	20	mm
Specified Slump	80	mm

Table 3.3 Concrete Cylinder Test Results

Component	Segment A	Segment B
28 Day Concrete Strength (Mpa) Date of Casting: Jan 30, 2008	34.8	38.0
Segment A: Concrete Strength (Mpa) @ Test Start Date Test Start Date: June 18, 2010	40.72	-
Segment B: Concrete Strength (Mpa) @ Test Start Date Test Start Date: May 17, 2011	-	44.5

3.4 Concrete Bridge Deck Slab Design

The 9,190 mm long by 6,500 mm wide full scale concrete bridge deck slab was conceptually divided into two segments. Segment A represented a conventionally designed steel reinforced concrete bridge deck slab; while Segment B reflected a steel-free concrete bridge deck slab. In an effort to compare both segments with respect to code provisions, each segment was designed based on minimum requirements according to CAN/CSA-S6-00. At the time of the design phase of the bridge deck in this experiment, CHBCD (2000) was still the most relevant code provision. In recognition that all concrete bridge decks are now designed based on minimum requirements provided in the most recent CAN/CSA-S6-06, the test results from this experiment are compared under CAN/CSA-S6-00/06 code provisions for the purpose of showing that the bridge deck is compatible with both code provisions in terms of design, serviceability, and fatigue limits. In a second effort to construct a direct comparison between the segments under fatigue, both segments contained similar reinforcement ratios in the bottom transverse direction. In addition, the slab thickness was maintained at a constant depth of 200 mm throughout the entire specimen, except for the edge beams positioned at each end of the bridge deck.

3.4.1 Segment A (Conventional Steel Reinforced)

Segment A was designed according to CAN/CSA-S6-00, Section 8.18.4 (Empirical Design Method). According to Section 8.18.1 (Design Methods), as long as the concrete bridge deck slab is designed in agreement with the specified conditions in Section 8.18.4, there is no need to analyze the deck slab except for areas containing negative transverse moments.

The empirical design method is relevant for a section of deck that maintains uniform thickness and is bounded by exterior supporting beams, provided that the following conditions are satisfied:

a) The deck slab is composite with the supporting beams; the beams are aligned parallel to each other; and the position of the beam supports line up parallel with each other;

b) The supporting beam spacing to slab thickness ratio is $\leq$ 18.0.

c) The spacing of the supporting beams does not exceed 4.0 m; and the slab projects a sufficient distance beyond the supporting beams in order to provide full development length for the bottom transverse reinforcement.

In addition to the conditions above, the empirical design method is applicable for a cast-in-place concrete deck slab provided that the following is satisfied:

a) Both top and bottom reinforcement is orthogonal in nature, and both top and bottom assemblies contain a minimum reinforcement ratio (ρ) of at least 0.003 in each direction in each assembly.

b) The reinforcing bars closest to the top and bottom of the slab are positioned perpendicular to the supporting parallel beams.

c) The reinforcing bar spacing in each direction does not exceed 300 mm for both top and bottom assemblies

Finally, Section 8.18.2 of the CAN/CSA-S6-00 states that in no case shall the slab thickness be less than 175 mm.

Satisfying the conditions outlined above, the following parameters were considered for Segment A:

- Supporting beam spacing to slab thickness ratio = 12.5 (< 18.0) O.K.
- Spacing of supporting beams = 2.5 m (< 4.0) O.K.
- Slab cantilever distance beyond supporting beams = 2.0 m
- Slab thickness = 200 mm (> 175) O.K.
- The spacing and reinforcement ratio (ρ) of steel reinforcement in each assembly is provided in Table 3.4.

$$\rho = \frac{A_s}{bd}$$ **Equation 3.1**

Where,

A_s = Total area of steel in specified layer [mm^2]

b = Width [mm]

d = Effective Depth [mm]

Table 3.4 - Reinforcement ratio and bar spacing for steel reinforcement

Layer	Area of Steel, A_s (mm^2)	Width, b (mm)	Effective Depth, d (mm)	Reinforcement Ratio, ρ (%)	Minimum Reinf. Ratio, ρ_{min} (%)	Bar Spacing (mm)	Minimum Bar Spacing (mm)
Bottom-Transverse	3000	4595	167	0.39	(≥ 0.3)	300	(≤ 300)
Bottom-Longitudinal	4600	6500	151	0.47	(≥ 0.3)	300	(≤ 300)
Top-Transverse	9000	4595	67	2.92	(≥ 0.3)	100	(≤ 300)
Top-Longitudinal	4600	6500	83	0.85	(≥ 0.3)	300	(≤ 300)

It is common practice to use 15M steel reinforcing bars for concrete bridge deck slabs. Therefore, 15M reinforcing bars were chosen for the top and bottom assemblies and a maximum spacing of 300 mm was used for each assembly, except for the top transverse steel bars where a spacing of 100 mm was applied.

3.4.2 Segment B (Steel-Free)

Segment B was designed according to CAN/CSA-S6-00, Section 16.7 (FRC Deck Slabs). It is stated that as long as the concrete bridge deck slab is designed in agreement with the specified conditions in Section 16.7 as follows, there is no need to analyze the deck slab except for areas containing negative transverse moments:

a) The deck slab is composite with parallel supporting beams.

b) The spacing of the supporting beams, S, does not exceed 3.0 m

c) In no case shall the slab thickness be less than 175 mm, and not less than S/15.

d) The supporting beams are braced with transverse diaphragms.

e) The height of the haunch is between 25 and 125 mm. The shear projection of the shear connecting devices into the deck slab, t_s, is a minimum of 75 mm.

f) The top flanges of all adjacent supporting beams are connected by external steel straps either connected directly to the top of the flanges (i.e. welded steel straps), or indirectly connected to the top of the flanges (i.e. partially studded straps).

g) The spacing of the straps, S_l, is not more than 1.25 m.

h) Each strap has a minimum cross-sectional area, A, in mm^2, given by

$$A = \frac{F_s S^2 S_l}{Et} 10^9 \qquad \textbf{Equation 3.2}$$

Where,

F_s = 6.0 for outer panels, 5.0 for inner panels

E = Modulus of Elasticity of the strap material [MPa]

t = Slab thickness [mm]

S_l = Strap spacing [mm]

S = Supporting beam spacing [mm]

Satisfying the conditions outlined above, the following parameters were considered for Segment B:

- Spacing of supporting beams = 2.5 m (< 3.0) O.K.
- Slab thickness = 200 mm (> 175 & > S/15) O.K.
- Haunch height = 71 mm (> 25 & < 125) O.K.
- Projection of shear connector = 154 mm (> 75) O.K.
- Strap spacing = 1.2 m (< 1.25) O.K.
- Area of one strap = 25 mm x 50 mm = 1,250 mm^2 (> $A_{s,min}$ = 1,125 mm^2) O.K.

According to Eq. 3.2, the minimum cross-sectional area for a steel strap, based on the parameters outlined above, is 1,125 mm^2. Subsequently, 25 by 50 mm steel straps were chosen for this project; resulting in a cross-sectional area of 1,250 mm^2 per strap.

In addition to the external steel straps used as the primary reinforcement, a secondary reinforcement was provided in Segment B to help control shrinkage, thermal and fatigue induced cracking. The secondary reinforcement was glass fibre reinforced polymer (GFRP) bars. The bottom reinforcing assembly was comprised of #10 GFRP Pultrall V-Rod spaced at 500 mm in the transverse and longitudinal directions. The top reinforcing assembly consisted of #10 GFRP Pultrall V-Rod spaced at 500 mm in the longitudinal direction and #25 Pultrall V-Rod spaced at 175 mm in the transverse direction. Furthermore, the reinforcement ratio (ρ) for the steel straps and GFRP bars is provided in Table 3.5.

Table 3.5 - Reinforcement ratio for steel straps and GFRP reinforcement

Layer	Material	Area of Steel Straps and GFRP Bars, A_s, A_{FRP} (mm^2)	Width, b (mm)	Effective Depth, d (mm)	Reinforcement Ratio, ρ (%)
Transverse Steel Strap	Steel	5000	4595	259	0.42
Bottom-Transverse	GFRP	720.0	4595	170	0.09
Bottom-Longitudinal	GFRP	997.6	6500	160	0.10
Top-Transverse	GFRP	13000.0	4595	63	4.49
Top-Longitudinal	GFRP	997.6	6500	80	0.19

It should be noted, as previously stated, that both sections of the deck contain similar reinforcement ratios with respect to their primary bottom transverse reinforcement (bottom transverse steel bars in Segment A and external steel straps in Segment B). More specifically, the reinforcement ratio for the bottom transverse steel reinforcement in Segment A was 0.39% and close to in nature, the reinforcement ratio for the external steel straps in Segment B was 0.42%.

3.4.3 Design Summary

The concrete bridge deck slab design for this experiment was conceptually divided into two segments; Segment A representing a conventionally steel reinforced concrete slab and Segment B, representing a steel-free concrete slab. Ultimately, the main difference between Segments A and B were the methods used to reinforce each section. Segment A contained two orthogonal mats of deformed steel bars for reinforcement and Segment B received its primary reinforcement from partially studded steel straps embedded in the concrete haunches, and resting just above the top flanges of the girders. Segment B also incorporated a bottom and top mat of crack control GFRP bars. The overall reinforcement summary of Segments A and B is outlined in Tables 3.6 and 3.7, respectively. Figures 3.4 and 3.5 illustrate plan views of Segments A and B with regards to the top and bottom internal reinforcement placement, respectively. Figure 3.6 highlights the location of the partially studded steel straps in Segment B; and Figures 3.7 and 3.8 depict typical cross-sectional views of Segments A and B, respectively.

Table 3.6 Reinforcement summary for Segment A

Segment A (Conventional Steel Reinforced)						
Layer	Material	Type	Size	Spacing	Effective Depth	Reinforcement Ratio
				(mm)	(mm)	(%)
Bottom-Transverse	Steel	Deformed Steel Bars	15M	300	167	0.39
Bottom-Longitudinal	Steel	Deformed Steel Bars	15M	300	151	0.47
Top-Transverse	Steel	Deformed Steel Bars	15M	100	67	2.92
Top-Longitudinal	Steel	Deformed Steel Bars	15M	300	83	0.85

Table 3.7 Reinforcement summary for Segment B

Segment B (Steel-Free)						
Layer	Material	Type	Size	Spacing	Effective Depth	Reinforcement Ratio
				(mm)	(mm)	(%)
External Bottom-Transverse	Steel	Steel Strap	25 x 50 mm	1200	259	0.42
Bottom-Transverse	GFRP	Pultrall V-Rod	#10	500	170	0.09
Bottom-Longitudinal	GFRP	Pultrall V-Rod	#10	500	160	0.10
Top-Transverse	GFRP	Pultrall V-Rod	#10	175	63	4.49
Top-Longitudinal	GFRP	Pultrall V-Rod	#10	500	80	0.19

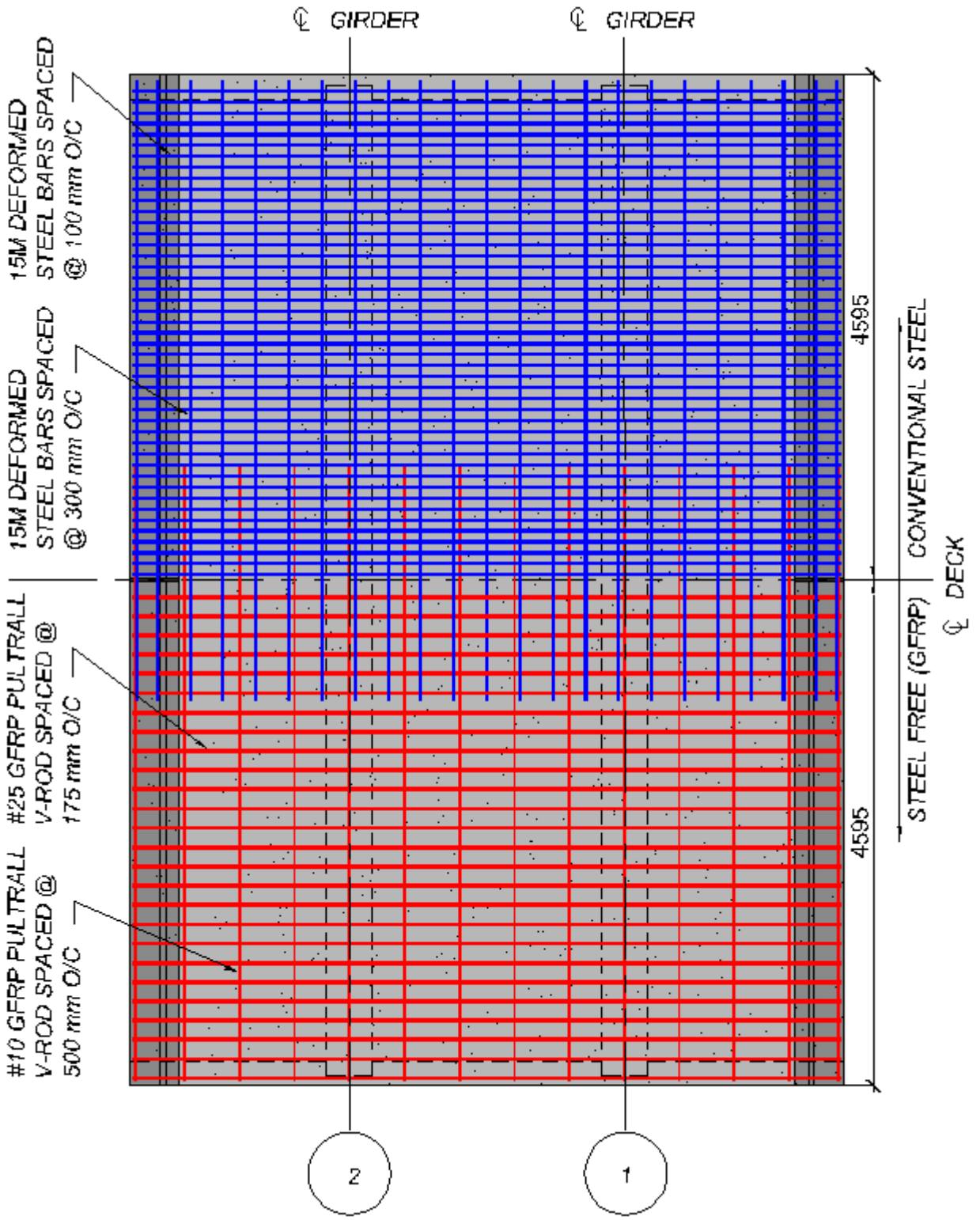

Figure 3.4 Plan view of concrete bridge deck slab with top internal reinforcement schematic used in this experiment.

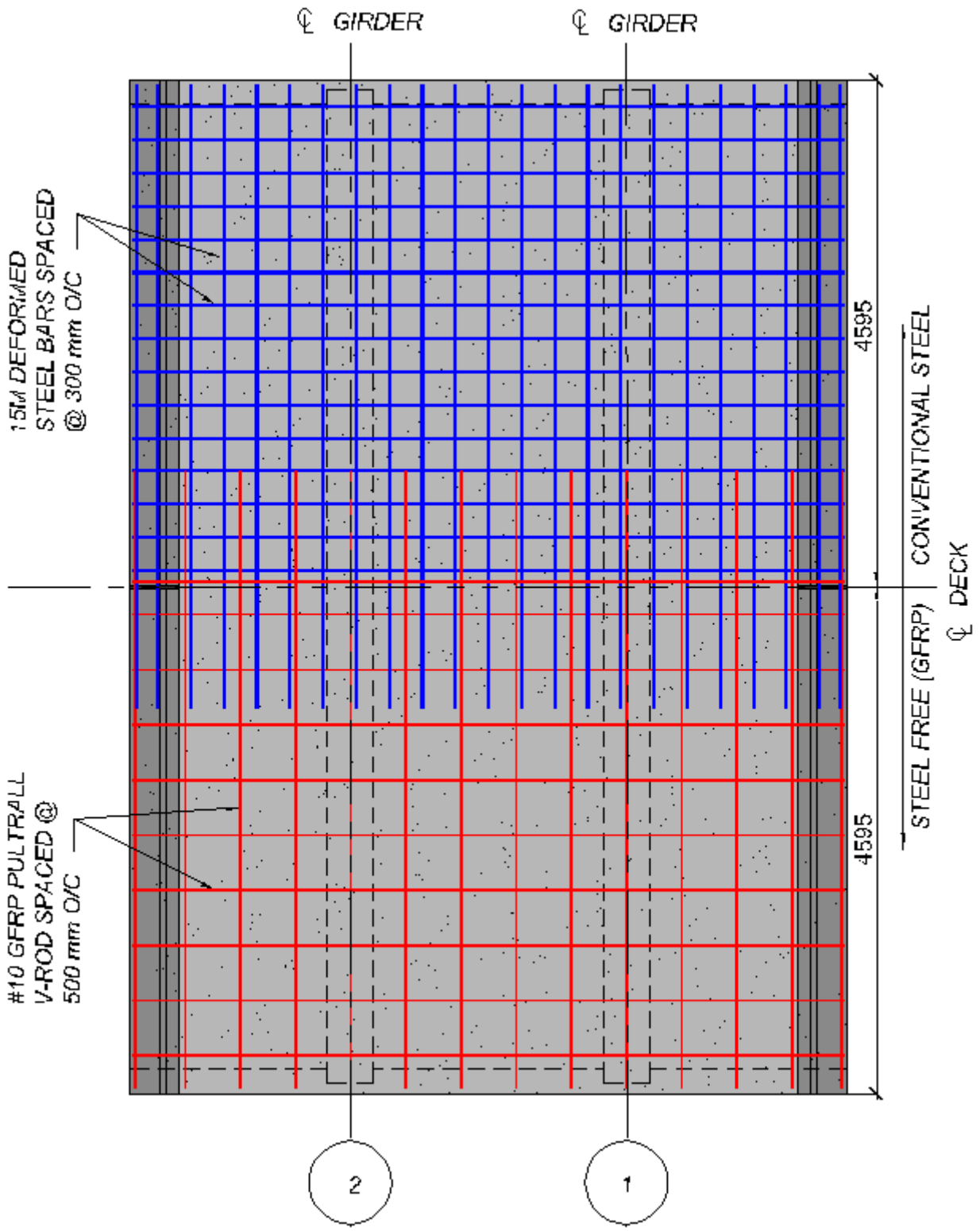

Figure 3.5 Plan view of concrete bridge deck slab with bottom internal reinforcement schematic used in this experiment

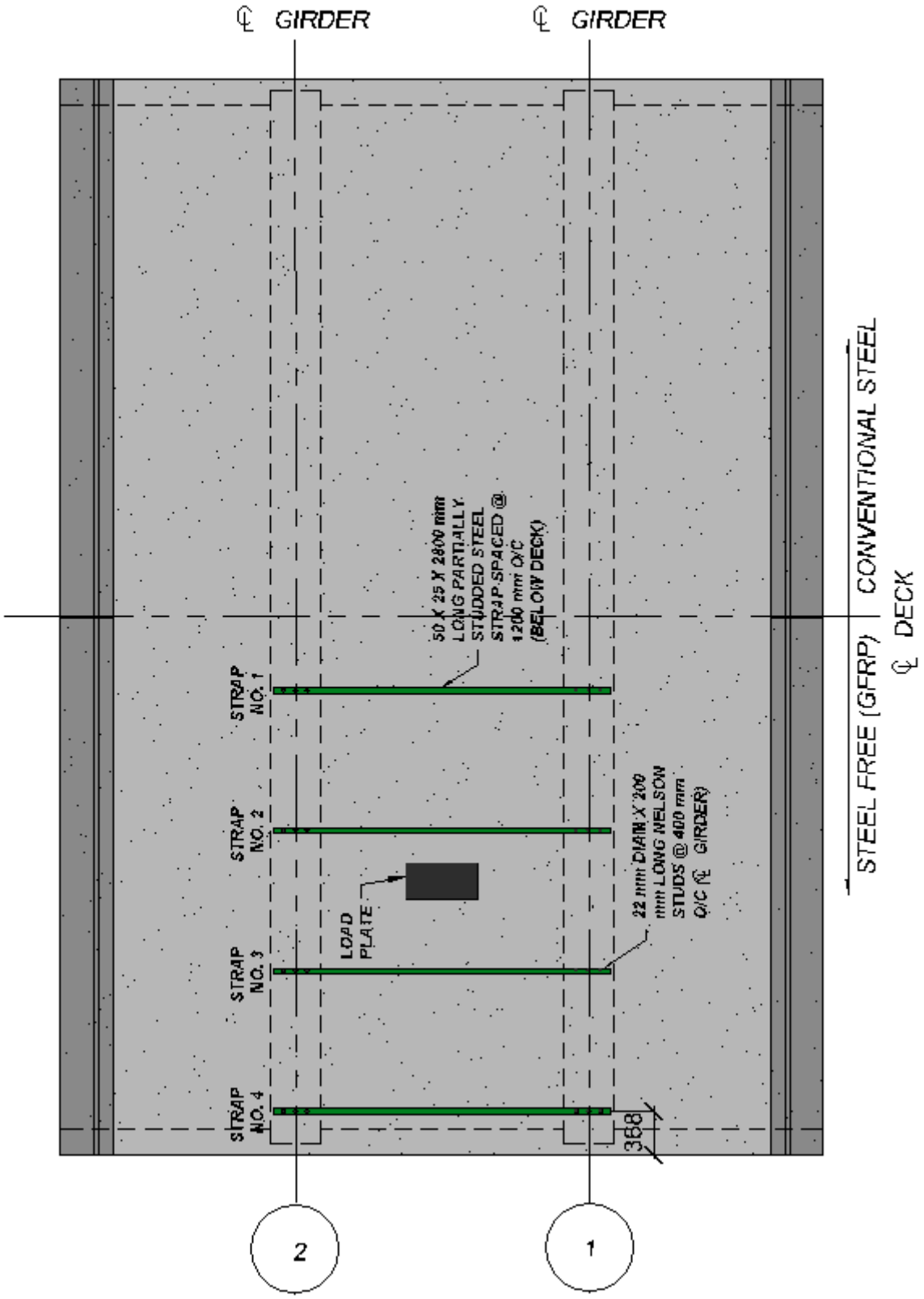

Figure 3.6 Plan view of concrete bridge deck slab with bottom external reinforcement schematic (steel-free only) used in this experiment

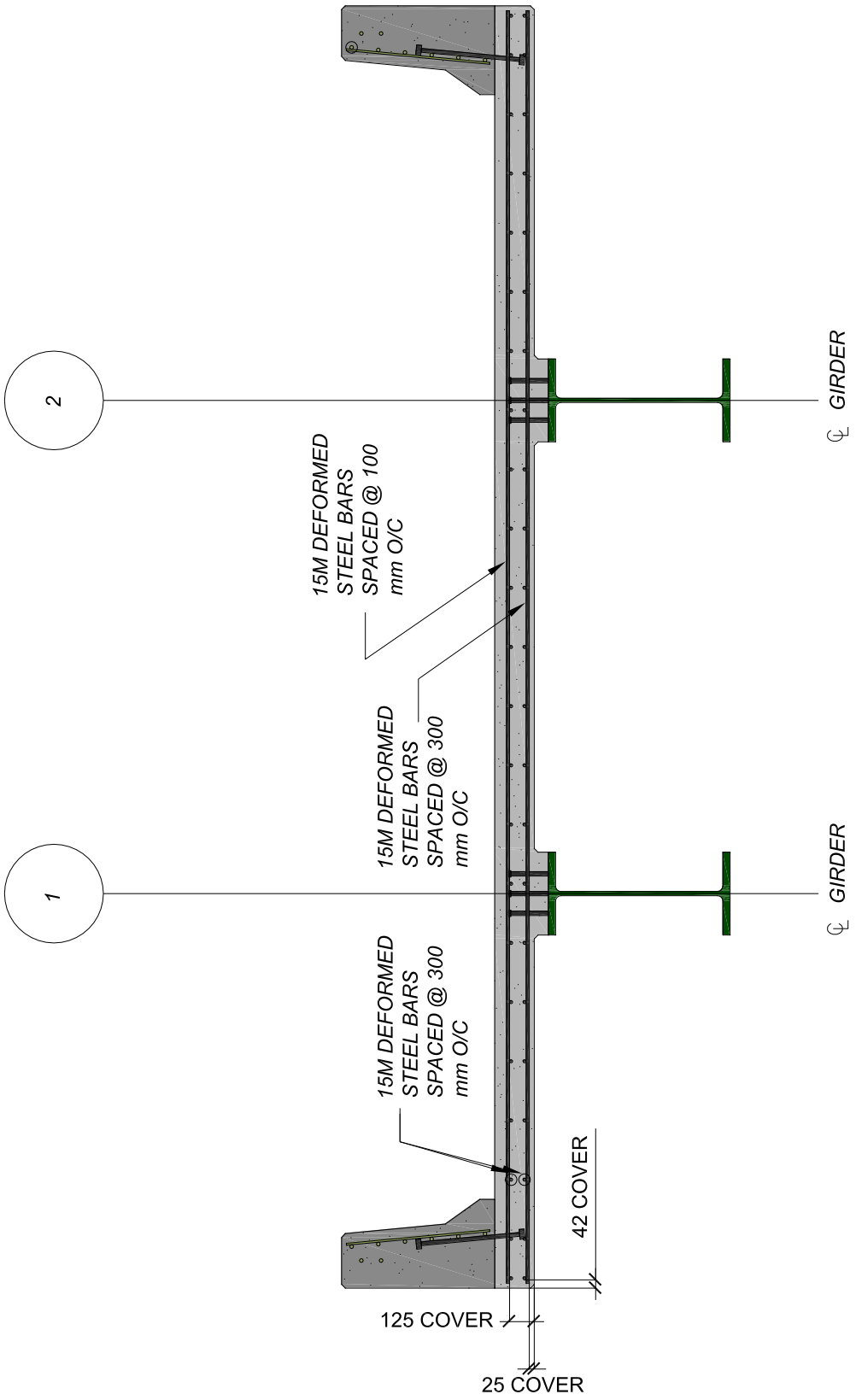

Figure 3.7 Cross section view of Segment A: Conventional steel reinforced concrete bridge deck slab

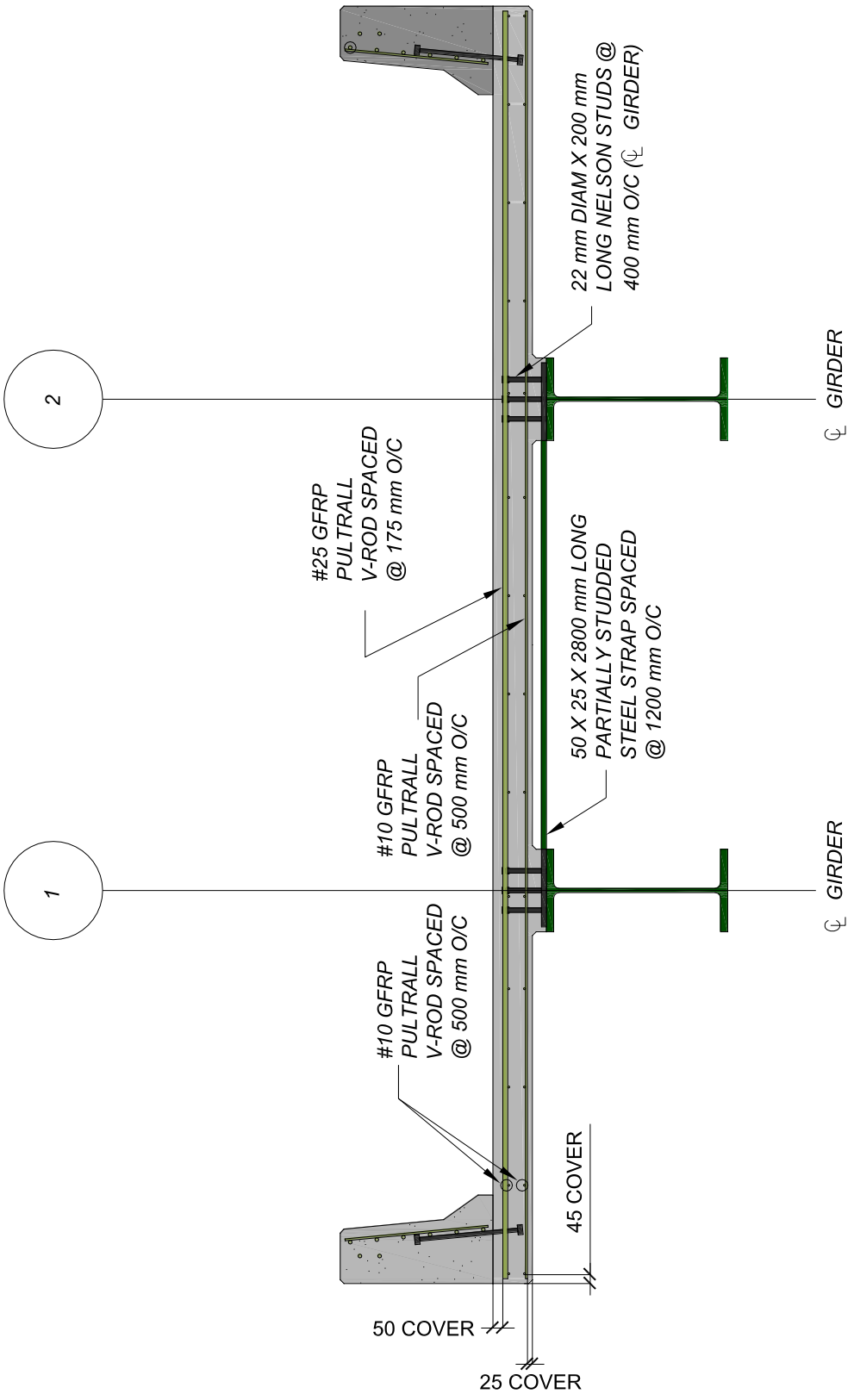

Figure 3.8 Cross section view of Segment B: Steel-free reinforced concrete bridge deck slab

Chapter 4

Test Program

4.1 General

The test program for Segments A and B consisted of a number of instrumentation apparatuses including the likes of linear variable displacement transducers (LVDT), pi gauges, a data acquisition system, and a collection of strain gauges. The aim of the test program was to provide a wide variety of data recording methods. The main goal was to acquire a compilation of conclusive data that would provide the means for a thorough analysis to materialize and eventually lead to a valuable comparison between the two fatigue tests conducted on Segments A and B. The instrumentation provided, focused on recording data with respect to displacement, crack width, internal reinforcement strain, external reinforcement strain, concrete strain and load measurement. Albeit, it should be noted that even before the test program could be tried, a testing scheme concerning load application and magnitude needed to be developed.

4.2 Testing Scheme

In an effort to compare steel-free and empirical design methods with respect to fatigue endurance, structural integrity, and overall performance, both bridge deck segments were subjected to identical testing schemes. The testing scheme established for this experiment was based on analysis conducted in the following three categories:

1) Finite Element Analysis
2) PUNCH Program Analysis

3) Fatigue Life Estimation Model Analysis

Using the combined results from the finite analysis, the PUNCH program analysis and the fatigue life estimation models, it was decided to load the internal panels of Segments A and B with an identical continuous fatigue load of 570 kN until punching failure was reached. The testing scheme for Segments A and B is shown in Figure 4.1.

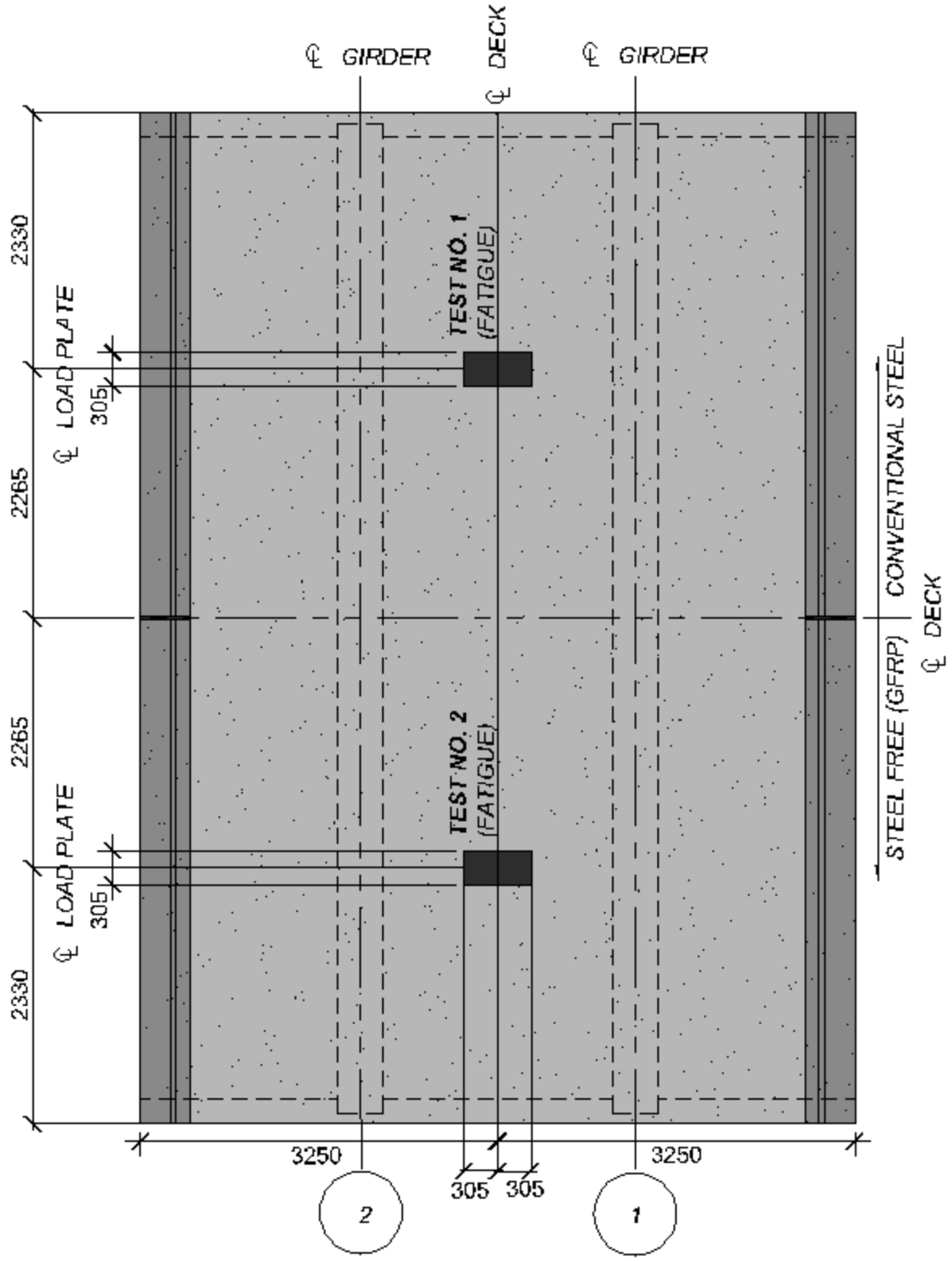

Figure 4.1 Plan view of testing scheme used in this experiment

4.2.1 Finite Element Analysis

Using the design parameters of the steel-free and steel reinforced concrete bridge deck slabs formulated in Chapter 3, a finite element analysis of the girders and adjacent reinforcement was conducted to determine the transverse restraint stiffness, k, for Segments A and B. The finite element program RISA-2D was chosen for the modeling and analysis of the girders and reinforcement.

The girders and reinforcement were modeled as beams and springs, respectively, in a beam on elastic spring supports model. The beams were modeled based on the top flanges of each girder, thereby neglecting the properties of the web and bottom flange. The springs in the model represented a combination of reinforcement including steel rebar, GFRP crack control bars, transverse steel straps, and diaphragm angles (edge beam angles). Only the properties of the bottom transverse reinforcement layers within the concrete deck of Segments A and B were considered in this model; all longitudinal and top reinforcement layers were ignored. The beam on springs input parameters used to construct and analyze the model in RISA-2D are presented in Table 4.1. The model apparatus used for analysis in RISA-2D is illustrated in Figure 4.2.

Table 4.1 Beam on springs model input parameters used in Risa-2D program

Elastic Spring Parameters	**Modulus of Elasticity (GPa)**	**Cross-Sectional Area (m^2)**	**Length (m^2)**	**Axial Stiffness (N/mm)**
Symbol/Equation =>	E	A	S_l	$\frac{E \times A}{\frac{S_l}{2}}$
Transverse Steel Strap	200	1,250	2,278	219,491
Double Angle	200	5,980	2,200	1,087,272
Steel Bar	200	200	1,791	44,693
GFRP Bar	46	71.3	1,791	3,665
Beam Parameters	**Moment of Inertia (mm^4)**			
Top Flange	228×10^6			

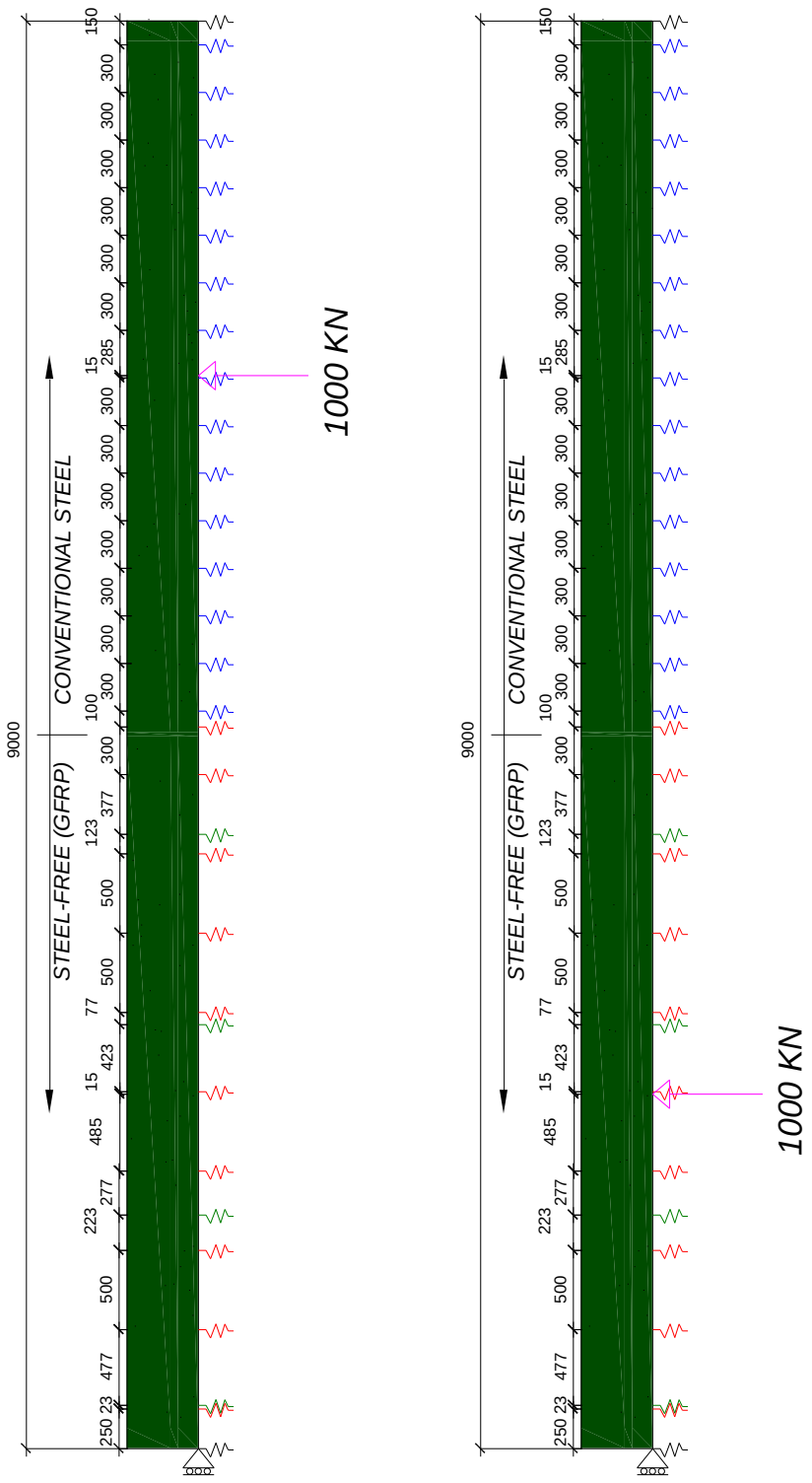

Figure 4.2 Beam on elastic springs model schematic. Blue springs indicate steel rebar; red springs indicate GFRP reinforcement; green springs indicate transverse steel straps; and black springs indicate double edge angles

The different colored springs in the model represent each type of reinforcement, and the dimensions show the actual location of the reinforcement on the real structure. To determine the transverse restraint stiffness, k, for Segments A and B, a unit load of 1000 kN was placed in the model at the same location where the actual loading on the real structure is situated. Upon analyzing the model in RISA 2-D, the resulting deflections at the location of the unit loads were obtained and used to calculate the corresponding transverse restraint stiffness, k, values for Segments A and B. The results from the model analysis are presented in Table 4.2. The values obtained for transverse restraint stiffness, k, were then used as input parameters in the program PUNCH, to estimate the ultimate static punching shear capacity of the two segments; see Section 4.2.2 for further discussion.

Table 4.2 Beam on springs model RISA-2D deflection results at a unit load of 1,000 kN; corresponding transverse restraint stiffness, k, for Segments A and B

Model Segment	Applied Unit Load (KN)	Resulting Deflection (mm)	Transverse Restraint Stiffness, k, (N/mm/mm)
A (Steel-Reinforced)	1000	3.436	291
B (Steel-Free)	1000	3.054	327

4.2.2 PUNCH Program Analysis

PUNCH is a program developed by [Mufti and Newhook (1998)] to predict the behavior of laterally restrained concrete slab-on-girder bridge decks under heavy wheel loading. Details of the program are discussed in former Section 2.2.2. The input parameters used in the PUNCH program for this experiment are provided in Table 4.3, along with the output estimates for ultimate deflection and ultimate static punching shear capacity. The PUNCH Program predicted that Segments A and B had ultimate static punching shear capacities of 984 kN and 1,087 kN, respectively.

Table 4.3 PUNCH program input parameters for Segments A and B

PUNCH Parameters	Segment A		Segment B	
	Input	Output	Input	Output
Clear Span Between Girders (mm)	2,500		2,500	
Diameter of Equivalent Circle for Load (mm)	579		579	
Maximum Compressive Stress of Concrete (MPa)	40.7		44.5	
Elastic Axial Stiffness of Strap (N/mm/mm)	291		327	
Strap to Load Spacing (mm)	0		438	
Depth Of Slab (mm)	200		200	
Beta to Define Rectangular Stress Block	0.75		0.75	
Concrete Constant used for confinement	10		10	
Area of Load Patch (mm^2)	184,500		184,500	
Yield strain	0.002		0.002	
Predicted Ultimate Deflection (mm)		20.01		19.87
Predicted Ultimate Shear Punch Load (KN)		984		1,087

4.2.3 Fatigue Life Estimation Model Analysis

The objective was to apply an equivalent fatigue load to Segments A and B, and observe the number of cycles required for each deck to fail in punching shear. Subsequently, there needed to be a middle ground between both tests concerning load magnitude that would ensure premature failure did not take place, and on the contrary, the decks would not continue to resist loading beyond a reasonable time frame. In that case, it was decided that the best method to predict load cycles would be to use previous research involving Fatigue Life Estimation Models. The Fatigue Life Estimation Models considered in this experiment are discussed in detail in previous Section 2.4.

Table 4.4 outlines the “selection by trial” methodology that was used to determine an applied fatigue load that was satisfactory for this experiment. Fatigue Life Estimation Models are based on the ratio between the applied load and the ultimate static punching shear capacity. Using the PUNCH program, Segments A and B were predicted to have punching shear capacities of 984 kN and 1087 kN, respectively, as shown in Section 4.2.2. After several iterations using the Fatigue Life Estimation Models, an applied load of 570 kN appeared satisfactory for this experiment. 570 kN provided an applied load to ultimate static shear capacity ratio of 0.579 and 0.524 for Segments A and B, respectively. The Fatigue Life Estimation Models suggested that at ratios of 0.579 and 0.524, respective Segments A and B would fail in a time frame that was considered reasonable based on the fact that the test was occupying valuable lab time and space. Specifically, 1,000,000 cycles per segment was the greatest number of cycles considered appropriate before testing would start to consume too much valuable lab time and space. All the Fatigue Life Estimation Models, with the exception of “Batchelor” and “Mufti”, suggested that an applied load of 570 kN would produce a number of load cycles to failure equal to or below 1,000,000 cycles. For this, an applied load of 570 kN was chosen to be used for fatigue loading in both Segments A and B.

Table 4.4 Fatigue life estimation models (refer to Section 2.4 for fatigue life estimation model expressions); "selection by trial" methodology

Fatigue Life Estimation Models		
	Steel Reinforced	**Steel-Free**
Applied Load, P	570	570
Static Punching Shear Capacity, P_s	984	1087
P/P_s	0.579	0.524
log(P/Ps)	-0.2371	-0.2804
	Number of Cycles to Failure	
Batchelor	10,719,552	
Young	1,017,865	
Matsui	221,312	791,121
Mufti	300,188	1,592,736
Memon		
c = 5.737 (GFRP)		290,920
c = 6.104 (GFRP)		650,572
c = 4.4138 (RC)	5,776	
Memon/Mufti		
M = 26.5(GFRP)		299,110
M = 20.5(RC)	5,588	
El Ragaby	69,698	323,160

4.3 Instrumentation Types and Nomenclature

4.3.1 Nomenclature

Due to the significant variety and number of instruments used in this project, all the drawings in Chapter 4 use short form abbreviations for all the different types of instrument names and groups. Table 4.5 lists the general short form and corresponding full name for each group of instruments used in the figures found throughout Chapter 4.

Table 4.5 Nomenclature used in this experiment

Short Form (Abbreviated Name)	Full Name
LVDT NO. 1-S	Linear Variable Displacement Transducer, Number 1, Steel Reinforced Section
LVDT NO. 1-SF	Linear Variable Displacement Transducer, Number 1, Steel-Free Section
PI GAUGE NO. 1-S	Pi Gauge, Number 1, Steel Reinforced Section
PI GAUGE NO. 1-SF	Pi Gauge, Number 1, Steel-Free Section
ESG NO. 1-S-B	Electronic Strain Gauge, Number 1, Steel Reinforced Section, Bottom Reinforcement
ESG NO. 1-S-T	Electronic Strain Gauge, Number 1, Steel Reinforced Section, Top Reinforcement
ESG NO. 1-SF-B	Electronic Strain Gauge, Number 1, Steel-Free Section, Bottom Reinforcement
ESG NO. 1-SF-T	Electronic Strain Gauge, Number 1, Steel-Free Section, Top Reinforcement
STRAP ESG NO. 1	External Steel Strap, Electronic Strain Gauge, Number 1
CONC ESG S	Concrete, Electronic Strain Gauge, Steel Reinforced Section
CONC ESG SF	Concrete, Electronic Strain Gauge, Steel-Free Section

4.3.2 Load Measurement

Each internal panel test assumed one position and remained stationary throughout the entire loading. The load cell's location was mirrored for the steel reinforced and steel-free tests, as shown previously in Figure 4.1. The load cell was attached to a hydraulic actuator which was connected to a data acquisition system, where the data was recorded and saved.

4.3.3 Displacement

Deflections of the two internal panel fatigue tests were recorded using linear variable displacement transducers (LVDT). Deflections were only recorded at the location of the load application. For each fatigue test, two LVDT's were positioned along the longitudinal center of the deck, on each side of the loading pad, at a distance of 200 mm from the center of the loading pad. Two steel uni-strut beams complete with threaded rods and clamps were used to support the LVDT's in their desired positions. The two uni-struts were supported on steel supports placed over the center-lines of the girders. As a result, the internal panel displacements were measured with respect to the deflections of the steel girders. Data recorded by the LVDT's were transferred to a data acquisition system via extension cables and saved for further analysis. See Figure 4.3 for a detailed plan view of the LVDT positioning, and Figure 4.4 for an actual photo of the LVDT setup.

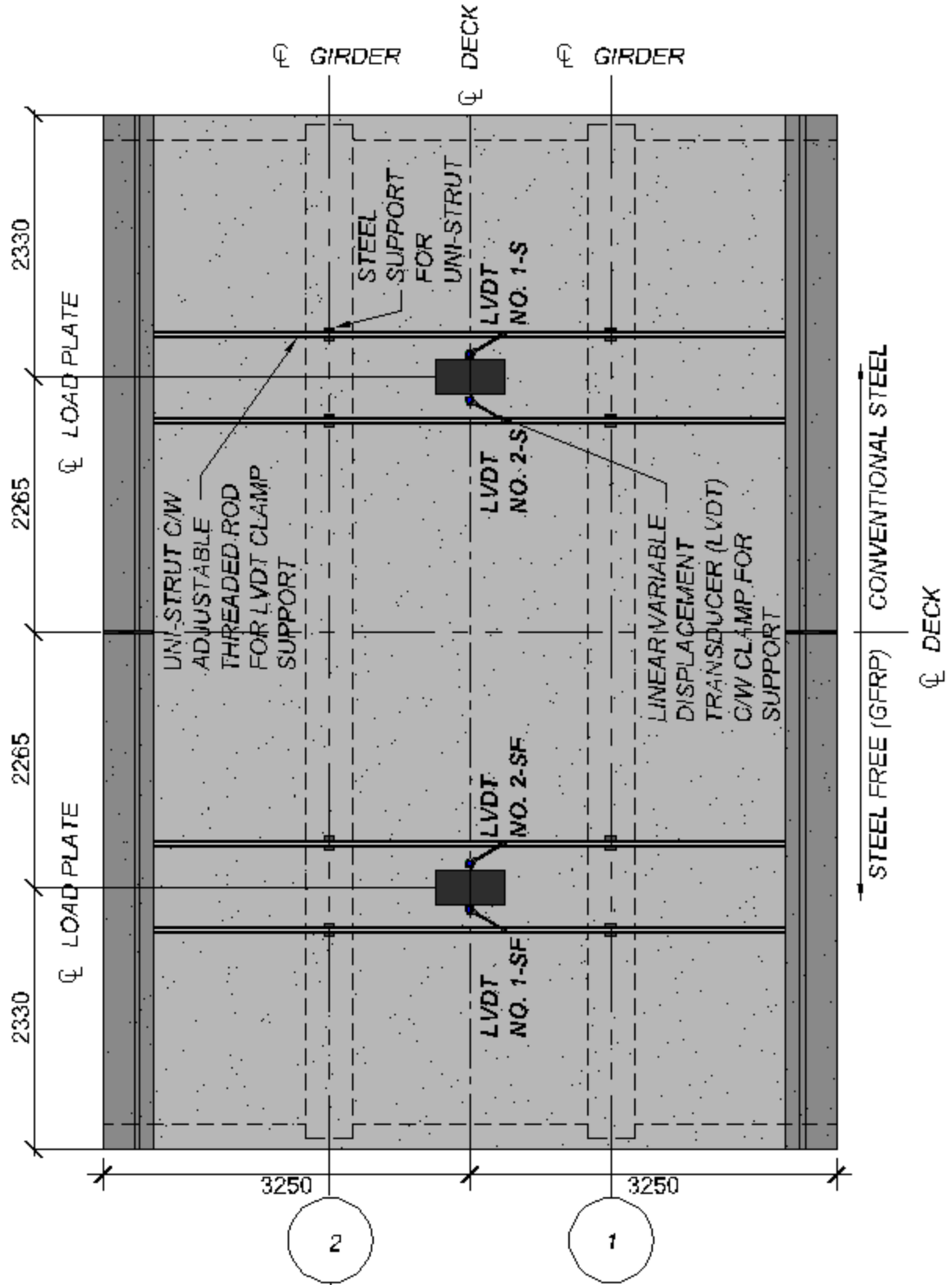

Figure 4.3 Plan view of the LVDT program used in the experiment

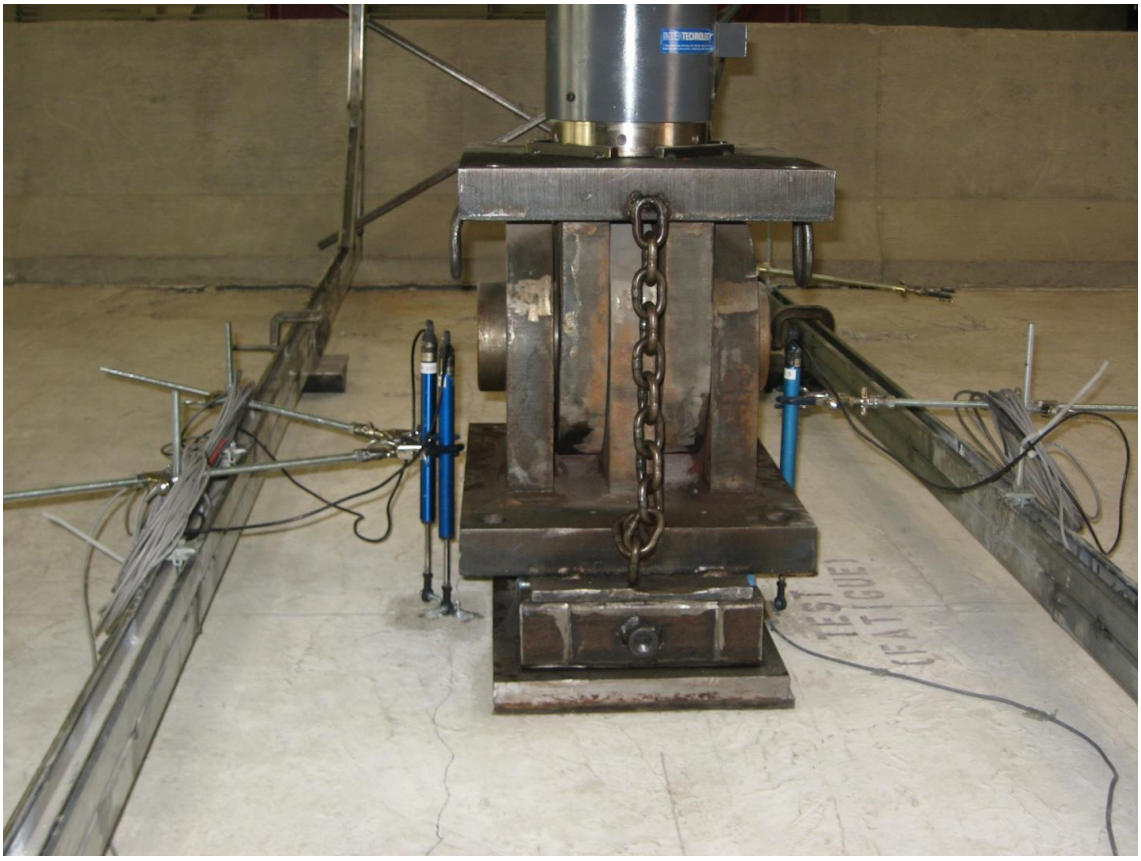

Figure 4.4 LVDT setup in Segment A

4.3.4 Crack Width

Pi gauges with a gauge length of 200 mm were used to measure crack widths at several locations on the deck. The original goal was to place the pi gauges in mirrored positions in Segments A and B, but unfortunately crack dispersion was random and only one pi gauge location (sole top of deck pi gauge) was able to be replicated for both tests. Subsequently, the pi gauges were placed over random cracks; for example, visible cracks that suggested good data could be extracted as loading progressed. On the contrary, the number of pi gauges used in both tests was identical, equating to four per test; three on the underside or soffit of the deck, and one on the top of the deck. Data recorded by the pi gauges was transferred to a data acquisition system via extension cables and saved for future analysis. A plan view of the pi gauge program is illustrated in Figure 4.5. Figure 4.6 is a photo of the pi gauge layout in Segment A.

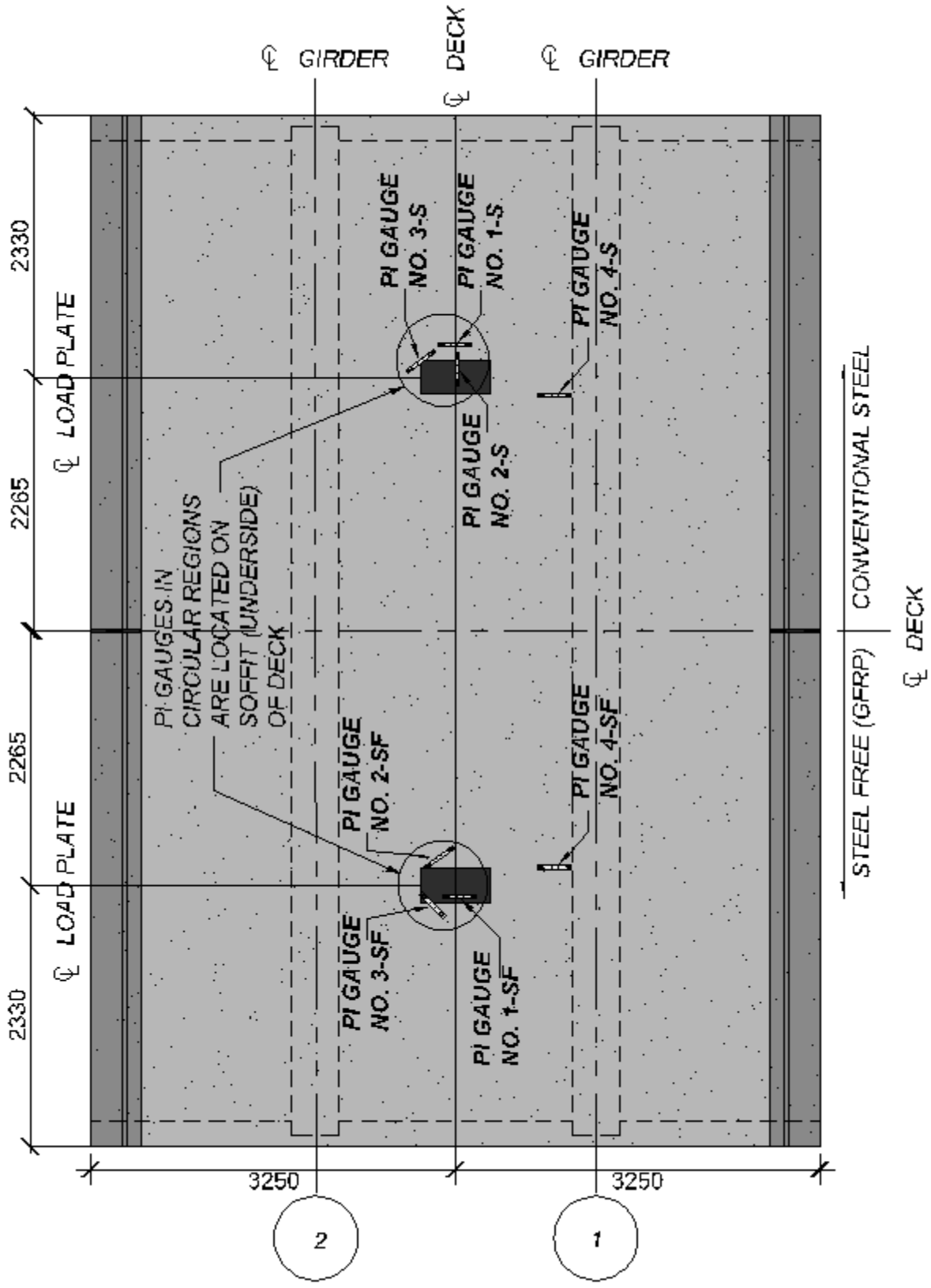

Figure 4.5 Pi Gauge program used in this experiment

Figure 4.6 Pi gauge arrangement in Segment A

4.3.5 Internal and External Reinforcement Strain

During the construction phase, select internal reinforcing bars (steel and GFRP) were equipped with 12 mm electronic strain gauges. The strain gauges were generally located along the centerline of the load plate (i.e. longitudinal bars) or along the longitudinal centerline of the deck (i.e. transverse bars), as shown in Figures 4.7 and 4.8. All the strain gauge wires were gathered into rigid PVC conduit, which rested in the haunches of the bridge deck. Figure 4.9 shows several strain gauges attached to GFRP bars in Segment B prior to concrete placement. The conventional steel reinforced section of the deck incorporated 11 strain gauges, while the steel-free portion of the deck contained 10.

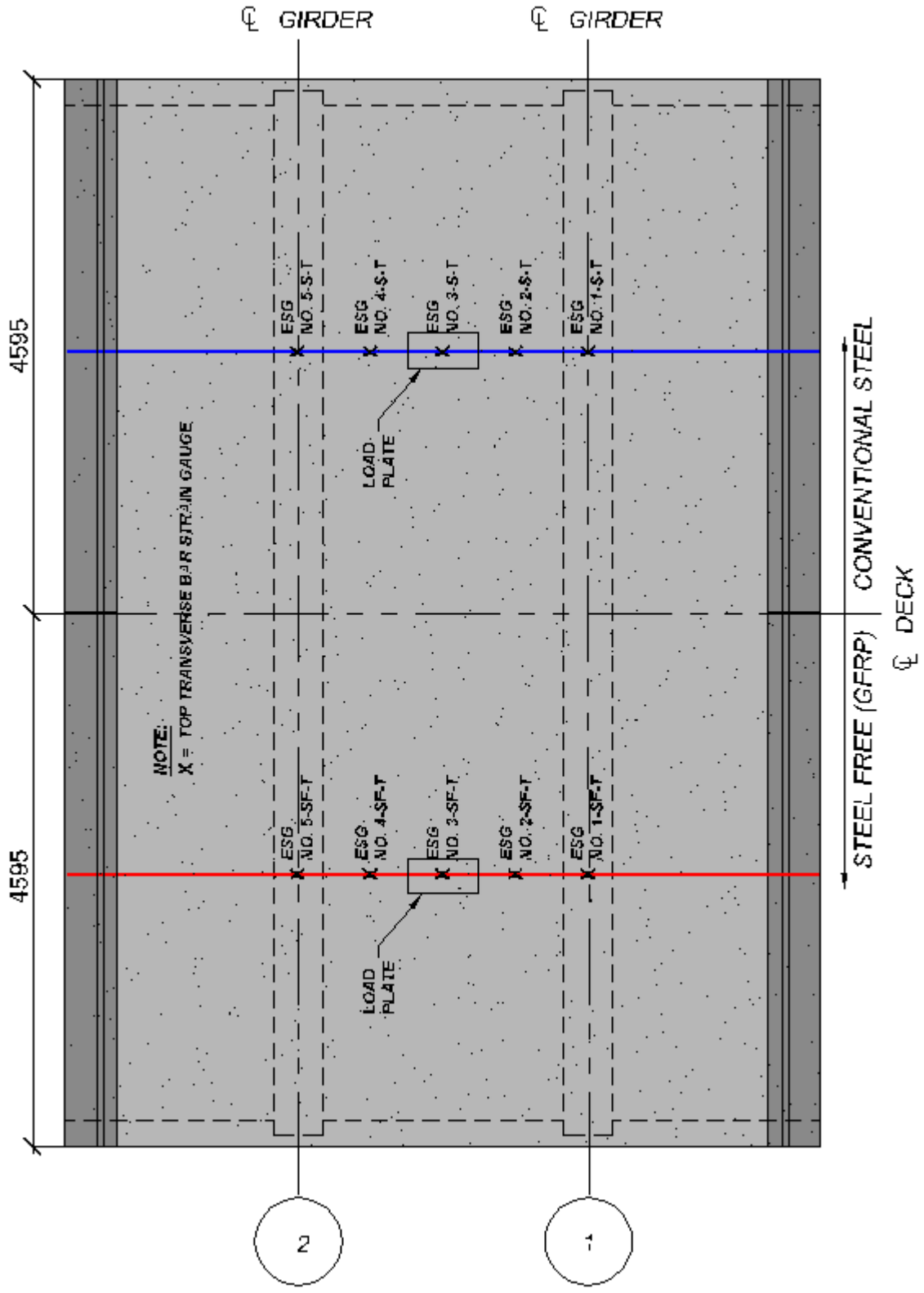

Figure 4.7 Plan view (from above) of the top internal reinforcement strain gauge program used in this experiment

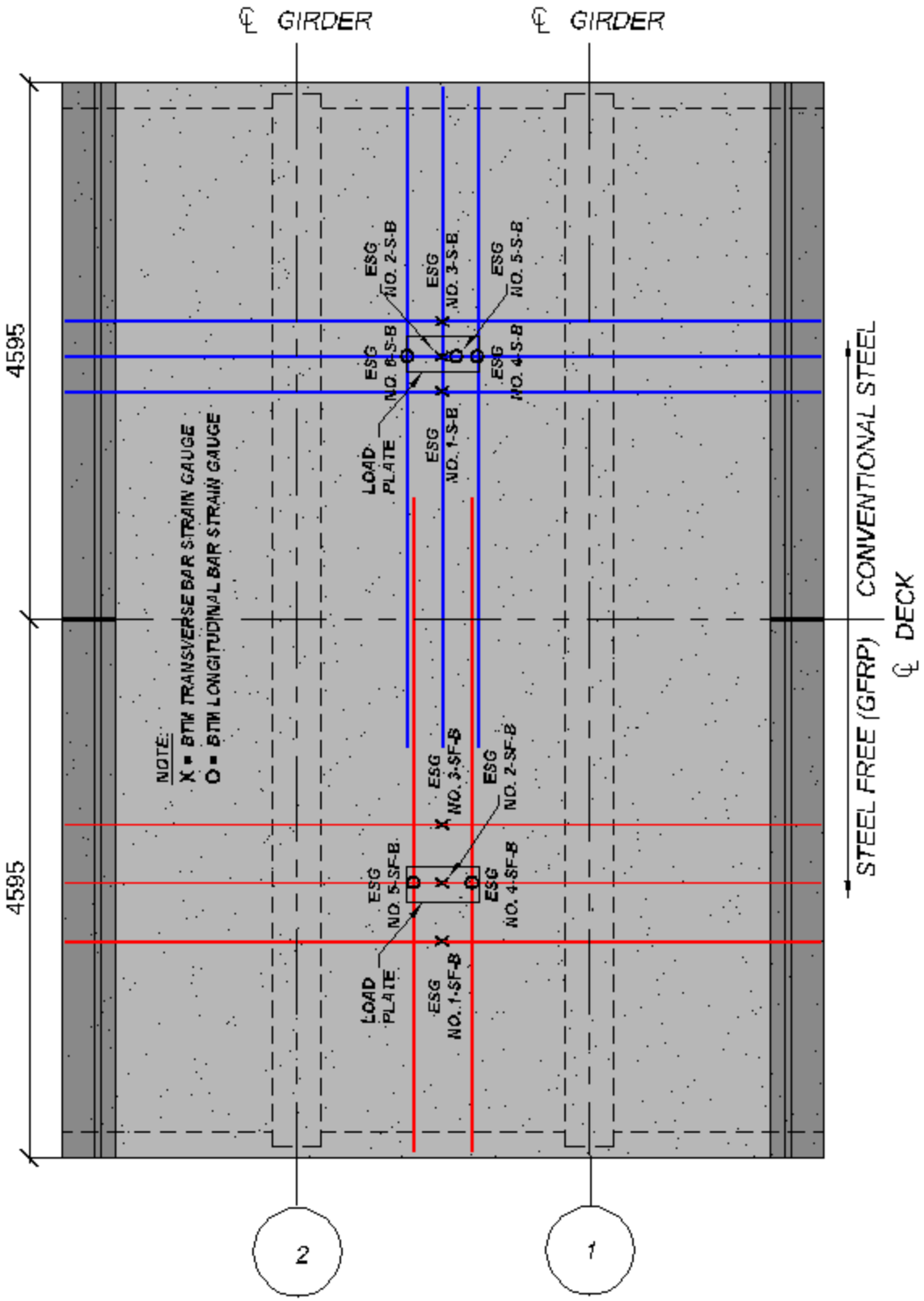

Figure 4.8 Plan view of the bottom internal reinforcement strain gauge program used in this experiment

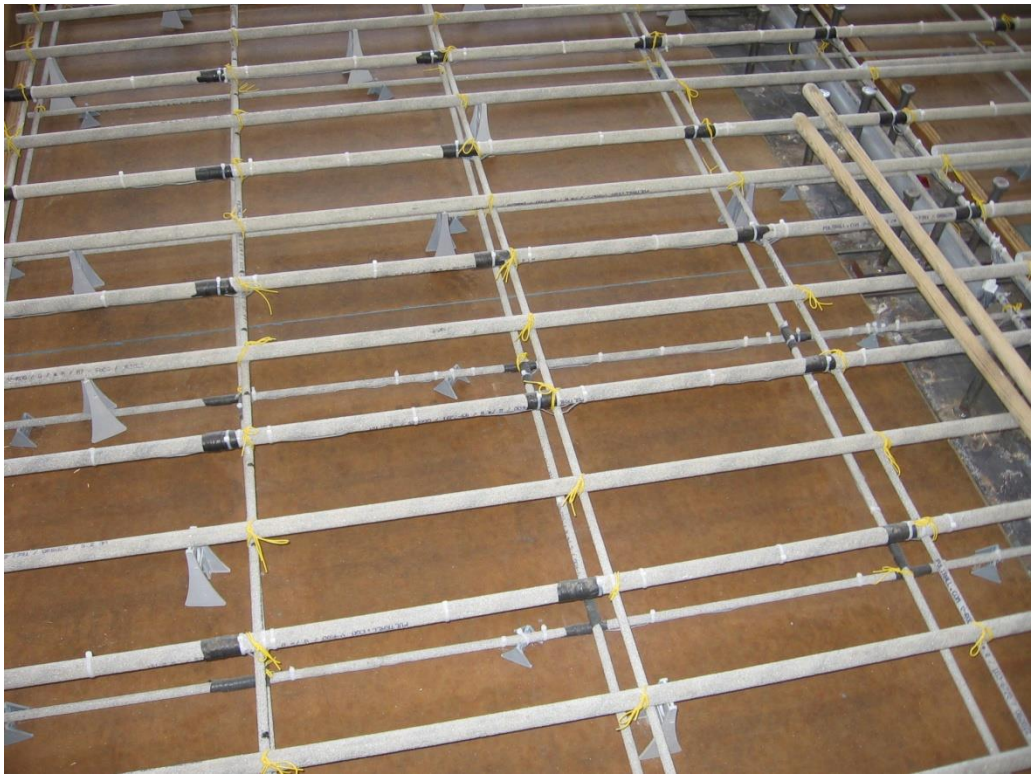

Figure 4.9 Strain gauges attached to GFRP bars in Segment B

In addition to the internal GFRP crack control reinforcement, Segment B had four external steel reinforcing straps which were also equipped with 6 mm electronic strain gauges. The strain gauges were attached directly to the underside and center of the steel straps, right in line with the longitudinal center of the deck, as shown in Figure 4.10. Figure 4.11 is a photo of the transverse steel straps from a distance, and Figure 4.12 is a close up of a strain gauge attached to a steel strap. All strain gauges were connected to a data acquisition system which recorded and saved the extracted data for future analysis.

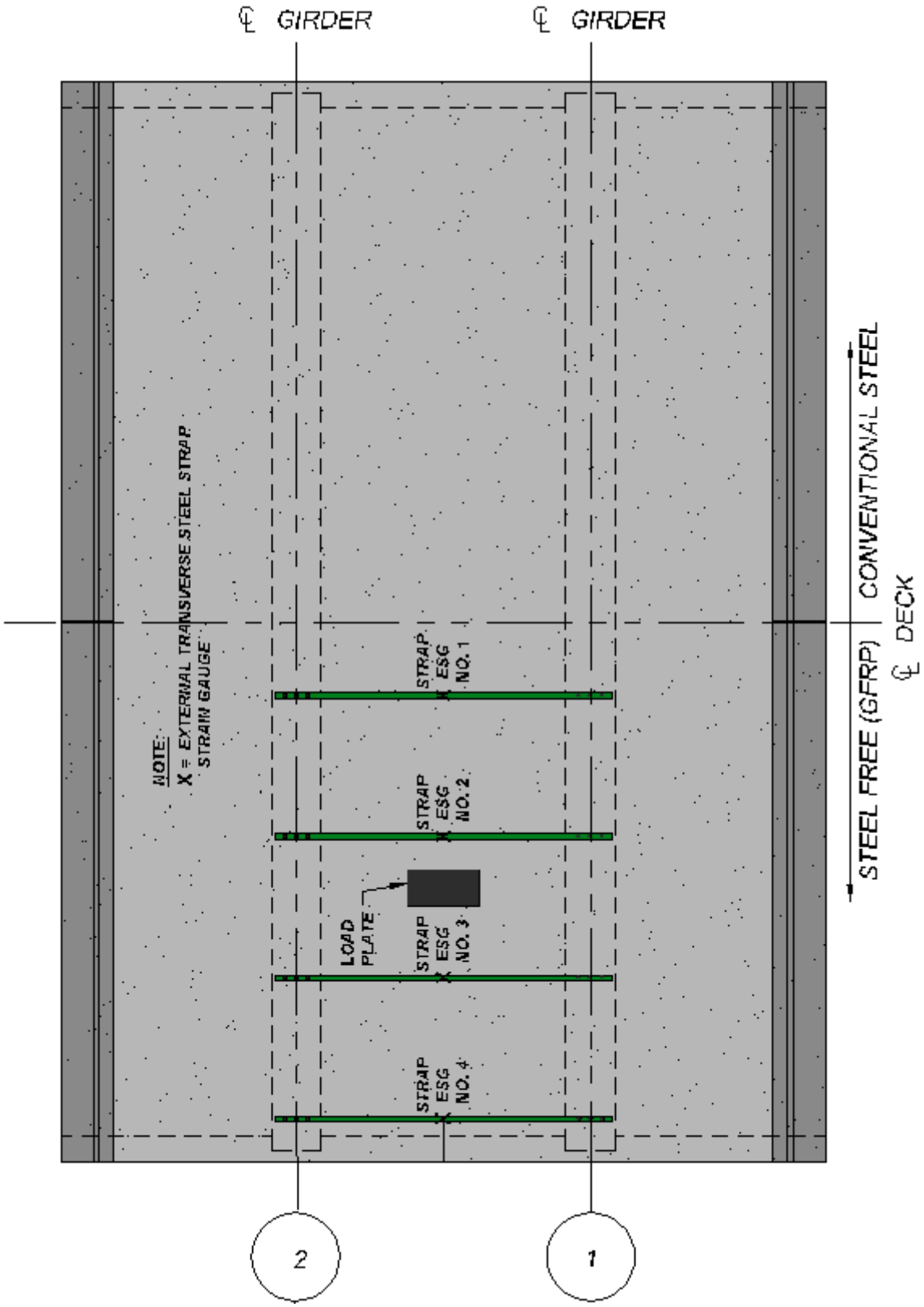

Figure 4.10 Plan view (from above) of the bottom external transverse steel strap strain gauge program used in this experiment

Figure 4.11 Transverse steel straps below the bridge deck

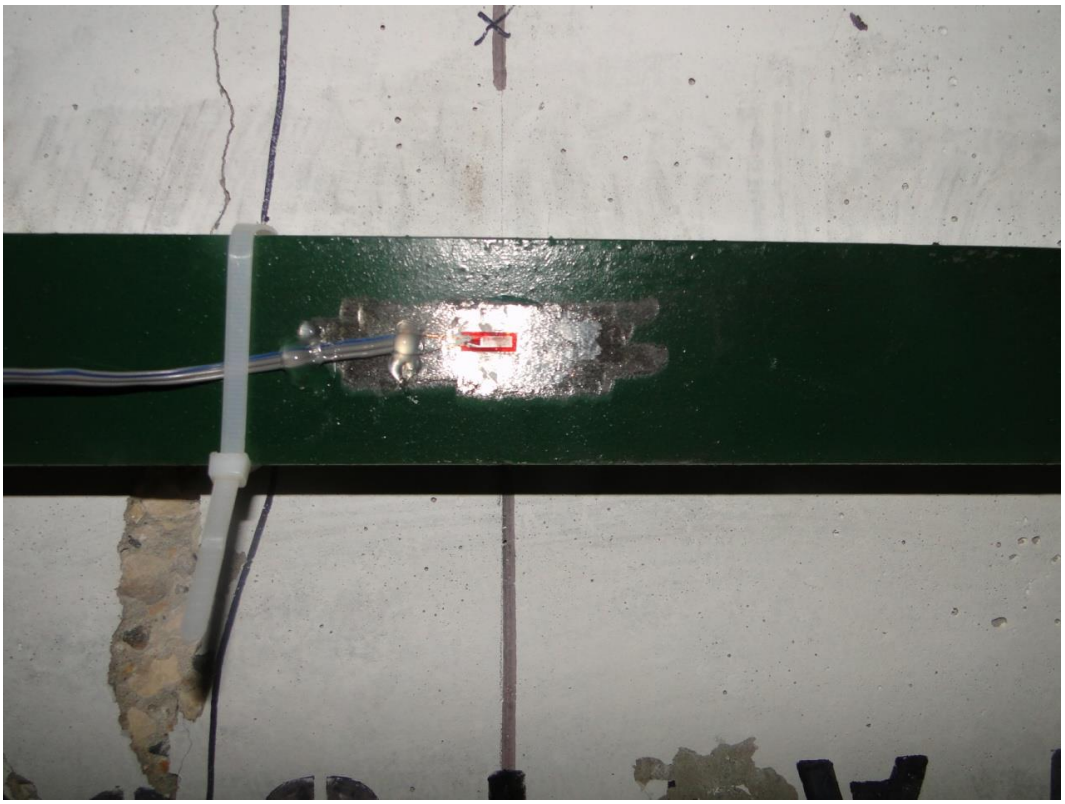

Figure 4.12 Close up photo of a strain gauge attached to a steel strap

4.3.6 Concrete Strain

In an effort to measure the concrete strain near the load plate, concrete strain gauges were installed on the top side of the deck within close proximity to the load imprint. One concrete strain gauge was used per fatigue test, as shown in Figure 4.14. Figure 4.13 shows the installed concrete strain gauge. All strain gauges were connected to a data acquisition system which recorded and saved the extracted data for future analysis.

Figure 4.13 Concrete strain gauge

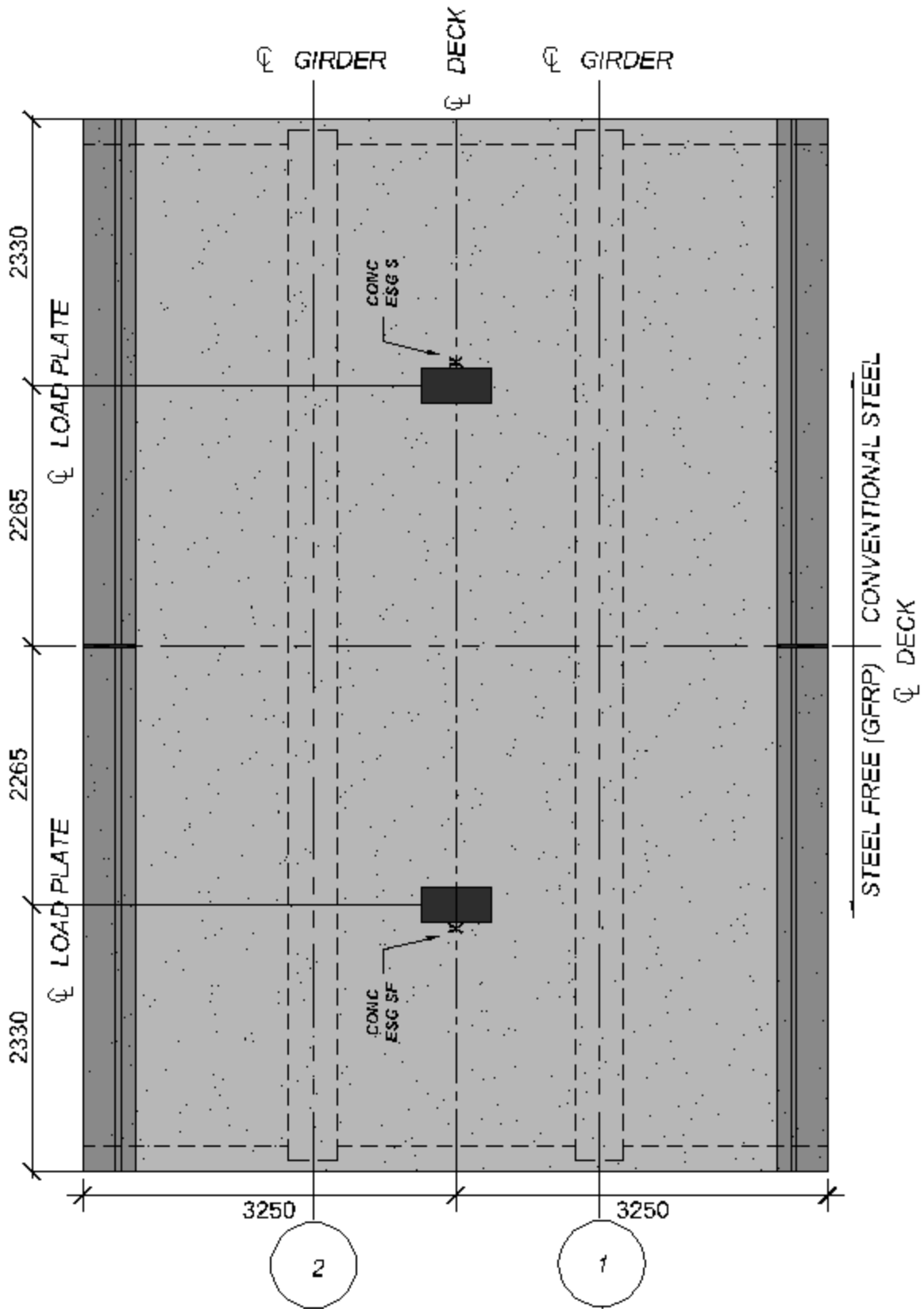

Figure 4.14 Plan view of the concrete strain gauge program used in this experiment

Chapter 5

Test Results

5.1 General

The full-scale concrete bridge deck slab was conceptually divided into two segments with overall dimensions of 9,190 mm longitudinally and 6,500 mm transversely. Segment A was a conventionally reinforced concrete bridge deck slab with two top and bottom orthogonal steel mats, while Segment B was a steel-free concrete bridge deck slab containing external steel straps as primary reinforcement and additional internal GFRP reinforcement for crack control.

An overall six tests were conducted on the full-scale specimen; however, only two of the six experimental tests are discussed here. The six tests comprised of two internal panel fatigue tests, two cantilever fatigue tests and two cantilever static tests. The scope of this thesis is limited to the two internal panel fatigue tests. The experimental results and analysis for the four cantilever tests were recorded and discussed elsewhere. Nonetheless, the fact that four adjacent tests occurred prior to and in relative proximity to the two internal panel fatigue tests documented in this report should be noted because it is possible that the cantilever tests may have affected the outcome of the internal panel results. Finally, the full-scale specimen chronological order of testing proceeded as follows:

1. Static test on West conventional steel reinforced cantilever (Ph.D by C. Klowak; to be completed)
2. Fatigue test on East conventional steel reinforced cantilever (Ph.D by C. Klowak; to be completed)
3. Fatigue test on conventional steel reinforced internal panel, Segment A

4. Static test on West conventional GFRP reinforced cantilever (Ph.D by C. Klowak; to be completed)
5. Fatigue test on East conventional GFRP reinforced cantilever(Ph.D by C. Klowak; to be completed)
6. Fatigue test on steel-free internal panel, Segment B

5.2 Segment A (Conventional Steel Reinforced)

The fatigue behavior of Segment A was investigated under cyclic loading with the use of a hydraulic actuator. Segment A was subjected to 2,000,000 cycles at a load level of 570 kN over a period of two and a half months. During the 2,000,000 cycles, Segment A sustained significant, but not critical, damage including large cracks on the top and bottom of the deck, isolated spalling of concrete falling from the soffit of the deck, and visible rupturing of internal steel reinforcement. Despite the considerable damage to the concrete and steel, the conventional steel reinforced deck managed to reach 2,000,000 cycles without any reasonable indication that punching shear failure would occur in the foreseeable future. In response to time constraints, a decision to fail the bridge deck under static loading was made. Finally, the deck achieved failure at an ultimate load of 936 kN due to static loading. The mode of failure was punching shear. A perfect punch cone formed between the top and bottom of the deck and can be seen in Figures 5.1 and 5.2.

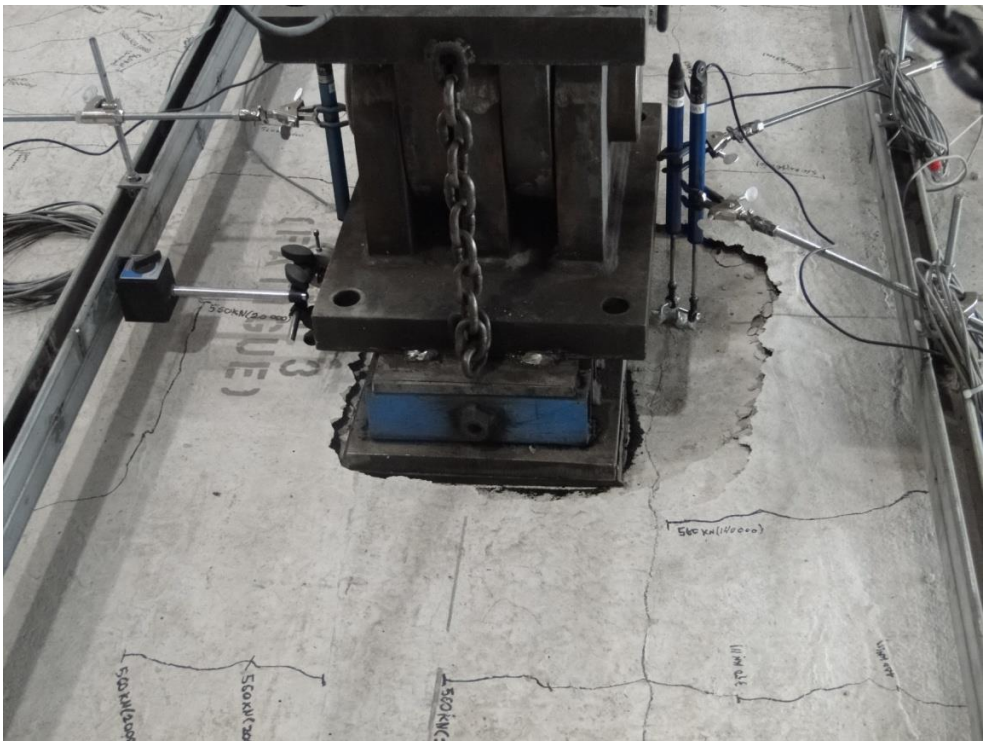

Figure 5.1 Punch cone on top of deck in Segment A

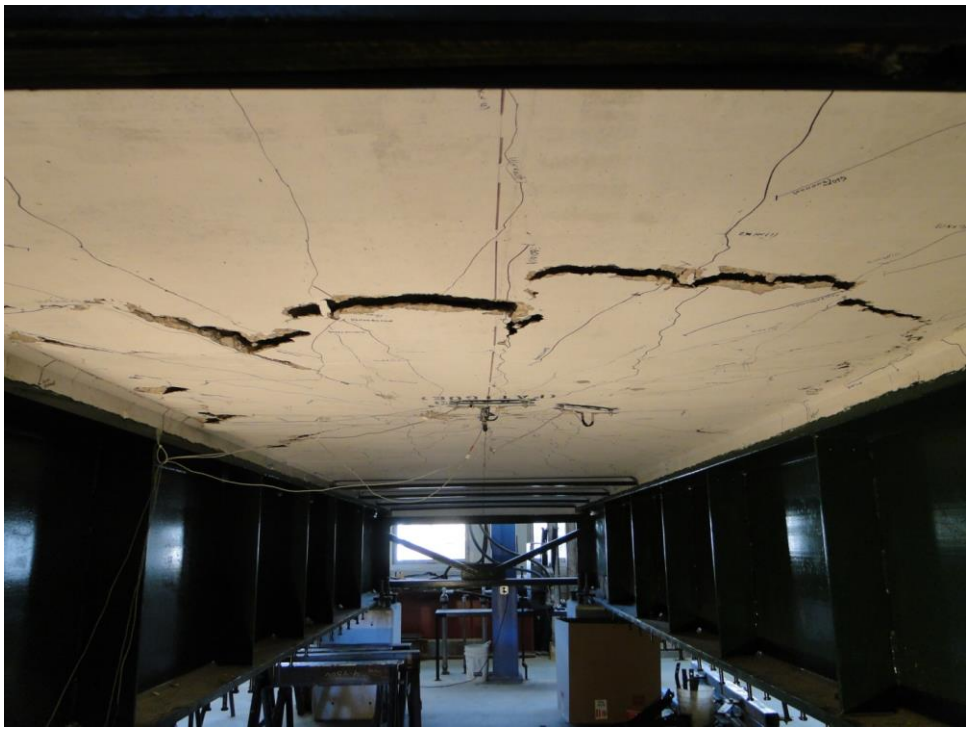

Figure 5.2 Punch cone on bottom side of deck in Segment A

To monitor the behavior of Segment A in detail, a variety of performance recording instruments were placed at locations inside and outside of the deck. LVDTs were used to measure vertical deflection with respect to the supporting steel girders. Pi gauges were attached to the top and bottom surfaces of the deck to track crack width fluctuations. The internal steel reinforcing bars were equipped with 6 mm electronic strain gauges to measure strain along the bars. Furthermore, concrete strain on the top of the deck, near the load plate, was measured with the use of a 50 mm concrete strain gauge. The results obtained from the monitoring devices listed above are presented and discussed in detail in Sections 5.2.1, 5.2.2, 5.2.3, and 5.2.4.

5.2.1 Displacement Behavior

The deflection of Segment A was recorded in two locations as previously shown in Figure 4.3. The deflection in terms of number of cycles up to 2,000,000 cycles, gathered from both recording devices LVDT No. 1-S and LVDT No. 2-S, is presented in Figure 5.3. For the first 10,000 cycles, the deflection increased sharply, followed by a swift leveling off into a near linear increasing pattern all the way up to 2,000,000 cycles. The lack of variation in the linear trend indicated that punching failure due to fatigue was unlikely to occur in the immediate future; this was one of the main contributing factors for choosing to fail the deck under static loading rather than continue fatigue loading. The vertical displacement at 2,000,000 cycles reached maximum values of 23.72 mm and 24.48 mm, recorded by LVDT No. 1-S and LVDT No. 2-S respectively.

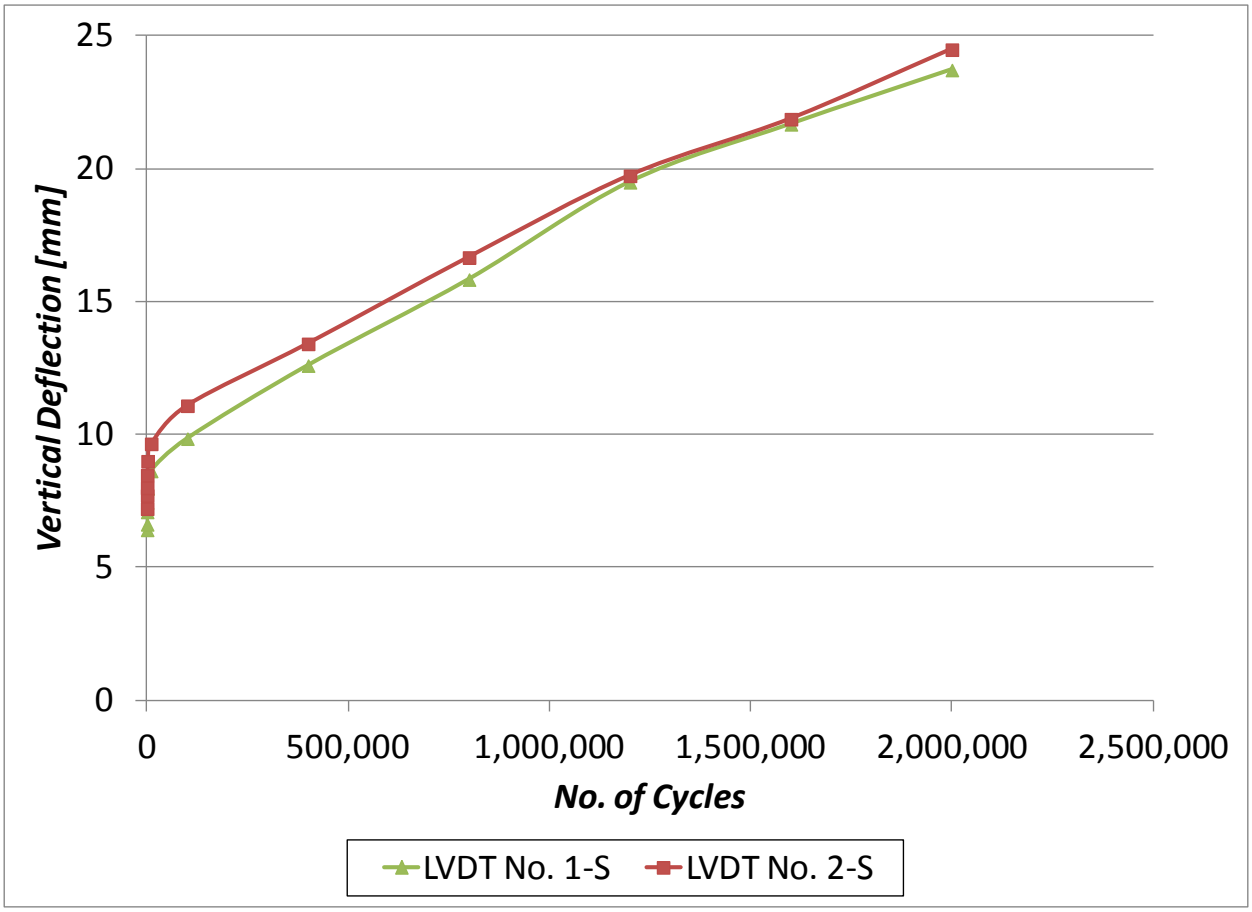

Figure 5.3 Plot of maximum vertical deflection vs. number of cycles in Segment A

Figures 5.4 and 5.5 demonstrate load versus deflection recorded by LVDT No. 1-S and LVDT No. 2-S at various cycles up to 2,000,000, as well as static failure. Data shows that the stiffness of the deck did not change significantly with increasing cycles, indicating once again that the deck would more than likely have continued resisting fatigue loading extensively beyond 2,000,000 cycles. Nonetheless, the deflection of the deck continued to grow consistently with increasing cycles. Finally, the deck reached an ultimate load of 936 kN, with coinciding maximum deflections of approximately 34.07 mm and 34.92 mm (values recorded by LVDT No. 1-S and LVDT No. 2-S respectively) recorded just prior to punching failure.

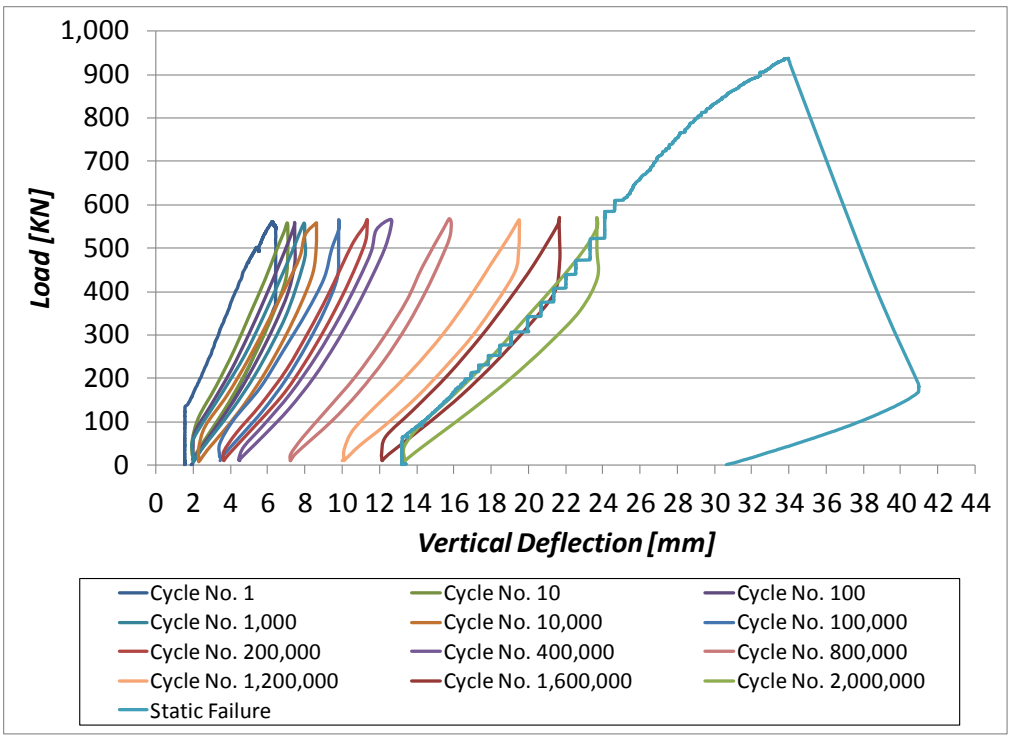

Figure 5.4 Plot of load vs vertical deflection at specified cycles in Segment A, recorded by LVDT No. 1-S

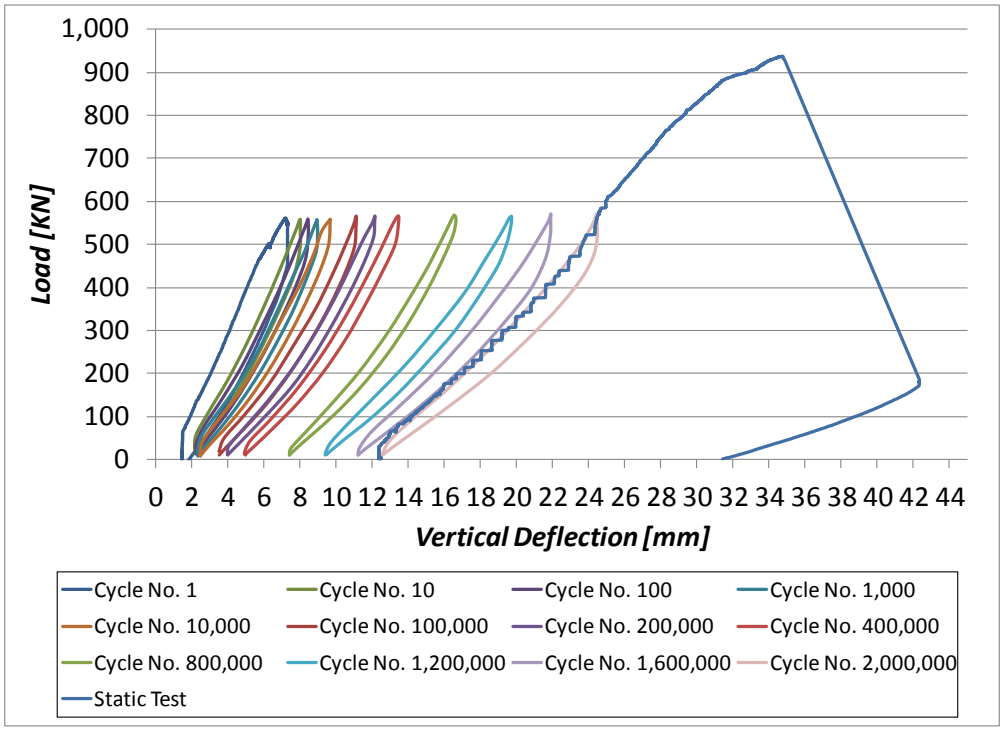

Figure 5.5 Plot of load vs vertical deflection at specified cycles in Segment A, recorded by LVDT No. 2-S

5.2.2 Crack Width Behavior

Crack width sizes were monitored in several locations with 200 mm gauge length pi gauges. It was impossible to predict exactly where cracks would develop; therefore four random, although strategic locations were chosen to observe crack width fluctuations. As previously shown in Figure 4.5, the pi gauge program for Segment A included an assortment of pi gauges used to track a series of different crack size and orientations; specifically, bottom longitudinal crack size and orientation (Pi Gauge No. 1-S), bottom transverse crack size and orientation (Pi Gauge No. 2-S), bottom radial crack size and orientation (Pi Gauge No. 3-S), and top circumferential crack size and orientation (Pi Gauge No. 4-S). Figure 5.6 covers crack width data recovered from all four pi gauges up to the 2,000,000 cycle mark.

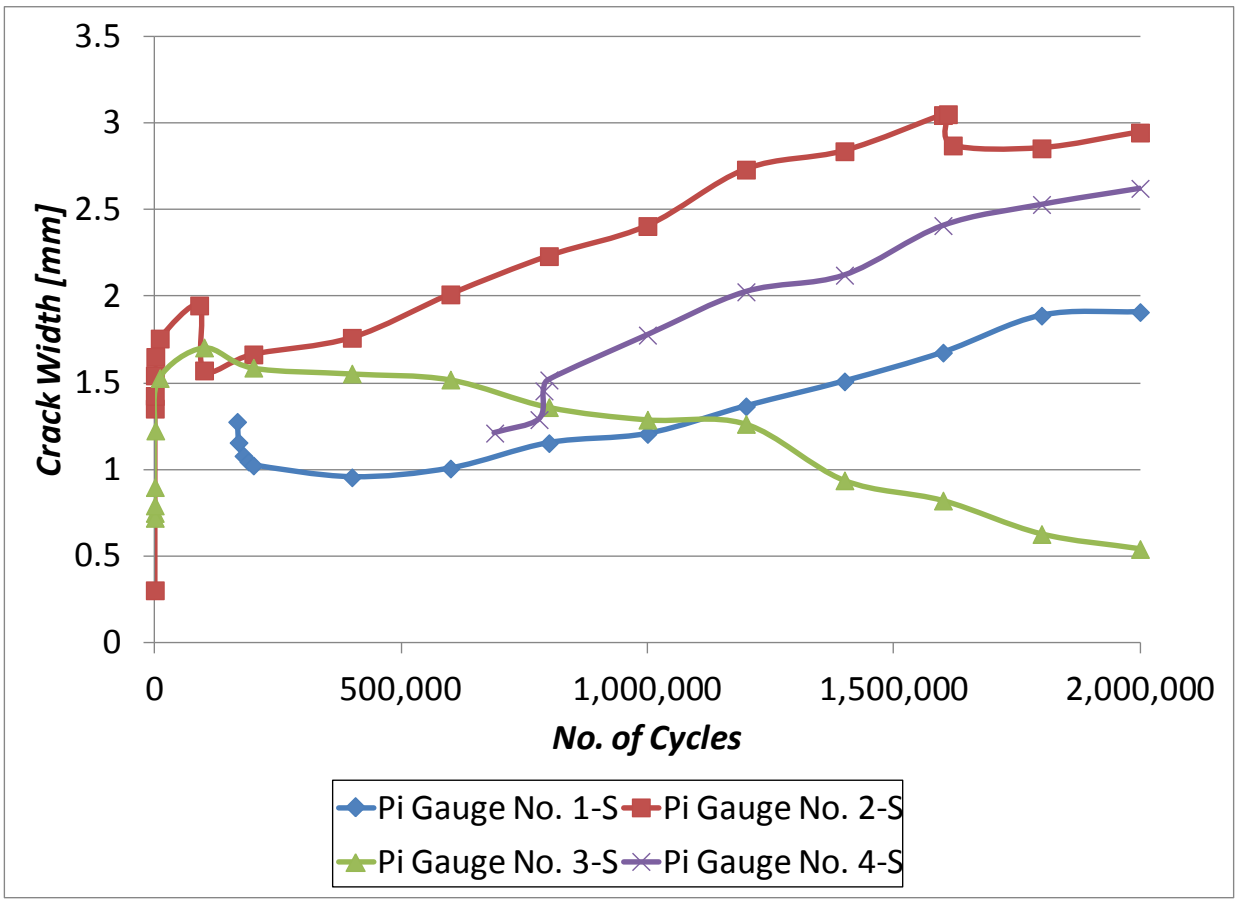

Figure 5.6 Plot of maximum crack width vs. number of cycles in Segment A

Initially, Pi Gauge No. 1-S was positioned directly below the load plate and over the main bottom longitudinal crack at the center of the deck. Unfortunately, due to shifting sections of concrete, caused by random wide spread cracking during loading, the crack that Pi Gauge No. 1-S spanned over on the underside of the deck stopped opening and closing, leading to confusing and misleading data. Therefore, at cycle no. 167,164, Pi Gauge No. 1-S was moved to a new crack location, which is the location that can be seen in previous Figure 4.5. The "at rest" (unloaded) crack width size of the new location for Pi Gauge No. 1-S was measured and entered into the residual data file prior to restarting the testing. At first, Pi Gauge No. 1-S retrieved data portraying a decrease in maximum crack width size, however only for a short period, followed by a continual increase in crack width size up until 2,000,000 cycles, where the maximum crack width size rose to approximately 1.9 mm. Pi Gauge No. 2-S monitored a large transverse crack on the underside of the deck, almost directly below the loading area. Similar to Pi Gauge No. 1-S, Pi Gauge No. 2-S was also situated in a zone subjected to continual concrete shifting; a direct result of the arbitrary formation and movement of surrounding cracks. Consequently, Pi Gauge No. 2-S showed several abrupt drops in maximum crack width, as seen in Figure 5.6; however, for the most part, Pi Gauge No. 2-S recorded a steady increase in maximum crack width, finally finishing with a maximum crack width of 2.95 mm at 2,000,000 cycles. Pi Gauge No. 3-S, spanned one of the many radial cracks that formed on the underside of the deck. Once again, as with Pi Gauges No. 1-S and 2-S, the crack that Pi Gauge No. 3-S covered was exposed to concrete shifting, and rather than showing gradual increases in crack size over the 2,000,000 cycles as with Pi Gauges No. 1-S and 2-S, Pi Gauge No 3-S decreased over almost the entire 2,000,000 cycle span. At 2,000,000 cycles, Pi Gauge No. 3-S displayed a maximum crack width of roughly 0.55 mm. Pi Gauge No. 4-S was the only pi gauge located on the top of the deck, as shown in previous Figure 4.5. Unlike cracking on the bottom of the deck, cracking on the top of the deck was much smaller and less dispersed for the first half a million cycles. The goal for Pi Gauge No. 4-S was to span over the circumferential crack that normally forms on a confined bridge deck slab. Unfortunately, the first sign of

a circumferential crack did not show up until around 680,000 cycles. At 687,308 cycles, Pi Gauge No. 4-S was placed into position directly over what was hoped to be the main circumferential crack. From the time Pi Gauge No. 4-S was fastened to the deck, an increasing pattern was noted, all the way up to 2,000,000 cycles where a maximum crack width of 2.63 mm was recorded. Figure 5.7 provides a glimpse of the crack patterns observed throughout the lifespan of Segment A.

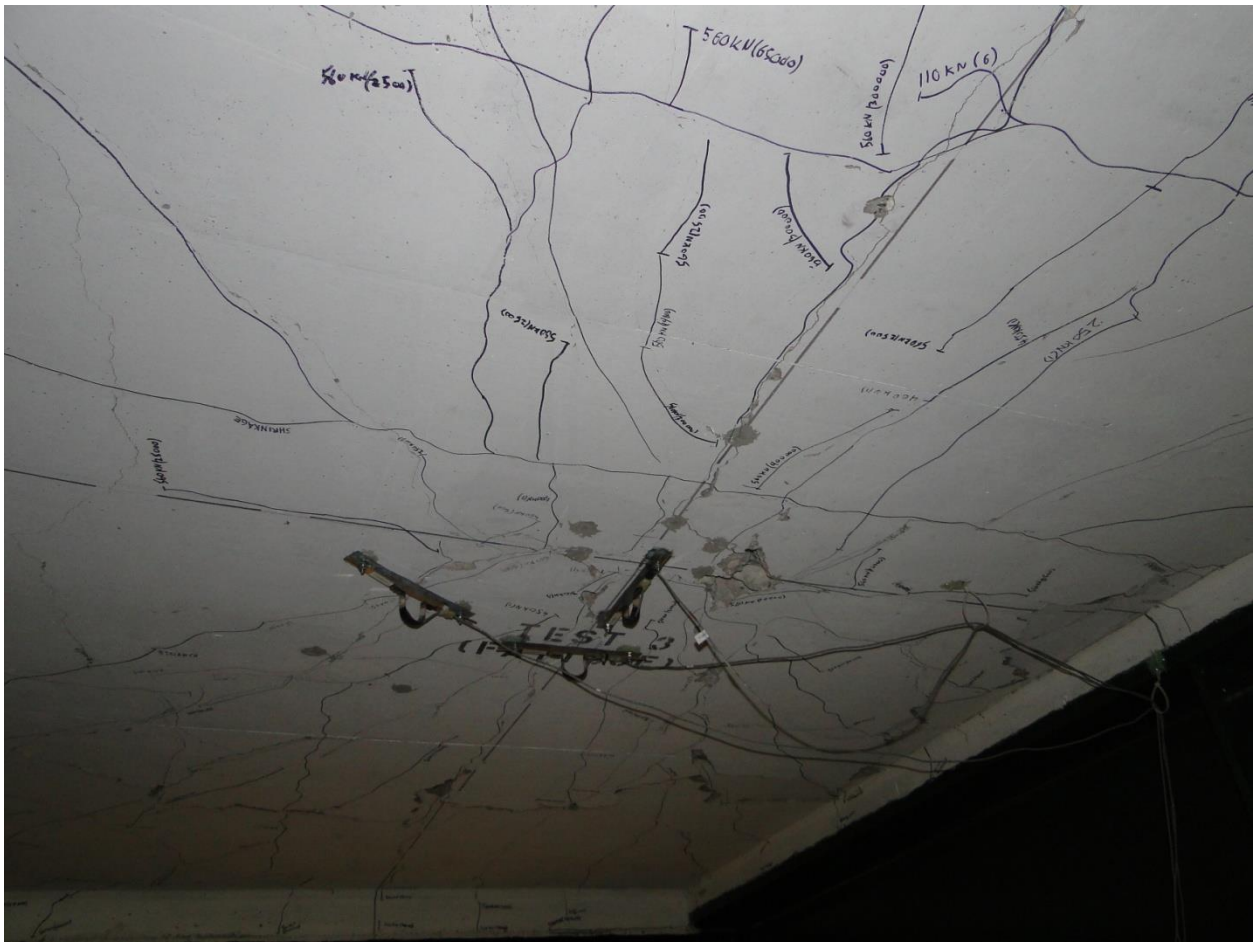

Figure 5.7 Crack patterns observed on the soffit of the deck throughout the lifespan of Segment A

5.2.3 Internal Steel Reinforcement Strain Behavior

Eleven electronic strain gauges were placed on six different steel rebar in Segment A to evaluate the strain behavior within the deck. The internal rebar equipped with electronic strain gauges included three bottom transverse steel bars, three bottom longitudinal steel bars, and one top transverse steel bar. The location of each individual electronic strain gauge attached to its corresponding rebar can be seen in previous Figures 4.7 and 4.8. The goal was to monitor the strain in the reinforcement close to the loading area as fatigue loading progressed; not one electronic strain gauge endured the entire 2,000,000 cycles. Most, if not all the electronic strain gauges stopped working because they had reached their ultimate strain recording capacity or the reinforcement which the strain gauges were attached to ruptured. It is also possible that several of the electronic strain devices failed prematurely as a result of internal damage caused by friction between the concrete and reinforcing materials which the strain gauges were attached to.

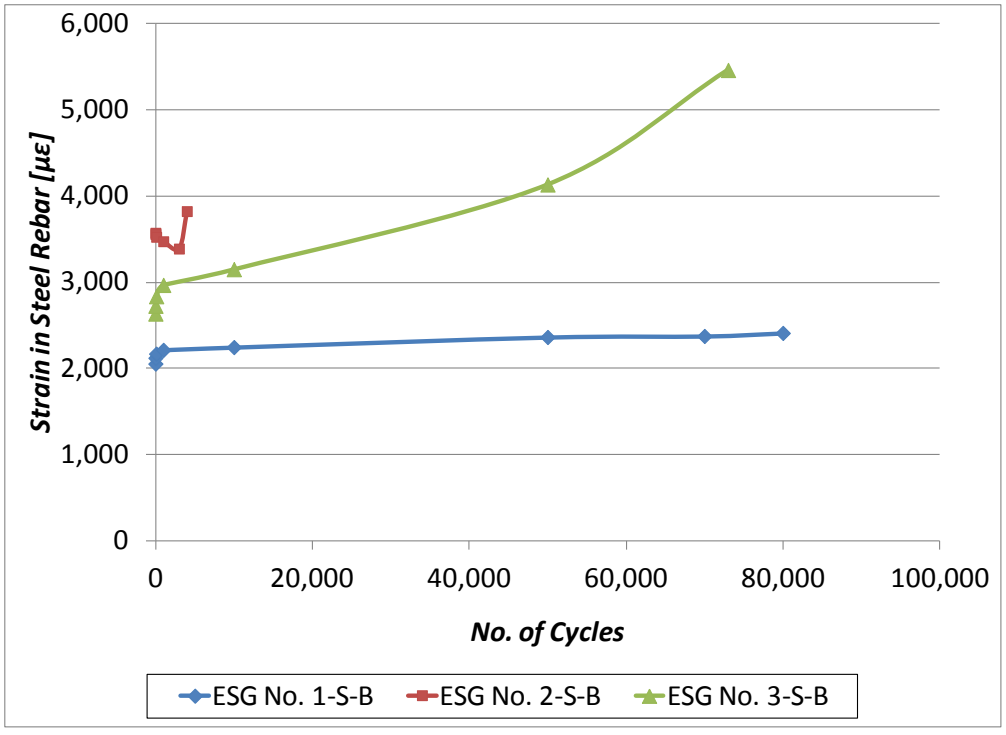

Figure 5.8 Plot of maximum strain in steel rebar vs. number of cycles in Segment A; bottom transverse steel reinforcement

The first electronic strain gauges to stop functioning were those attached to the bottom transverse steel reinforcement located directly below the loading pad; specifically ESG No. 1-S-B, ESG No. 2-S-B, and ESG No. 3-S-B. All three strain gauges signaled yielding of the steel reinforcement, upwards of 2,000 με, following the first full cycle to 570 kN. After only 4,004 cycles, and at a maximum recorded strain value of 3,823 με, ESG No. 2-S-B stopped registering sensible data, visible in Figure 5.8. It was later discovered around 186,000 cycles, when pieces of concrete started to separate from the underside of the deck, that the internal reinforcing bar that ESG No. 2-S-B was attached to had fully ruptured into two pieces, as shown in Figure 5.9. The two transverse rebar adjacent to the one that ESG No. 2-S-B was attached to, endured several 10's of thousand additional cycles prior to failure. As illustrated in Figure 5.8, ESG No. 1-S-B continued functioning up until around 80,000 cycles and registered an almost flat pattern of little to no growth in strain in the reinforcement right up to failure. On the other hand, ESG No. 3-S-B was very active up until failure at 73,017 cycles, showing a constant increase in strain in the reinforcement, reaching 5,461 με just prior to failure.

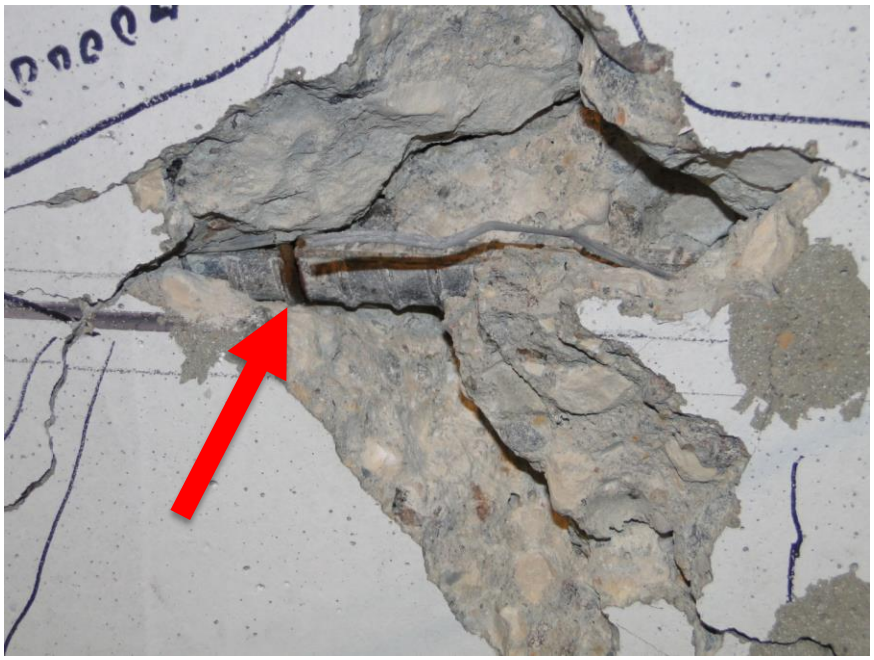

Figure 5.9 Ruptured bottom transverse steel bar in Segment A. Visible due to concrete spalling. ESG No. 2-S-B was attached to the steel bar shown in the picture

The second group of electronic strain gauges to succumb to excessive strains was those attached to the bottom longitudinal reinforcement located directly below the loading pad; specifically ESG No. 4-S-B, ESG No. 5-S-B, and ESG No. 6-S-B. The three bottom longitudinal reinforcement equipped with strain devices, unlike the bottom transverse bars, did not exceed yielding strain of 2,000 με until about 300,000 cycles, as shown in Figure 5.10. In fact, ESG No. 6-S-B did not at any point register a strain value in excess of 2,000 με; however, it stopped recording sensible data at around 161,832 cycles, thereby signaling failure. The remaining bars monitored by ESG No. 4-S-B, ESG No. 5-S-B showed small increases or small decreases in strain right up until failure. Finally, the bars failed at cycles 297,844 and 453,724 shown by the sudden respective spike in strain in ESG No. 5-S-B and ESG No. 4-S-B, with respective maximum strains of 2,375 με and 4,787 με.

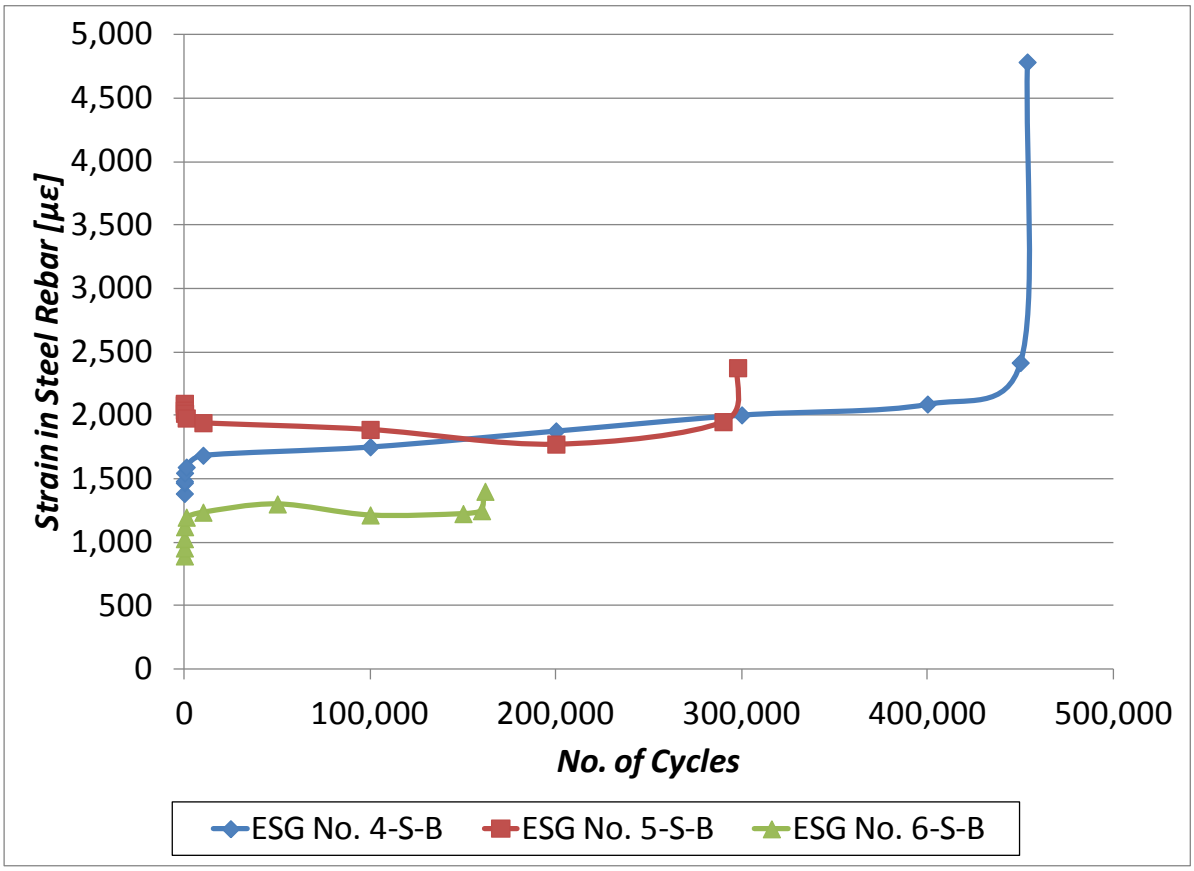

Figure 5.10 Plot of maximum strain in steel rebar vs. number of cycles in Segment A; bottom longitudinal steel reinforcement

The last group of electronic strain gauges to exceed their strain capacities was those attached to the single top transverse steel bar directly in line and parallel with the transverse centerline of the loading pad. The program included five strain gauges, namely, ESG No. 1-S-T, ESG No. 2-S-T, ESG No. 3-S-T, ESG No. 4-S-T, and ESG No. 5-S-T, attached and evenly spaced to the top transverse bar, as shown in previous Figure 4.8. The only strain gauge to show yielding in the steel bar prior to failure was ESG No. 5-S-T (located in negative moment region above girder), which surpassed 2,000 με just following 420,000 cycles; ESG No. 5-S-T then shot up to a maximum strain of 2,857 με, only to fall abruptly to 318 με around 540,000 cycles, and falling again to 79 με around 600,000 cycles, finally jumping past 2,000 με once again around 678,034 cycles, thereby finishing off a very unusual demonstration of strain behavior. It is possible that ESG No. 5-S-T failed early on closer to 420,000 cycles when it exceeded 2,857 με, and went on to produce misleading data like the odd rolling hill pattern seen in Figure 5.11 . On the opposite end of the steel bar with respect to ESG No. 5-S-T, was ESG No. 1-S-T. Because ESG No. 1-S-T was essentially in the same position on the steel bar as ESG No. 5-S-T, but on opposite ends, and the loading of the deck was centered right between the two strain recording devices, theory would suggest that the two locations should produce near identical strain patterns. However, unlike the sporadic behavior monitored by ESG No. 5-S-T, ESG No. 1-S-T showed a gradual increase in strain in the bar all the way up to 500,000 cycles with a maximum strain of 827 με, followed by a slightly less gradual decrease in strain right up to failure at approximately 1,010,000 cycles, with a maximum recorded strain of 382 με. ESG No. 3-S-T, the center most situated strain gauge along the bar, showcased a steady increase in strain behavior right up to 610,000 cycles, with a corresponding maximum strain of 872 με. From 610,000 to 615,379 cycles, ESG 3-S-T was subjected to a steep increase in strain, eventually recording a maximum strain of 1,179 με just prior to failure. ESG No. 2-S-T started off showing large, but gradual increases in strain in the bar up to 520,000 cycles, with a corresponding maximum strain of 1072 με; the strain then dropped suddenly to 700 με between 520,000 and 530,000 cycles, concluding with an increasing parabolic convex behavior, ultimately failing at 693,193

cycles and a maximum strain of 1171 με. ESG No. 4-S-T displayed a rather flat and uneventful lifespan, eventually breaking down around 1,086,015 cycles, with a maximum strain of 489 με, as well as earning the title as the last internal electronic strain gauge to fail during Segment A's testing.

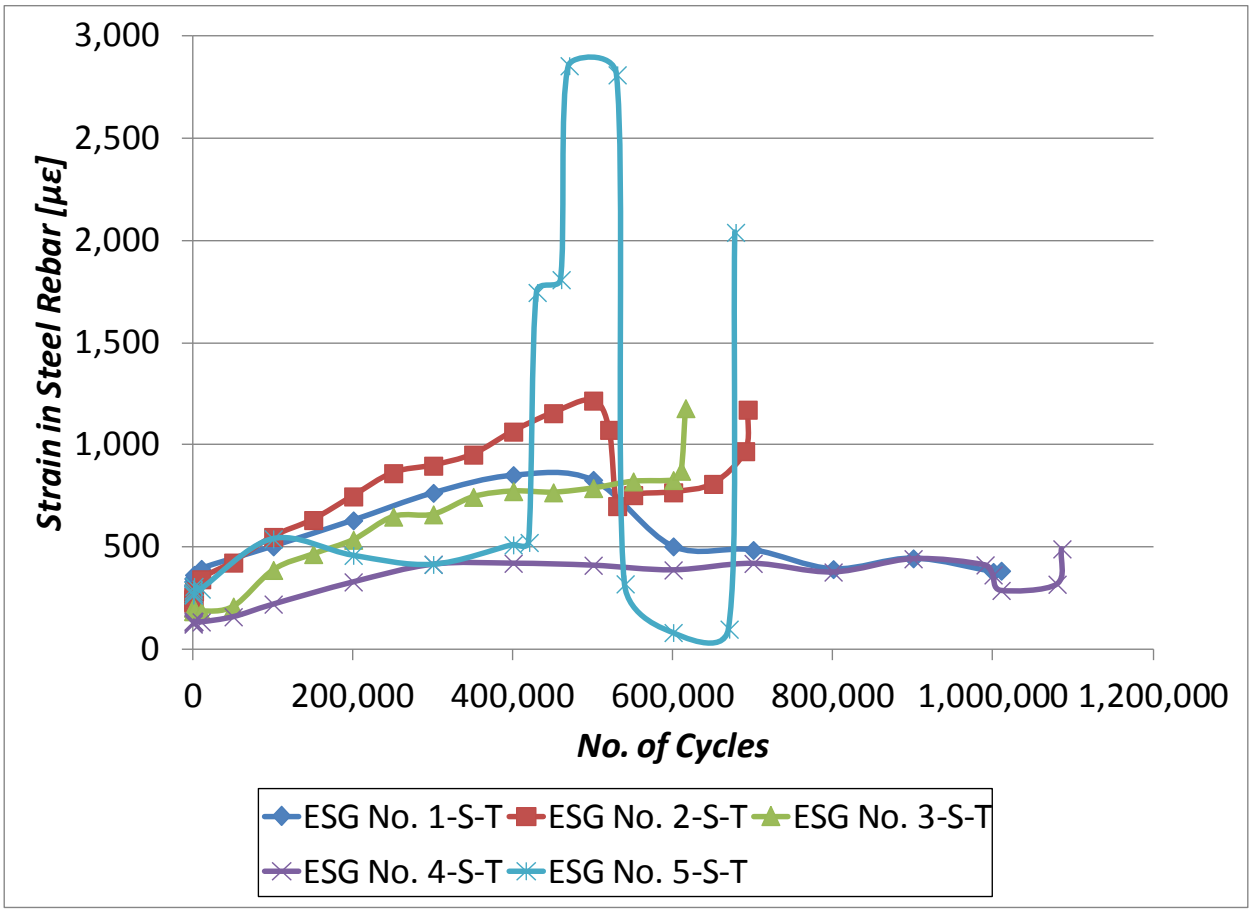

Figure 5.11 Plot of maximum strain in steel rebar vs. number of cycles in Segment A; top transverse steel reinforcement

5.2.4 Concrete Strain Behavior

In order to observe the strain behavior in the concrete during loading, a 50 mm electronic strain gauge was glued roughly 1 inch south of the edge of the load plate on the top surface of the deck, and was centered on the longitudinal center of the deck and load pad, as previously shown in Figure 4.14. The strain gauge was placed so as to record the strain in the concrete in the transverse direction.

The strain in the concrete reached a maximum of 1,254 με in compression during the first cycle to 570 kN. During the next 140,000 cycles the maximum strain in the concrete would drop significantly to approximately 765 με. The strain in the concrete would then reverse direction and jump to 860 με by 150,000 cycles. The remaining 1,850,000 cycles included a gradual and almost linear increase right up to 2,000,000 cycles where the fatigue testing was concluded. The maximum concrete strain recorded at 2,000,000 cycles was 1,513 με. The plot of max concrete strain versus no. of cycles is presented in Figure 5.12.

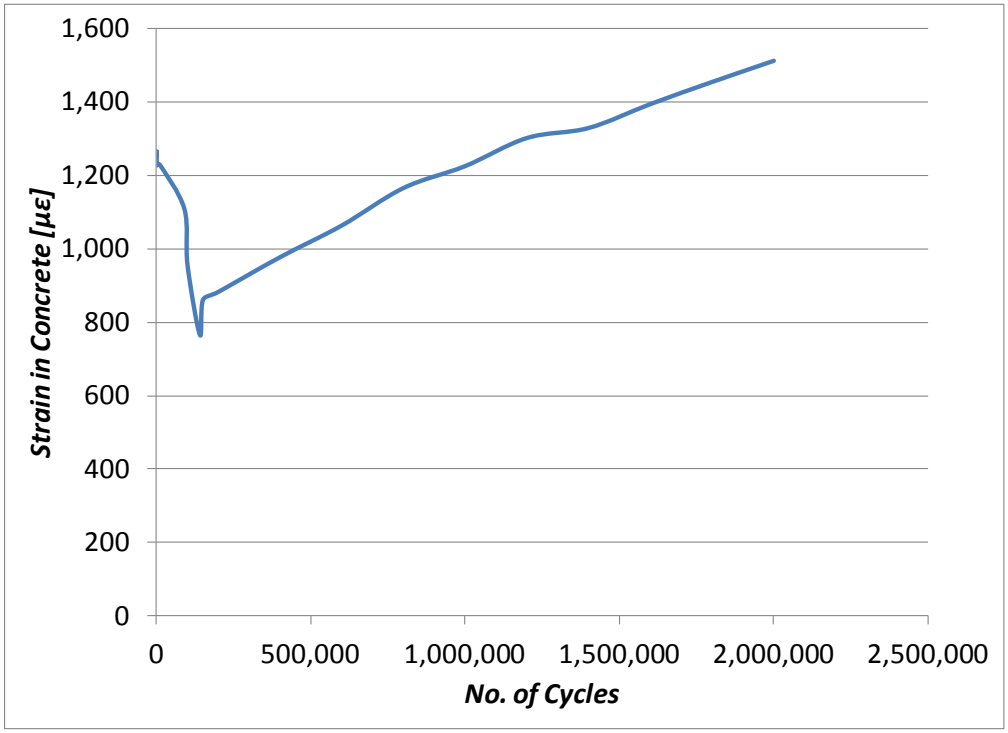

Figure 5.12 Plot of maximum strain in concrete vs. number of cycles in Segment A

Once fatigue loading was ceased, the next step for the deck was static loading to failure. The data recovered from the concrete strain gauge is presented in Figure 5.13 as load versus strain in concrete. Prior to static testing, the concrete maintained a 375 με residual strain sustained from the previous 2,000,000 cycles of loading at 570 kN. The strain in the concrete rose almost linearly with the load. In the end the strain in the concrete reached a maximum of 2,230 με at the corresponding ultimate static failure load of 936 kN. As soon as punching failure occurred, the concrete strain gauge failed immediately.

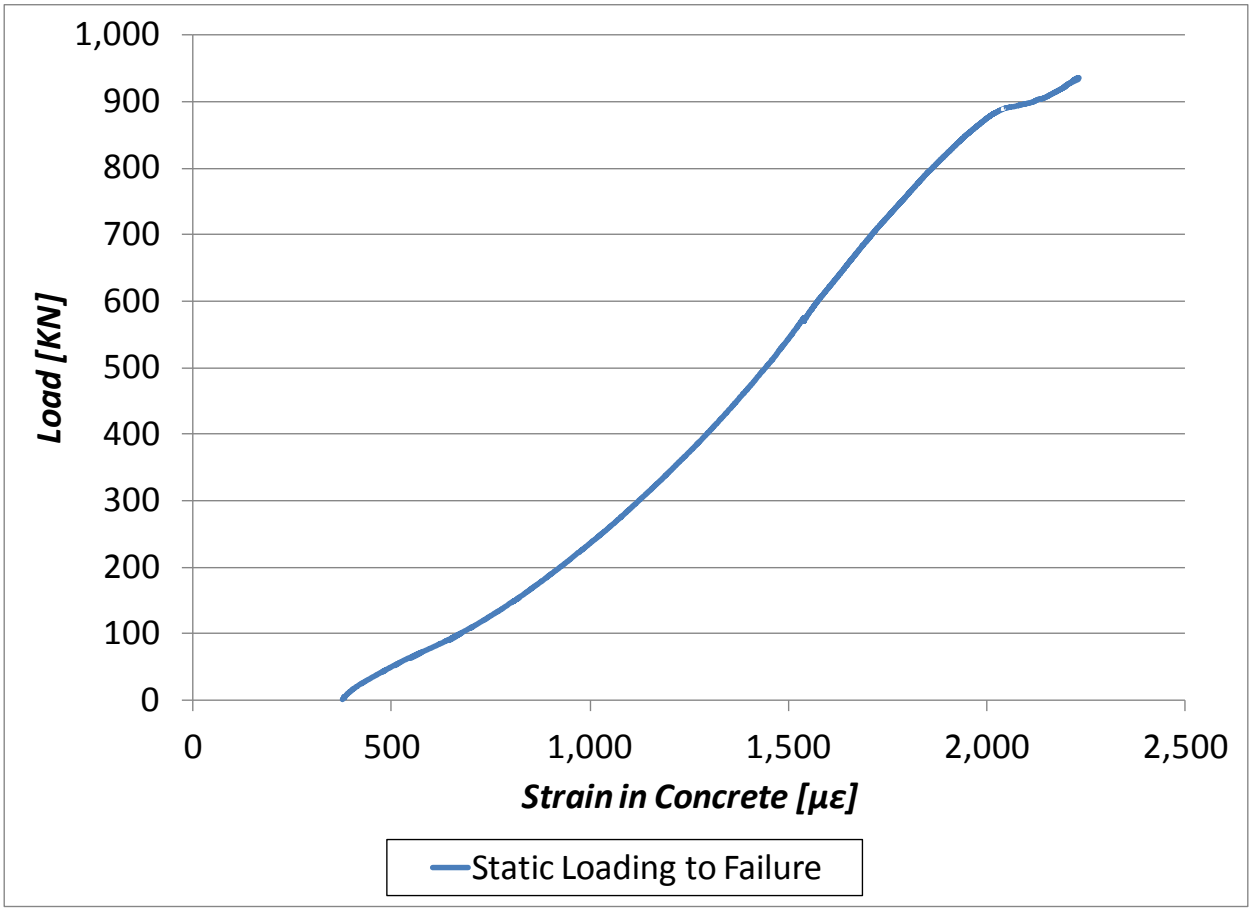

Figure 5.13 Plot of load vs. strain in concrete during static loading to failure in Segment A

5.3 Segment B (Steel-Free)

The fatigue behavior of Segment B was investigated under cyclic loading with the use of a hydraulic actuator. As with Segment A, Segment B was subjected to a constant cyclic loading of 570 kN. After only three weeks of testing and 414,223 cycles, Segment B failed prematurely. The mode of failure was punching shear. Once again, a perfect punch cone formed between the top and bottom of the deck as shown in Figures 5.14 and 5.15. The premature failure of Segment B and the presumed cause is explained in detail in Section 5.3.4.

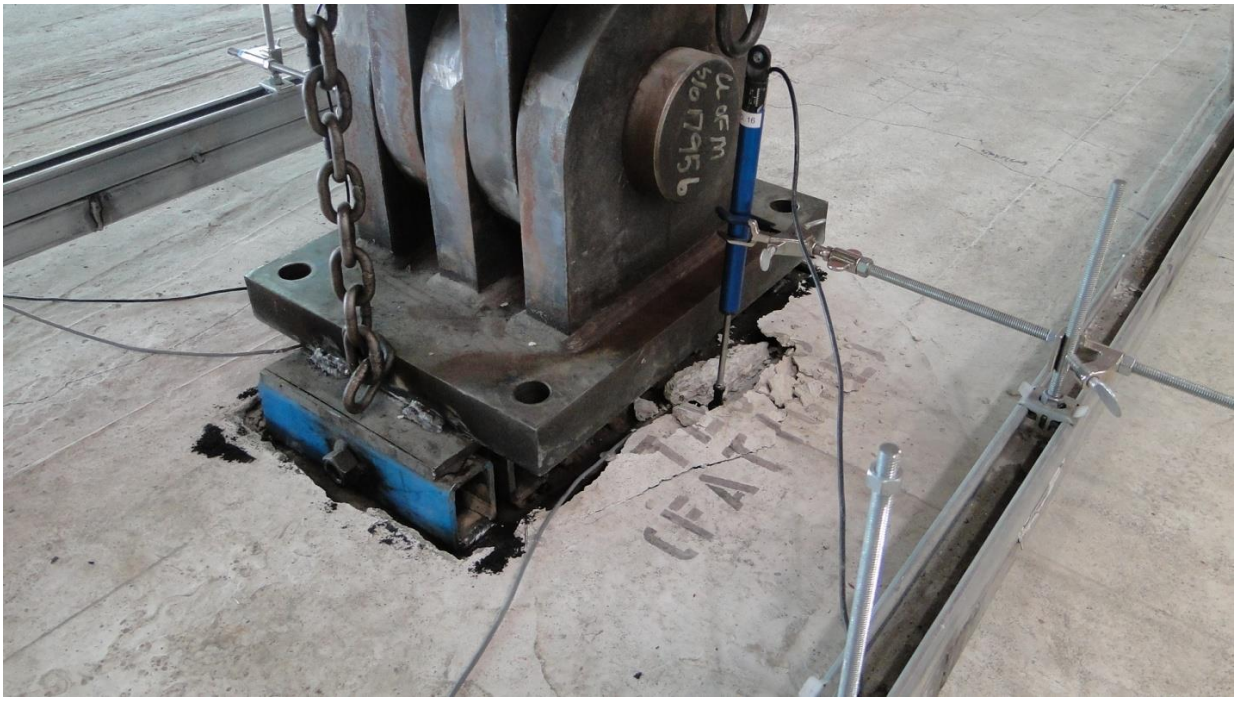

Figure 5.14 Punch cone on top side of deck in Segment B

Figure 5.15 Punch cone on bottom side of deck in Segment B

To monitor the behavior of Segment B in detail, a variety of performance recording instruments were placed at locations on the interior and exterior of the segment. LVDTs were used to measure vertical deflection with respect to the supporting steel girders. Pi gauges were attached to the top and bottom surfaces of the deck to track crack width fluctuations. The internal GFRP crack control reinforcing bars were equipped with 6 mm electronic strain gauges to measure strain along the bars. In addition, each external reinforcing steel strap was equipped with one 6 mm electronic strain gauge. Furthermore, concrete strain on the top of the deck, near the load plate, was measured with the use of a 50 mm concrete strain gauge. The results obtained from the monitoring devices listed above are presented and discussed in detail in Sections 5.3.1, 5.3.2, 5.3.3, 5.3.4, and 5.3.5 as follows.

5.3.1 Displacement Behavior

The LVDT deflection monitoring devices for Segment B, namely LVDT No. 1-SF and LVDT No. 2-SF, were installed in mirrored positions as those installed in Segment A, as previously shown in Figure 4.3. The data recovered from the two LVDT devices in Segment B, in terms of vertical deflection and number of cycles, is plotted in Figure 5.16.

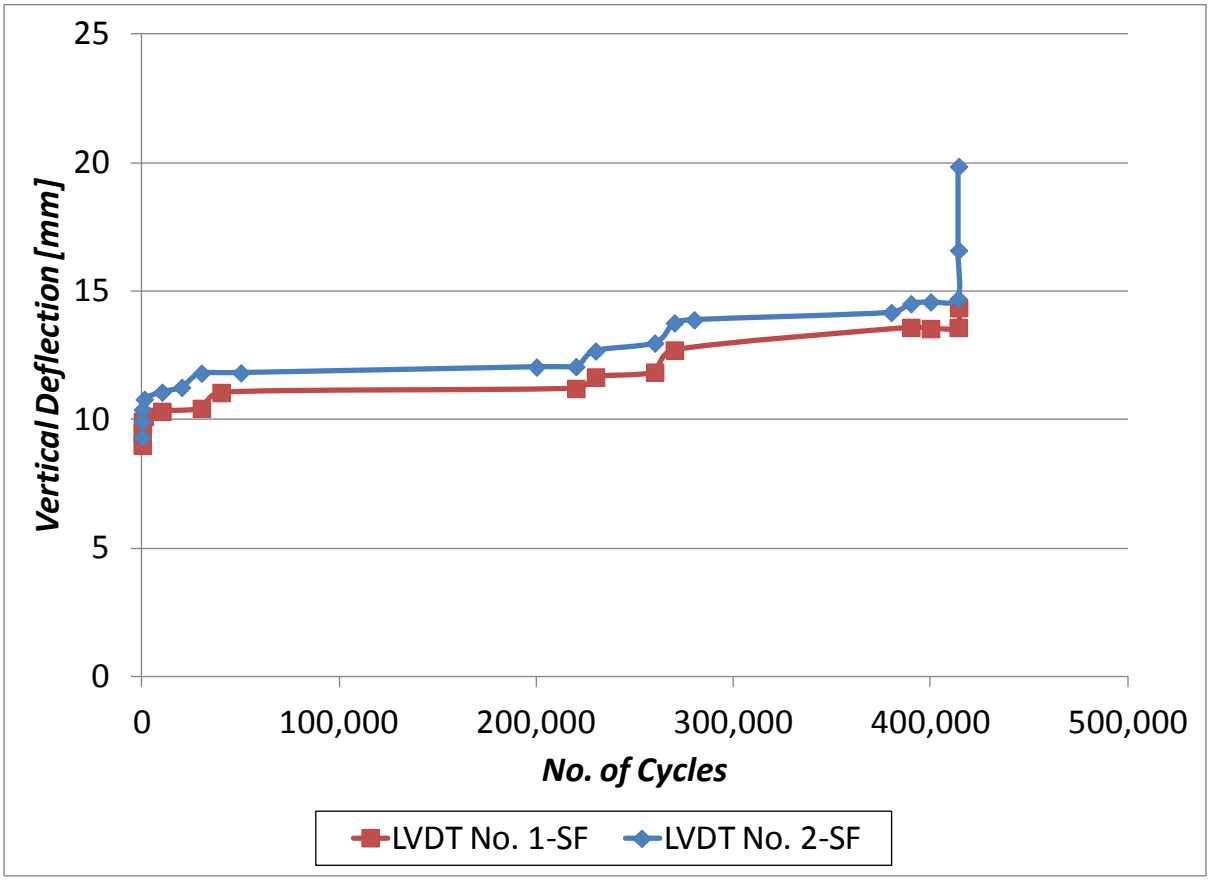

Figure 5.16 Plot of maximum vertical deflection vs. number of cycles in Segment B

As expected, both LVDT devices registered an almost identical pattern. For the first 30,000-40,000 cycles the deflection at the point of application gradually increased 2-2.5 mm, followed by a period of almost zero increase from approximately 40,000 to 220,000 cycles. At approximate cycles no. 227,000 and no. 261,101, two significant events occurred that lead to instantaneous spikes in deflection; both events were

very similar in nature. At 227,000 cycles, external reinforcing Strap No. 2 (previously shown in Figure 3.6) partially detached from within the West concrete haunch it was embedded in, and as a result its effective stiffness was reduced significantly. At almost the exact same instant both LVDT No. 1-SF and LVDT No. 2-SF recorded immediate increases in maximum deflection of 0.44 mm and 0.61 mm respectively, as shown in Figure 5.16. Around cycle no. 261,100, Strap No. 3 (also previously shown in Figure 3.6) mimicked Strap No. 2 and ruptured from within the West concrete haunch of the deck it was embedded in. Once again, sharp increases registering 0.86 mm and 0.78 mm were recorded by LVDT No. 1-SF and LVDT No. 2-SF, respectively, as a result of the reduced stiffness to the structure. From 261,100 to 414,000 cycles the deflection steadied off and increased less than 1 mm. The next 223 cycles would prove to be the final stages leading up to failure. Immediately following 414,000 cycles, the deck began to lose stiffness rapidly. The latter is demonstrated in Figure 5.16 by the near vertical increase in deflection shown by LVDT No. 1-SF and LVDT No. 2-SF. The deck finally failed in punching shear at 414,223 cycles. The overall maximum deflection recorded by LVDT No. 1-SF and LVDT No. 2-SF, just prior to punching failure, was 14.35 mm and 16.59 mm respectively.

Figures 5.17 and 5.18 demonstrate load versus deflection, for LVDT No. 1-SF and LVDT No. 2-SF, respectively, at various cycles up to punching failure at cycle no. 414,223. During the first 200,000 cycles, data shows that the stiffness of the deck did not change significantly with increasing cycles. Between 200,000 and 400,000 cycles, a reduction in stiffness was observed, clearly highlighted by the significant decrease in slope apparent from “Cycle No. 200000” to “Cycle No. 400000”. An even more profound demonstration of declining stiffness is recognized in the plotting of “Cycle No. 414,223” in both Figures 5.17 and 5.18; the slopes in both figures decrease substantially, finally concluding with the overall punching failure of the deck.

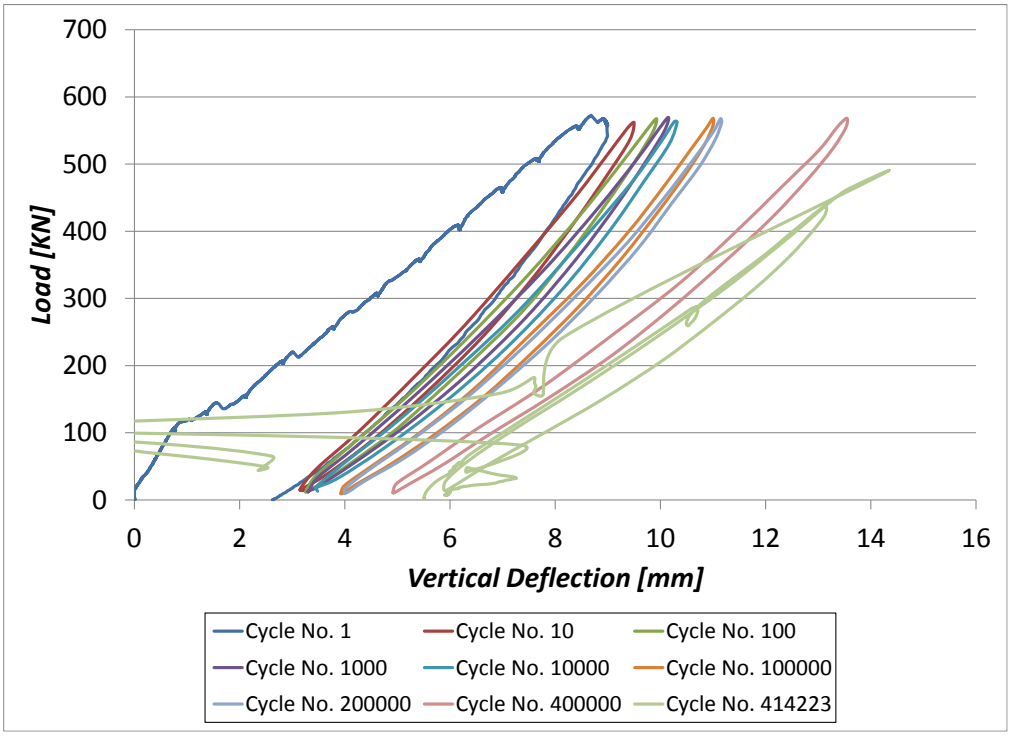

Figure 5.17 Plot of load vs. number of cycles at specified cycles in Segment B, recorded by LVDT No. 1-SF

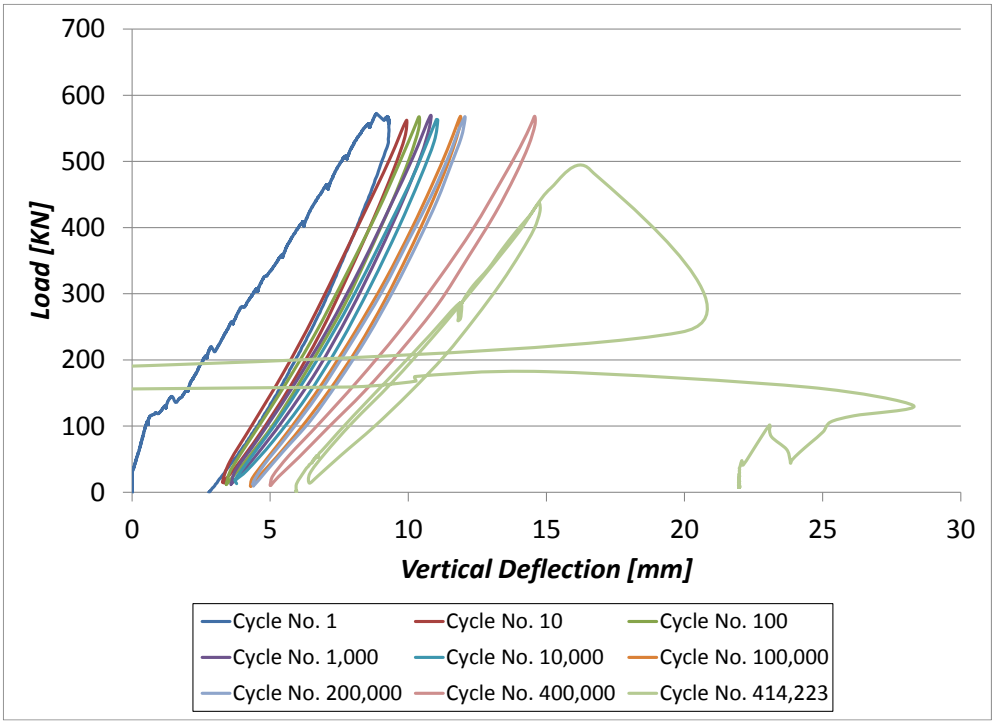

Figure 5.18 Plot of load vs. number of cycles at specified cycles in Segment B, recorded by LVDT No. 2-SF

5.3.2 Crack Width Behavior

As previously shown in Figure 4.5, the pi gauge program for Segment B included an assortment of 200 mm gauge length pi gauges used to track a series of different crack size and orientations, specifically, bottom longitudinal crack size and orientation (Pi Gauge No. 1-SF), bottom radial crack size and orientation (Pi Gauge No. 2-SF and Pi Gauge No. 3-SF), and top circumferential crack size and orientation (Pi Gauge No. 4-S).Initially, the goal was to mimic the pi gauge locations in Segment A to facilitate direct comparisons with Segment B. Unfortunately, during the first cycle of loading to 570 kN for Segment B, an issue occurred involving cracks forming beneath the glued supports of the pi gauges. The data recovered from the pi gauges during the first cycle to 570 kN was acceptable, however, there was too much of a risk that the pi gauges would detach from the bottom surface of the deck, as cycles increased, due to the formation of cracks beneath the supports. As a result, all three pi gauges attached to the bottom of the deck were relocated over three new strategic cracks that had formed during the first cycle. The “at rest” (unloaded) crack width sizes of the cracks that the pi gauges now spanned were measured and entered into the residual data file prior to restarting the testing. Figure 5.19 covers crack width data recovered from all four pi gauges up to failure, at 414,223 cycles.

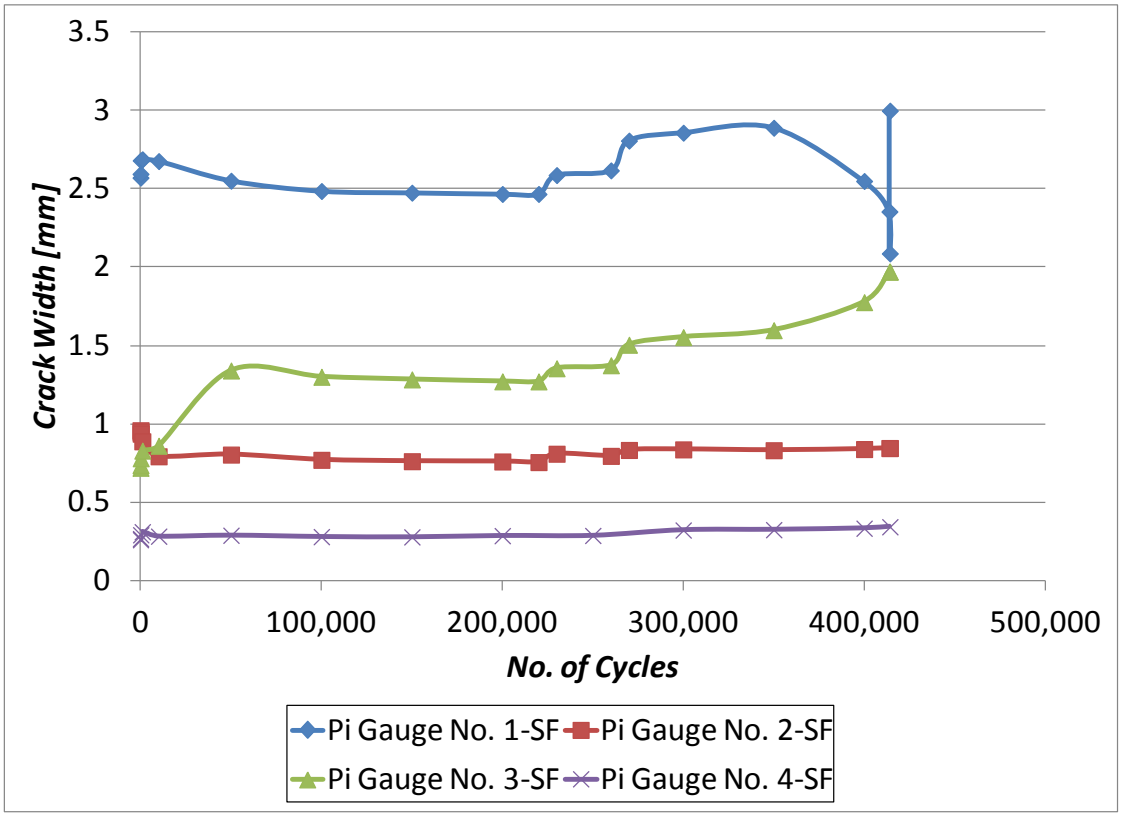

Figure 5.19 Plot of maximum crack width vs. number of cycles in Segment B

Following the second full cycle to 570 kN, Pi Gauge No. 1-SF, at its new location, recorded an enormous maximum crack width of 2.57 mm. The maximum crack width rose all the way to 2.69 mm by 1,000 cycles and then settled down gradually to about 2.46 mm by 200,000 cycles, as shown in Figure 5.19. At cycle no. 227,000 and no. 261,100, Pi Gauge No. 1-SF (location previously shown in Figure 4.5) recorded swift peaks in crack width sizes of 0.12 mm and 0.19 mm, respectively, due to the rupturing of Straps No. 2 and No. 3, respectively. By 350,000 cycles the maximum crack width given by Pi Gauge No. 1-SF was 2.89 mm. The maximum crack width would then drop steeply to around 2.08 mm by 414,222 cycles and during the last and final cycle would leap right back up and would register a maximum crack width of 3 mm just before punching shear failure occured. Pi Gauge No. 2-SF, covering one of the many radial cracks on the soffit of the deck, showed very little variation in crack width size over the entire 414,223 cycles. The only

events that caused Pi Gauge No. 2-SF to show any noticeable fluctuations in crack width size were the detachments of Strap No. 2 and Strap No. 3 from the West concrete haunch at cycle no. 227,000 and no. 261,100, respectively; even so, the jump in maximum crack width size was 0.05 mm or smaller in both instances. The final maximum crack width size recorded by Pi Gauge No. 2-SF at cycle no. 414,223 was 0.84 mm. Pi Gauge No. 3-SF demonstrated a rapid increase in crack width size for the first 50,000 cycles, registering a maximum crack width of 1.33 mm, as shown in Figure 5.19. Between 50,000 and 220,000 cycles there is little variation in crack width size shown by Pi Gauge No. 3-SF. Once again, visible increases in crack width size to the order of 0.08 mm and 0.13 mm, were observed by Pi Gauge No. 3-SF at cycle no. 227,000 and cycle no. 261,100, respectively, due to the rupturing of Straps No. 2 and No. 3, respectively. In the end, the radial crack monitored by Pi Gauge No. 3-SF finished off at a maximum crack width of 2 mm at cycle no. 414,223 just prior to punching failure. Pi Gauge No. 4-SF, the only pi gauge located on the top of the deck, recorded almost little to no variation in crack width size over the 414,223 cycle lifespan of Segment B. The maximum crack width size recorded by Pi Gauge No. 4-SF was 0.34 mm. Figure 5.20 provides a glimpse of the crack patterns observed throughout the lifespan of Segment B. Figure 5.21 shows the cracking that formed around the load pad imprint moments before punching shear failure occurred.

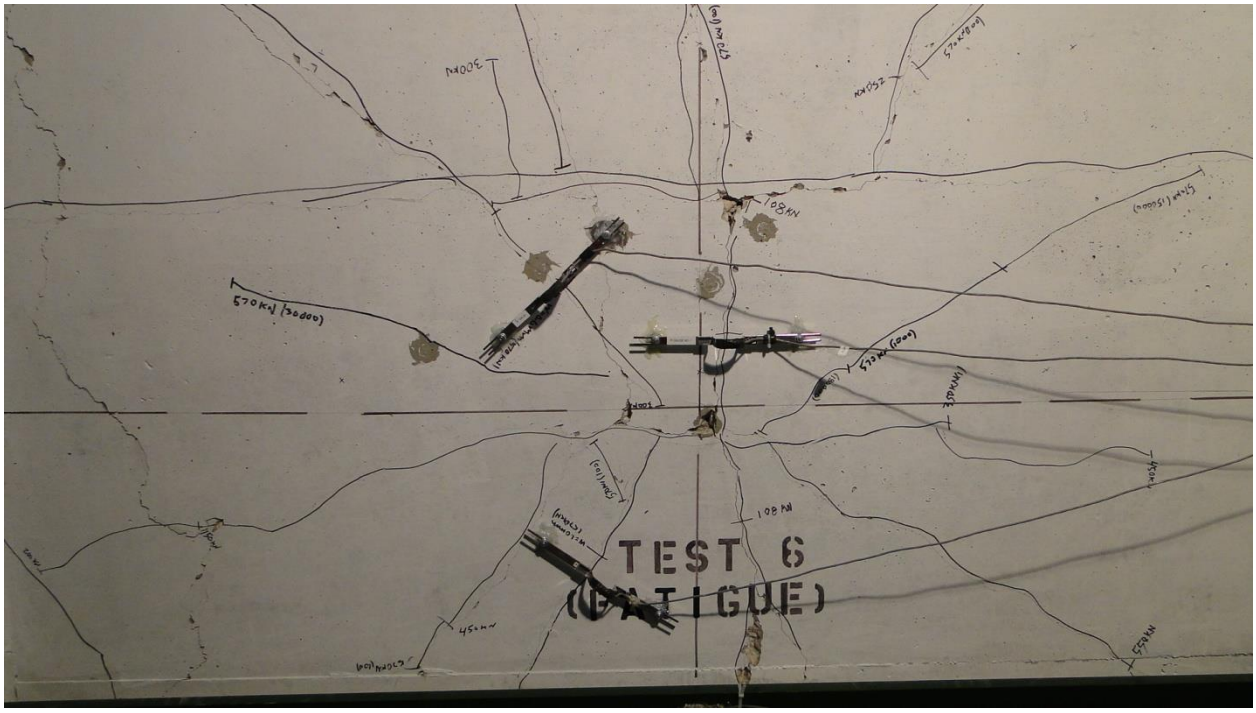

Figure 5.20 Crack patterns in Segment B

Figure 5.21 Crack pattern that formed around load pad imprint moments before punching shear failure of Segment B

5.3.3 Internal GFRP Crack Control Reinforcement Strain Behavior

Ten electronic strain gauges were placed on five different internal crack control GFRP bars to evaluate the strain behavior on the inside of the concrete deck. The internal bars equipped with electronic strain gauges included three bottom transverse GFRP bars, three bottom longitudinal GFRP bars, and one top transverse GFRP bar. The location of each individual electronic strain gauge attached to its corresponding GFRP bar can be seen in previous Figures 4.7 and 4.8. The goal was to monitor the strain in the reinforcement closest to the loading area as fatigue loading progressed; not one electronic strain gauge endured the entire 414,223 cycles leading to failure. Most, if not all the electronic strain gauges stopped working because they had reached their ultimate strain recording capacity. It is also possible that several of the electronic strain devices failed prematurely as a result of internal damage caused by friction between the concrete and reinforcing materials which the strain gauges were attached to.

The electronic strain gauges, namely ESG No. 1-SF-B, ESG No. 2-SF-B, and ESG No. 3-SF-B, each attached to one of three bottom transverse GFRP bars being monitored, all reached their ultimate strain recording capacity very early on during the testing. For instance, ESG No. 2-SF-B succumbed to failure after only one full cycle to 570 kN and registered a maximum strain of 5,271 με in the GFRP bar, as displayed in Figure 5.22. The GFRP bar monitored by ESG No. 3-SF-B jumped from a maximum strain of 2,361 με to 2,993 με from cycle 1 to 10, respectively; eventually tapering off to a slightly lower maximum strain of 2,864 με by cycle no. 556, at which the strain gauge stopped functioning. ESG No. 1-SF-B lasted 5,949 cycles before failing, initially recording a maximum strain of 4,149 με during the first cycle, and finally receding to 3,447 με upon failure.

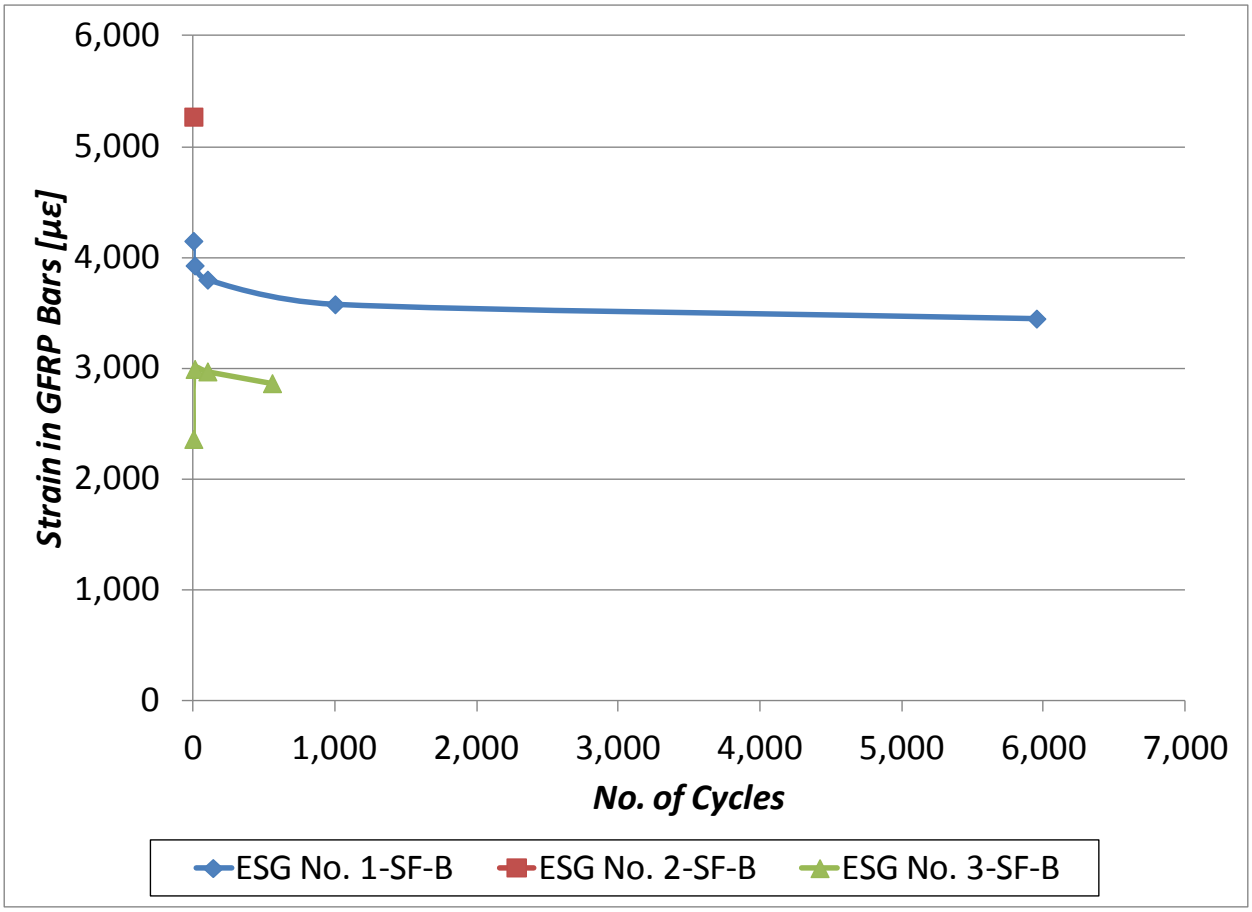

Figure 5.22 Plot of maximum strain in GFRP bars vs. number of cycles in Segment B; bottom transverse GFRP reinforcement

The bottom longitudinal GFRP bars monitored by ESG No. 4-SF-B and ESG No. 5-SF-B (locations previously shown in Figure 4.7 lasted slightly longer than the bottom transverse GFRP bars. ESG No. 4-SF-B recorded a maximum strain of 987 με during the first cycle to 570 kN, and failed at a maximum strain of 1,383 με, 68,073 cycles later, as shown in Figure 5.23. ESG No. 5-SF-B witnessed a little more strain action during its lifespan as opposed to ESG No. 4-SF-B. From cycle no. 1 to 1,000, ESG No. 5-SF-B jumped from a maximum strain of 1,574 με to a maximum strain of 1,977 με, respectively; and once again jumped from a maximum strain of 1,990 με to a maximum strain of 3,979 με from cycle no. 10,000 to 17,124, respectively, where it eventually stopped functioning.

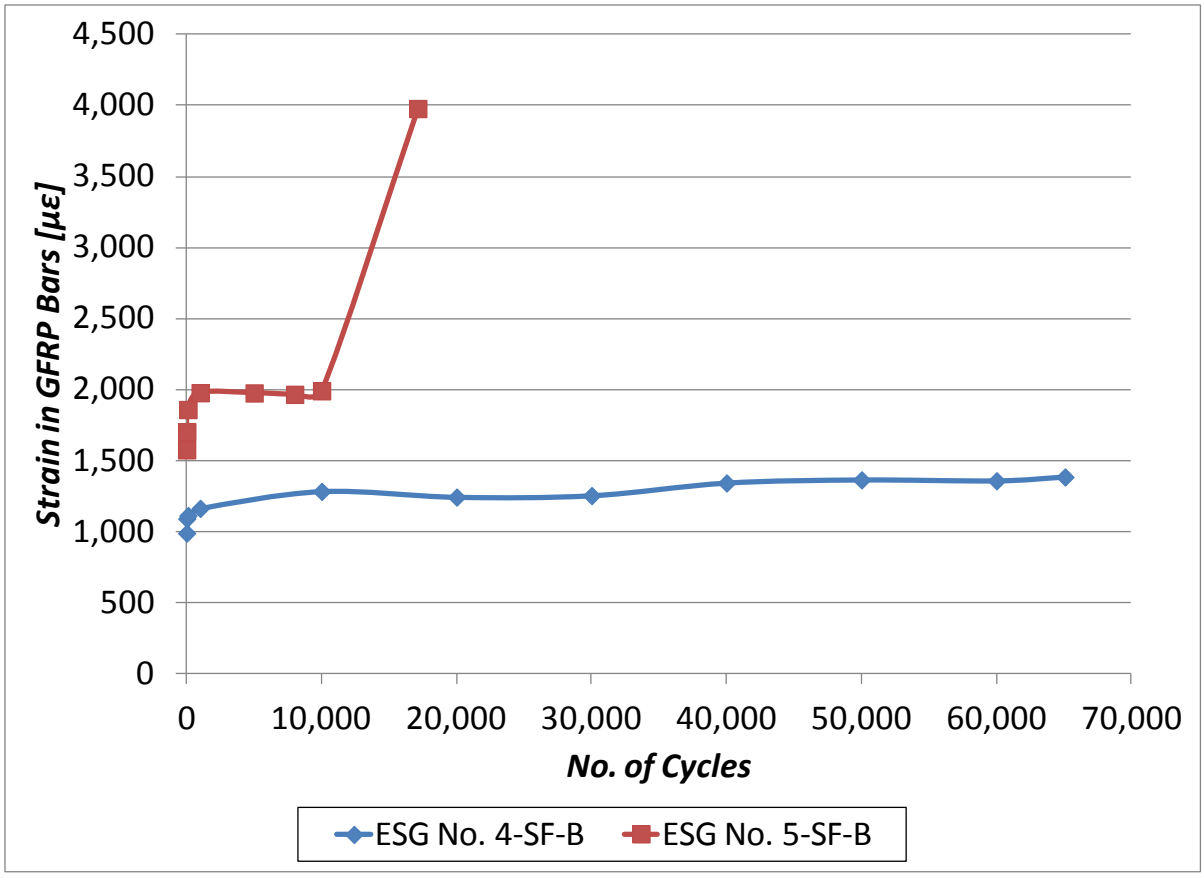

Figure 5.23 Plot of maximum strain in GFRP bars vs. number of cycles in Segment B; bottom longitudinal GFRP reinforcement

The final group of electronic strain gauges, namely ESG No. 1-SF-T, ESG No. 2-SF-T, ESG No. 3-SF-T, ESG No. 4-SF-T, and ESG No. 5-SF-T, were all attached and evenly spaced onto the top transverse steel bar directly in line and parallel with the transverse centerline of the loading pad, as previously shown in Figure 4.8. As expected, ESG No. 3-S-T, being located closest to the loading pad, registered the highest maximum strains along the top transverse GFRP bar. For the first 227,000 cycles, ESG No. 3-S-T recorded strain values at or hovering just below 2,000 με. When Strap No. 2 ruptured at around 227,000 cycles, ESG No. 3-S-T jumped from a maximum strain of 1,848 με to a maximum strain of 1,987 με, as shown in Figure 5.24. When Strap No. 3 ruptured at around 261,100 cycles, ESG No. 3-S-T jumped from a maximum strain of 2,054 με to a maximum strain of 2,208 με. ESG No. 3-S-T stopped registering sensible data around 342,258

cycles and recorded a corresponding maximum final strain of 2,350 με. As theory would suggest, ESG No. 2-SF-T and ESG No. 4-SF-T demonstrated very similar patterns and magnitudes of strain throughout their lifespan due to the symmetrical proximity along the GFRP bar in which they were situated. ESG No. 2-SF-T never exceeded a maximum strain of 170 με and stopped recording sensible data around 320,000 cycles, with a corresponding maximum final strain of 34 με. For the first 280,000 cycles, ESG No. 4-SF-T indicated maximum strain values in the GFRP bar hovering around 286 με. Not until between 300,000 and 320,000 cycles was there a noticeable spike in strain recorded by ESG No. 4-SF-T; in this case the maximum strain in the GFRP bar went from 261 με to 688 με from 300,000 to 320,000 cycles, respectively. In the end ESG No. 4-SF-T failed at 321,068 cycles at a slightly lower maximum strain of 553 με. As expected, ESG No. 1-SF-T and ESG No. 5-SF-T demonstrated very similar patterns and magnitudes of strain throughout their lifespan due to the symmetrical proximity along the GFRP bar in which they were also situated. The maximum strain recorded by ESG No. 1-SF-T rose immediately to 511 με by 10,000 cycles and continued to increase gradually to 835 με by 170,000 cycles, as shown in Figure 5.24. Between 170,000 and 180,000 cycles, ESG No. 1-SF-T registered a second spike in maximum strain, this time reaching upwards of 1,089 με. A third gradual increase in strain would occur between 180,000 and 286,235 cycles, where ESG No. 1-SF-T would record a maximum final strain of 1,343 με. ESG No. 5-SF-T also showed a sudden increase early on in the testing, reaching a maximum strain of 807 με by 10,000 cycles. The strain recorded by ESG No. 5-SF-T would fluctuate very little until its failure at 280,994 cycles, in which a maximum final strain of 1,200 με was recorded.

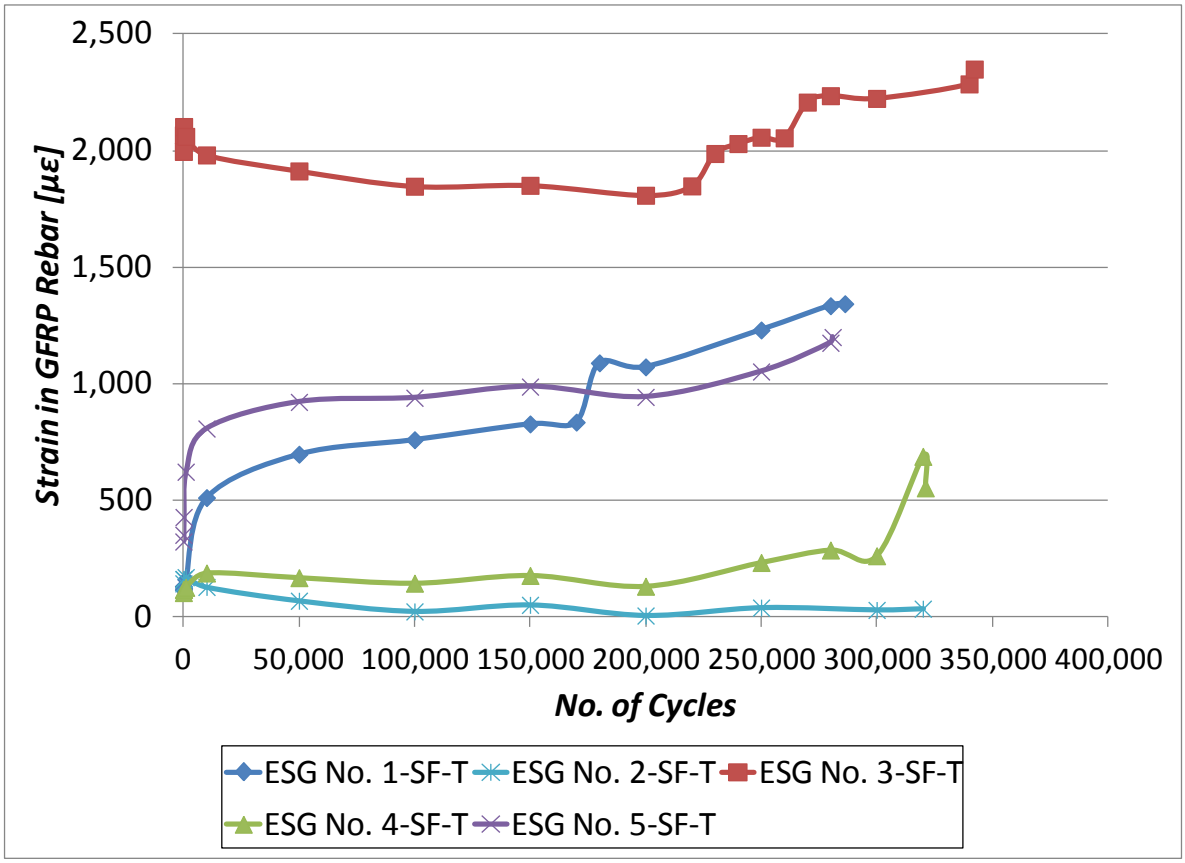

Figure 5.24 Plot of maximum strain in GFRP vs. number of cycles in Segment B; top transverse GFRP reinforcement

5.3.4 External Steel Strap Reinforcement Strain Behavior and Theoretical Explanation of Premature Failure

Segment B being the steel-free section of the deck received its primary reinforcement from external transverse steel straps located below the concrete deck. The straps were embedded into the haunches of the deck; they were 50 x 25 x 2,800 mm in size and spaced at 1,200 mm o/c. Welded to each end of the straps were three 22 mm diameter by 200 mm long nelson studs spaced 100 mm apart. There were four external steel straps in total called for in the design of Segment B. Each strap was equipped with one 6 mm electronic strain gauge attached at the center of the strap, as shown in previous Figure 4.10. The goal was to monitor the strain in the steel straps as fatigue loading progressed. All four electronic strain gauges,

namely Strap ESG No. 1, Strap ESG No. 2, Strap ESG No. 3, and Strap ESG No. 4, endured the entire 414,223 cycles leading up to punching shear failure of the deck.

For the first 220,000 cycles or so, the electronic strain gauges attached to the four straps showed almost identical patterns, as shown in Figure 5.25; however, they all varied in magnitude based on the closeness of the straps to the area of loading. For the first 200,000 cycles, the maximum strain in the straps hovered around 1,048 με, 941 με, 757 με and 415 με according to Strap ESG No. 2, Strap ESG No. 3, Strap ESG No. 1, and Strap ESG No. 4, respectively. Following 220,000 cycles, two very significant events occurred that ultimately affected the long-term performance and endurance of Segment B. First, at approximately 227,000 cycles, Strap No. 2 started to loosen from within the West side haunch it was embedded in. Soon after, at approximately 261,100 cycles, Strap No. 3 also started to loosen from within the West side haunch it was embedded in. The dislodging of the straps lead to an instant decrease in maximum strain in the straps from 1048 με to 603 με according to Strap ESG No. 2 and from 956 με to 512 με according to Strap ESG No. 3, as shown in Figure 5.25. It is evident that when Strap ESG No. 2 and Strap ESG No. 3 recorded sequential losses in maximum strain due to the dislodging of their respective straps, the remaining two strain gauges, notably Strap ESG No. 1 and Strap ESG No. 4, recorded definitive increases in maximum strain. It is obvious that the stresses once predominantly carried by Straps No. 2 and No. 3 had now been redistributed into Straps No. 1 and No. 4 to counteract the loss in restraint stiffness in the bridge deck as a whole. For the remaining cycles leading to failure, none of the electronic strain gauges recorded significant changes in strain in the straps. Just prior to failure, the strain in each strap was 864 με, 606 με, 505 με, and 533 με according to Strap ESG No. 1, Strap ESG No. 2, Strap ESG No. 3, and Strap ESG No. 4, respectively.

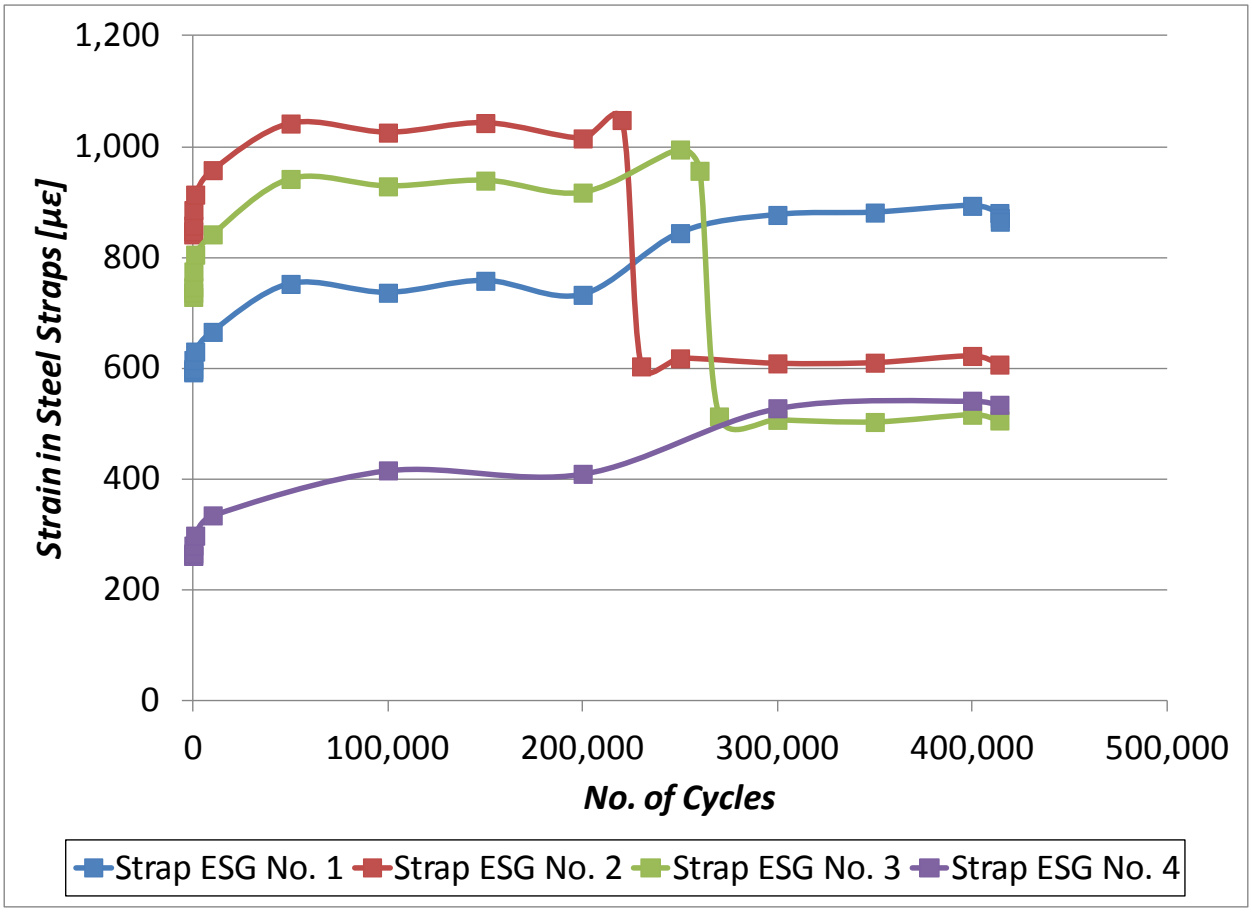

Figure 5.25 Plot of maximum strain in steel straps vs. number of cycles in Segment B

It was determined that the loss of strain in Straps No. 2 and No. 3 was due to a complete rupturing of steel along the cross-section of both straps. The rupturing of the steel straps occurred within the haunches and was only visible once the concrete had been removed from the girders, studs and straps following the removal of the bridge deck from the structures laboratory. Because the actual point of rupture for both steel straps was located directly adjacent to the inner most steel stud, as shown in Figure 5.26, Figure 5.27, Figure 5.28, and Figure 5.29, it is believed that the weld used to connect the steel stud to each steel strap weakened the steel at that point in the cross-section and as a result contributed to the sudden premature rupturing of the straps.

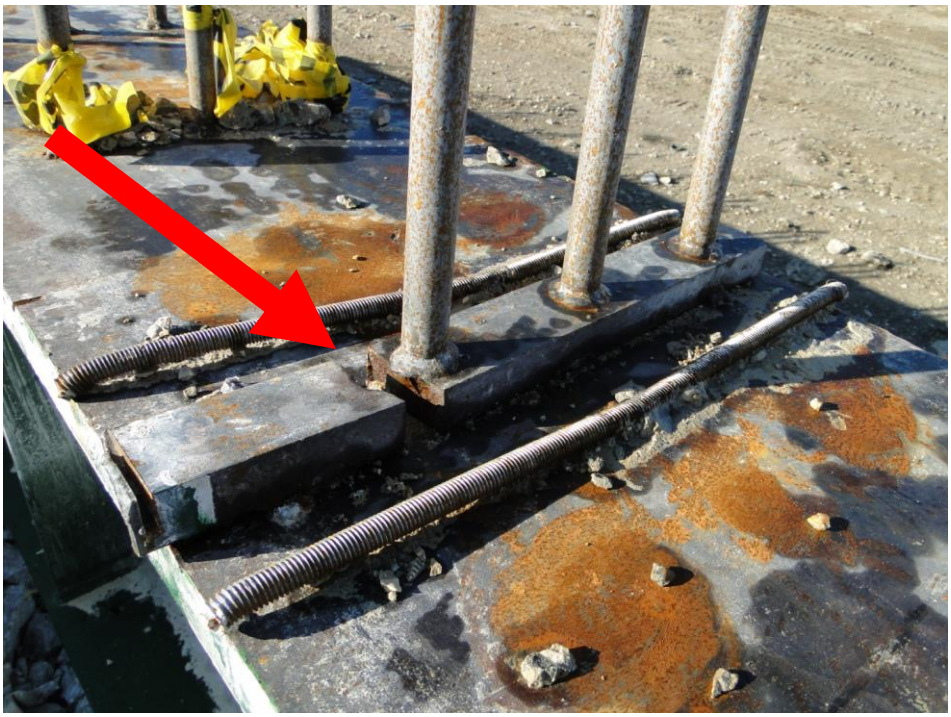

Figure 5.26 Rupture point in Strap No. 2

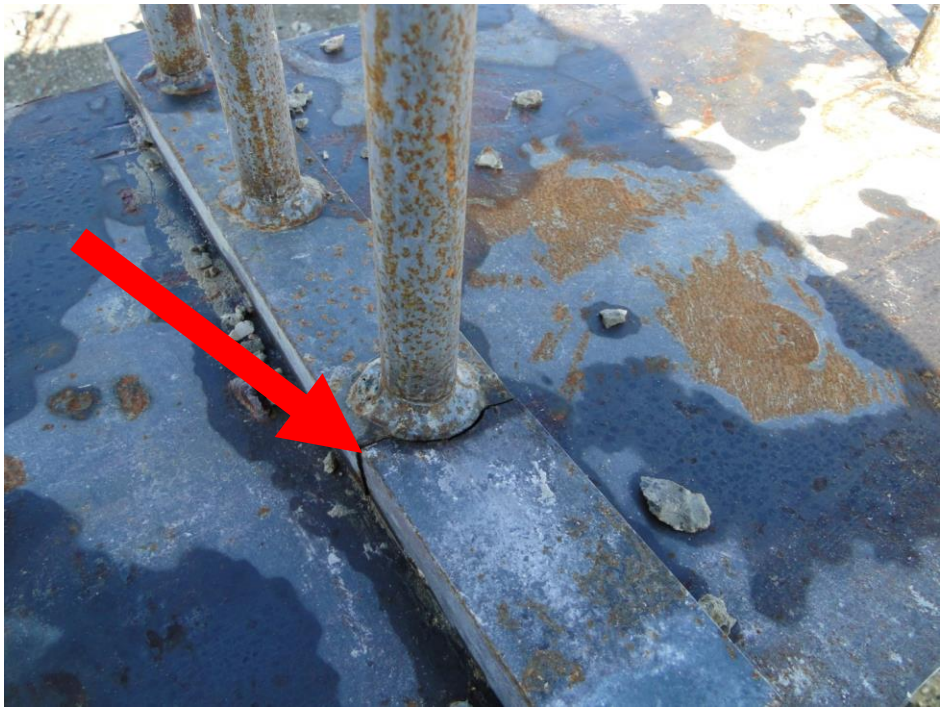

Figure 5.27 Rupture point in Strap No. 3

Figure 5.28 Rupture interface in Strap No. 3

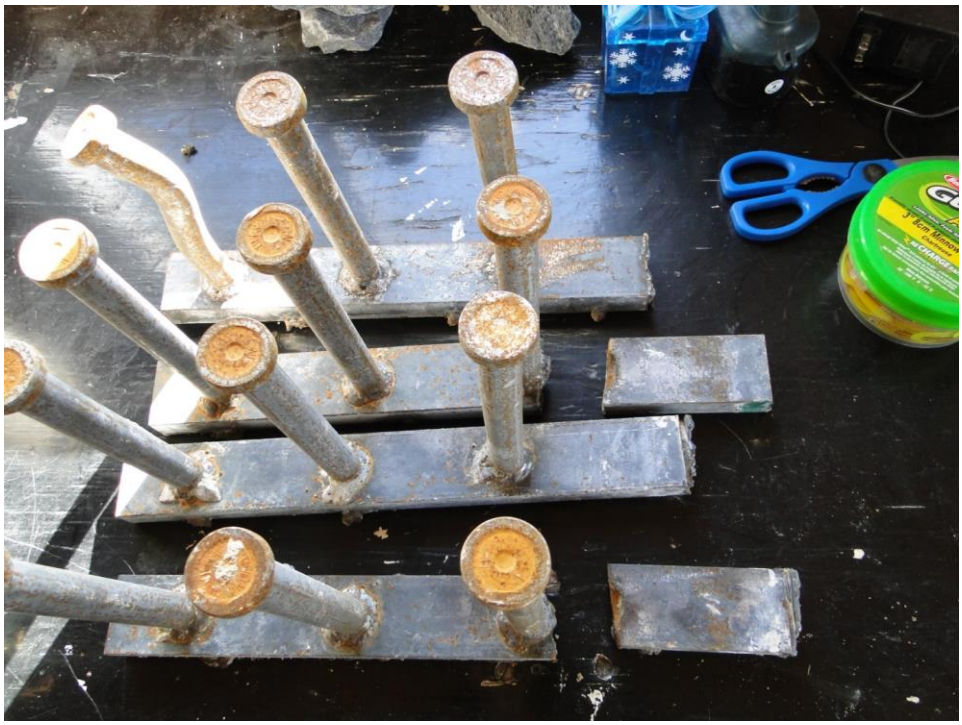

Figure 5.29 Strap No's 1, 2, 3, and 4 after removal from concrete haunches

5.3.5 Concrete Strain Behavior

In order to compare the concrete strain in Segment B with that of Segment A, a 50 mm electronic strain gauge was glued in the exact mirrored position as was the case in Segment A, as shown in Figure 4.14. Similar to Segment A, the concrete strain in Segment B spiked rather high initially to a maximum of 2,657 με in compression, and reversed course immediately as shown in Figure 5.30. By 6,000 cycles, the strain in the concrete was down to a maximum of 2,255 με in compression. Between 6,000 and 8,000 cycles, the strain in the concrete dropped significantly and at 8,011 cycles the concrete strain gauge either exceeded its ultimate strain capacity or stopped functioning. 1,592 με in compression was the final maximum strain recorded.

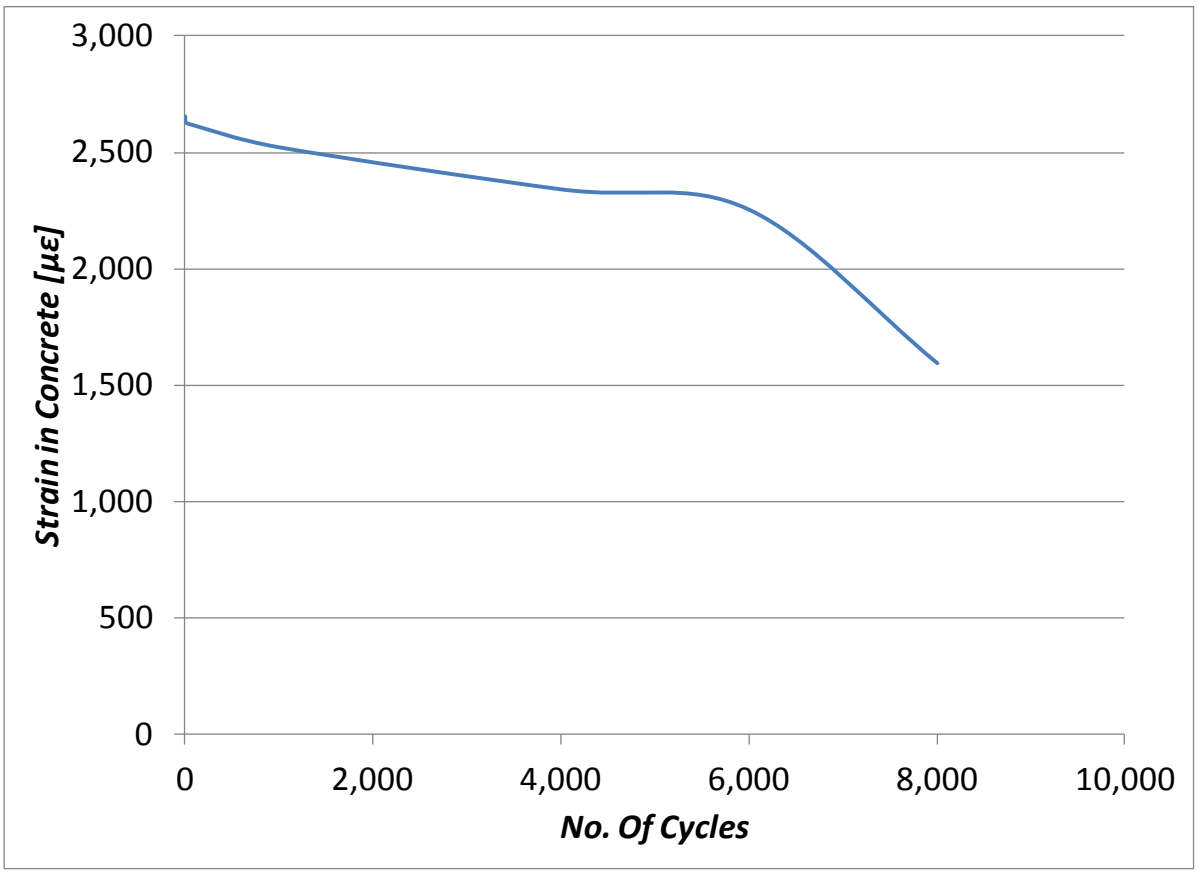

Figure 5.30 Plot of maximum strain in concrete vs. number of cycles in Segment B

Chapter 6

Discussion

6.1 General

This chapter discusses the overall comparison between Segments A and B. The first topic discussed is the cause of failure of Segments A and B, and the overall significance. The second topic discussed is the direct comparison between Segments A and B in terms of fatigue performance. Finally, the test results from Segments A and B are assessed under limit states design requirements.

6.2 Cause of Failure of Segments A and B, and the Overall Significance

In order to judge the test results from both Segments A and B fairly, it is important to look at the cause of failure for both segments and evaluate the overall significance that those causes had on the capacity, endurance, structural integrity, and response of the two differently designed structures. In the end, both Segments A and B (steel reinforced and steel-free, respectively) failed in punching shear failure. The major differences were: the form of loading under which each section failed, and the overall root cause of failure.

6.2.1 Segment A

Segment A, the steel reinforced section of the deck, endured 2,000,000 cycles at a cyclic load of 570 kN before it was decided that the deck was not likely to fail in the near future. The alternative was to apply a constant increasing static load until failure was reached. Finally, at a static load of 926 kN, Segment A failed in the form of punching shear failure. The cause of failure is believed to be that the deck simply reached its ultimate punching shear capacity.

Segment A exceeded far beyond any of the original predictions for number of cycles, and in the end out performed Segment B, the steel-free section of the deck. There is no question that the conventional steel reinforced slab-on-girder bridge deck system is a safe design, and the test results gathered from this experiment only reinforce that notion. To reach 2,000,000 cycles at a cyclic load of 570 kN (roughly five times the maximum unfactored allowable wheel load anywhere in Canada) and then go on to resist 936 kN before failing is quite remarkable.

6.2.2 Segment B

Segment B, the steel-free section of the deck, failed in fatigue after only 414,223 cycles at a cyclic load of 570 kN. The mode of failure was punching shear failure. The cause of failure is believed to be directly related with the substantial loss of two major reinforcing components sustained during the fatigue loading. At respective cycle no's 227,000 and 261,100, exterior steel reinforcing Straps No's 2 and 3 ruptured along their cross-sections right at the welded edge of the inner steel studs which were welded to the straps in the West haunch, as shown in previous Figure 5.26, Figure 5.27, Figure 5.28, and Figure 5.29. The rupturing of the steel straps caused a major loss in restraint stiffness in the deck, which in turn weakened the arching action in the deck. It is this loss of restraint stiffness that is believed to have led to the premature punching shear failure of Segment B. It is possible that if the straps had not ruptured, and instead continued to serve their purpose, Segment B may not have succumb to punching shear failure so early on in its lifespan as compared to the 2,000,000 cycles that Segment A endured under the exact same loading conditions.

The loss of restraint stiffness mentioned above is clearly visible in previous Figure 5.25, where Strap ESG No. 2 and Strap ESG No. 3 show losses in maximum strain in the straps of more than half. It should be noted that over the course of loading, all four straps sustained permanent strain; in effect, Straps No. 2 and No. 3 after rupturing still showed strain but this strain was residual. Therefore, although previous

Figure 5.25 shows that Strap ESG No. 2 and Strap ESG No. 3 continued to record strain after the straps had ruptured, the actual restraint stiffness provided by the straps was more or less negligible. Without the restraint stiffness provided by the two central straps, only the outer two straps (Strap No. 1 and Strap No. 4) were available to provide restraint stiffness to the concrete deck and steel girders. In the end, the final result was punching shear failure, which confirmed that arching action was still present in the structure even after the two central straps fully ruptured. Despite failing prematurely, it is quite remarkable that the deck continued to resist the 570 kN fatigue loading an additional 153,123 cycles even after its second steel strap ruptured. In the real world, this would have allowed for plenty of time for proper maintenance and/or rehabilitation to take place before the deck actually failed. This not only emphasized the safe aspects and reliability of the steel-free slab-on-girder bridge deck, but also highlighted that it encompassed the fundamental durability required by a structure to continue to resist loading and avoid complete failure, even after damage was sustained and localized failure occurred.

6.3 Direct Fatigue Performance Comparison of Segments A and B

For the purpose of comparison, the test results extracted from Segment A was plotted against the test results extracted from Segment B and was compared accordingly. The test results included test parameters such as number of cycles, deflection, crack width, reinforcement strain, and concrete strain. The main objective was to compare the results and differences between the two separate tests in terms of, but not limited to, capacity, endurance, structural integrity, and overall response.

6.3.1 Loading and Endurance Comparison of Segments A and B

Segment B, the steel-free section of the deck, failed in fatigue after only 414,223 cycles at a cyclic load of 570 kN; whereas, Segment A, the steel reinforced section of the deck, endured 2,000,000 cycles at an identical cyclic load of 570 kN, but did not fail. As a result, a decision was made based on time restrictions

to statically load Segment A until failure, which eventually took place at an ultimate static load of 936 kN. The mode of failure for both segments was punching shear failure.

6.3.2 Deflection Comparison of Segments A and B

Maximum deflection versus no. of cycles for Segments A and B is plotted in Figures 6.1a and 6.1b. LVDT No's 1-S and 2-S were mounted to Segment A, and LVDT No's 1-SF and 2-SF were mounted to Segment B. Previous Figure 4.3 shows a plan view layout of the above mentioned LVDT's. The maximum deflection in Segment A, recorded by LVDT No's 1-S and 2-S, increased at a steady pace all the way up to 2,000,000 cycles. LVDT No's 1-SF and 2-SF in Segment B showed greater initial maximum deflections compared to those recorded in Segment A during the first 30,000 cycles. Following those initial increases, the maximum deflections recorded in Segment B flattened out and registered little to no increase, eventually evening out with the maximum deflections recorded in Segment A as shown in Figure 6.1a and 6.1b at around 220,000 cycles. At approximately 227,000 cycles, Strap No. 2 in Segment B ruptured, causing a loss in restraint stiffness and a subsequent increase in maximum deflections, ending a near zero slope pattern of maximum deflection over the previous 200,000 cycles. At around 261,100 cycles, Strap No. 3 ruptured and the maximum deflections in Segment B rose sharply for a second time. For the remaining 153,000 cycles or so, the maximum deflections in Segment B stabled off once again, this time right up until failure. If not for the rupturing of Strap No's 2 and 3, there is valid evidence, such as that shown in Figures 6.1a and 6.1b, that Segment B could theoretically have continued its near zero maximum deflection slope pattern and it is plausible that the maximum deflections in Segment B could have remained below those recorded in Segment A, and Segment B could very well have endured the 2,000,000 cycles that Segment A was able to achieve.

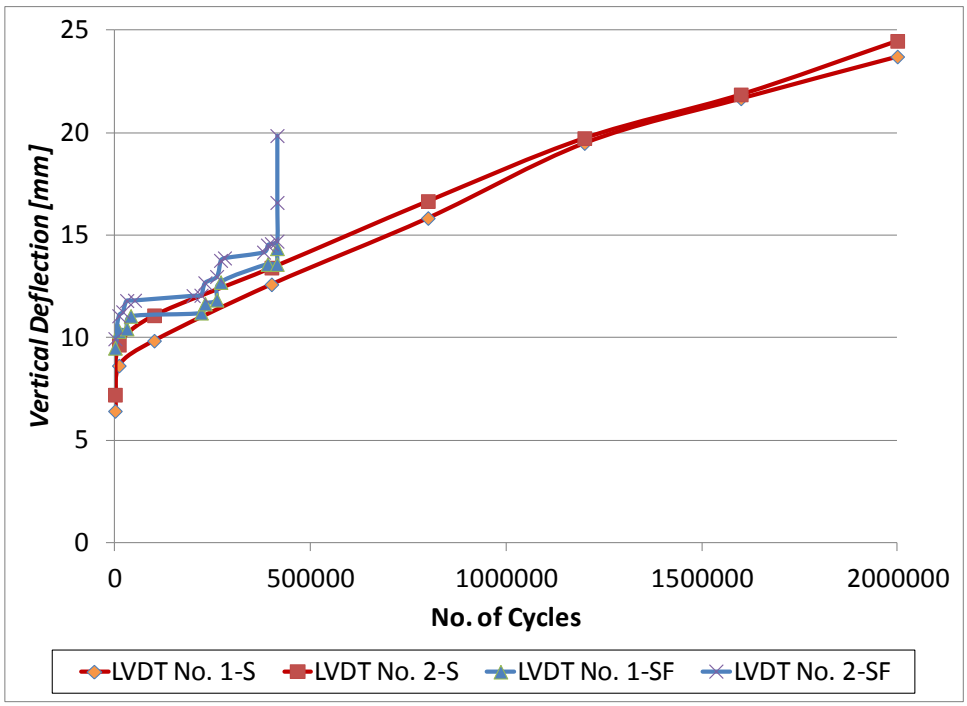

Figure 6.1a Comparison plot between maximum vertical deflection in Segments A and B vs. number of cycles; covering 2,000,000 cycles

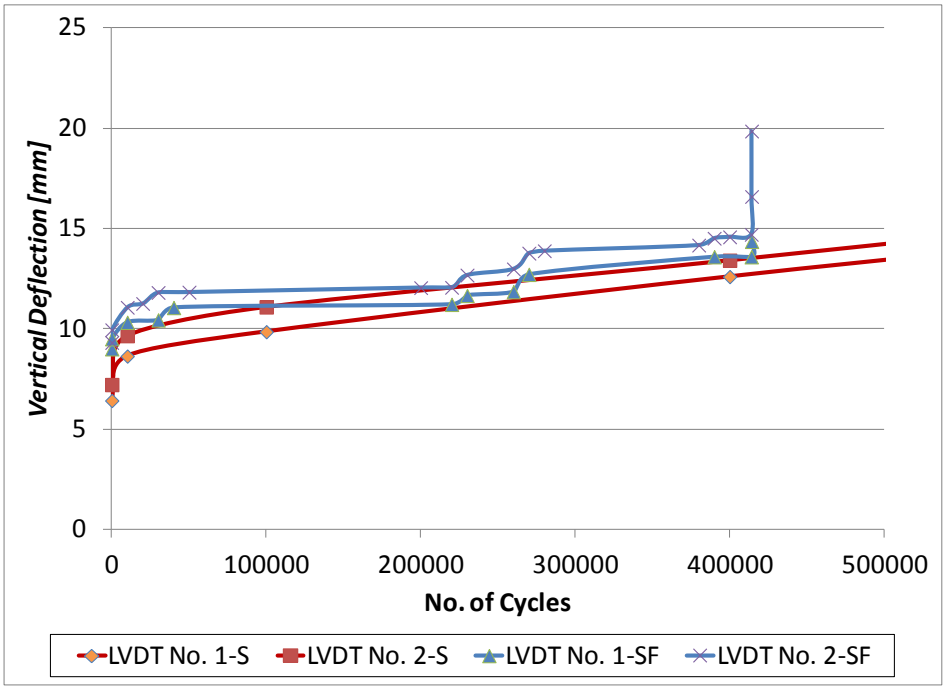

Figure 6.1b Comparison plot between maximum vertical deflection in Segments A and B vs. number of cycles; covering 500,000 cycles

6.3.3 Crack Width Comparison of Segments A and B

Maximum crack width versus no. of cycles for Segments A and B is plotted in Figures 6.2a and 6.2b. Pi Gauge No's 1-S, 2-S, 3-S, and 4-S were mounted to Segment A, and Pi Gauge No's 1-SF, 2-SF, 3-SF, and 4-SF were mounted to Segment B, for the purpose of recording crack width sizes. See previous Figure 4.5 for a plan view layout of the pi gauge program mentioned above.

For the first 10,000 cycles, Pi Gauge No's 2-SF, 3-SF, and 4-SF in Segment B recorded maximum crack widths below 1 mm. In the same 10,000 cycles, Pi Gauge No's 2-S and 3-S of Segment A recorded crack widths in the 1.5 to 2 mm range (Pi Gauge No's 1-S and 4-S of Segment A were not established until 167,164 and 690,000 cycles, respectively). Maximum crack widths in Segment B recorded by Pi Gauge No's 2-SF, 3-SF, and 4-SF remained below 1.5 mm right up until failure (maximum crack width size recorded by Pi Gauge No. 2-SF exceeded 1.5 mm only in the last couple thousand cycles when the structural integrity of the deck started to diminish). By 2,000,000 cycles, the majority of the crack width sizes recorded in Segment A were somewhere between 1.5 and 3 mm; whereas the only Pi Gauge in Segment B to record a crack width in that range was Pi Gauge No. 1-SF. Pi Gauge No's 4-S and 4-SF were mounted over top of deck cracks in Segments A and B, respectively. The top of deck maximum crack width measured in Segment B remained several magnitudes smaller than the one measured in Segment A.

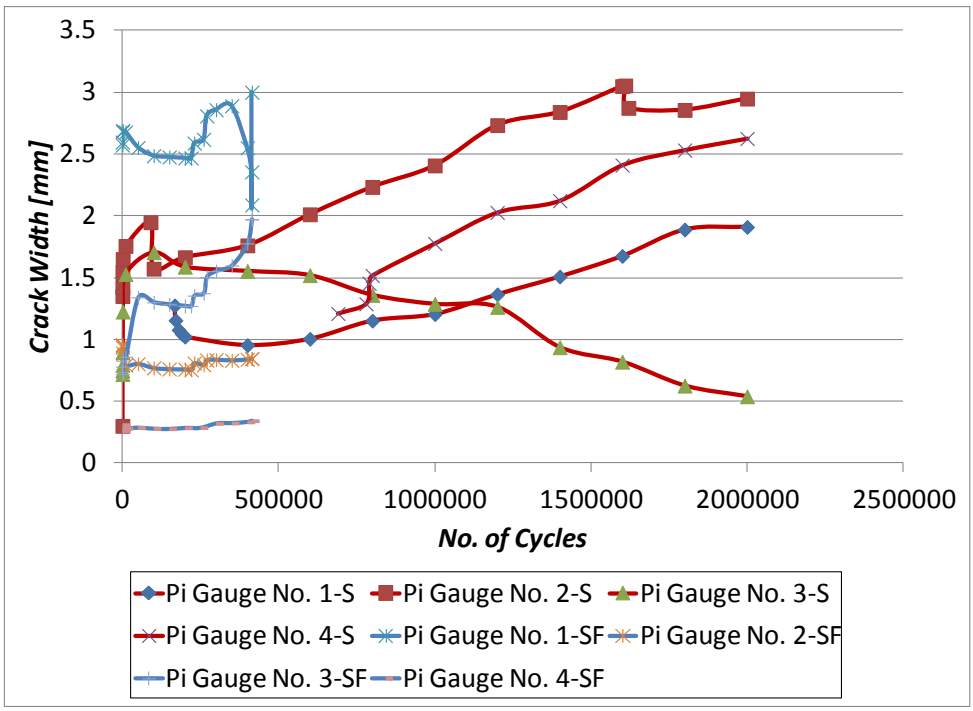

Figure 6.2a Comparison plot between maximum crack width in Segments A and B vs. number of cycles; covering 2,000,000 cycles

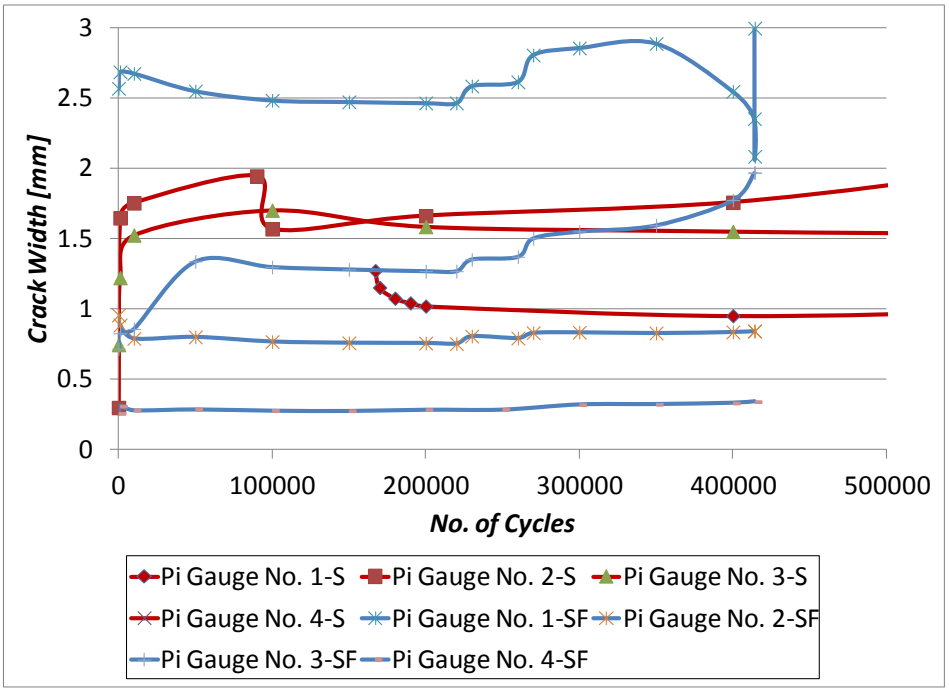

Figure 6.2b Comparison plot between maximum crack width in Segments A and B vs. number of cycles; covering 500,000 cycles

6.3.4 Internal Reinforcement Strain Behavior Comparison of Segments A and B

Maximum strain versus no. of cycles for internal bottom transverse reinforcement in Segments A and B is plotted in Figures 6.3a, 6.3b, and 6.3c (log scale). ESG No's 1-S-B, 2-S-B, and 3-S-B were attached to the internal bottom transverse steel reinforcement in Segment A, and ESG No's 1-SF-B, 2-SF-B, and 3-SF-B were attached to the internal bottom transverse GFRP reinforcement in Segment B, for the purpose of recording internal reinforcement strain. See previous Figure 4.7 for a plan view layout of the electronic strain gauge program mentioned above.

The bottom transverse reinforcement strain gauges in Segments A and B recorded relatively high strains in the bars between 2,000 and 5,000 με. All bottom transverse strain gauges stopped functioning before 100,000 cycles. Either the reinforcing steel and GFRP bars ruptured or the electronic strain gauges failed themselves due to the combination of high strains and continual fatigue loading. Rupturing of the reinforcement was the more likely culprit since evidence of this was witnessed when portions of spalling concrete fell from the soffit of Segment A, exposing the ruptured bottom transverse steel bar which ESG No. 2-S was attached to. On average, the bottom transverse steel reinforcement in Segment A sustained slightly lower strains and lasted several tens of thousands of cycles longer compared to the bottom transverse GFRP reinforcement in Segment B. ESG No. 2-SF-B lasted one cycle before signaling failure.

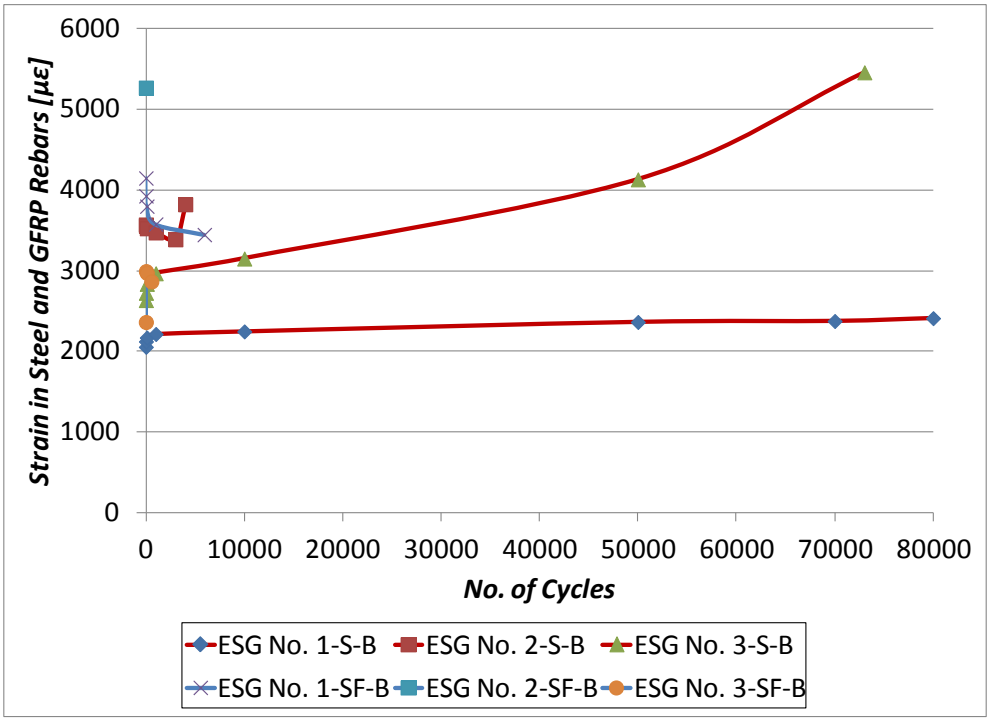

Figure 6.3a Comparison plot between maximum strain in bottom transverse steel and GFRP bars in Segments A and B respectively vs. number of cycles; covering 80,000 cycles

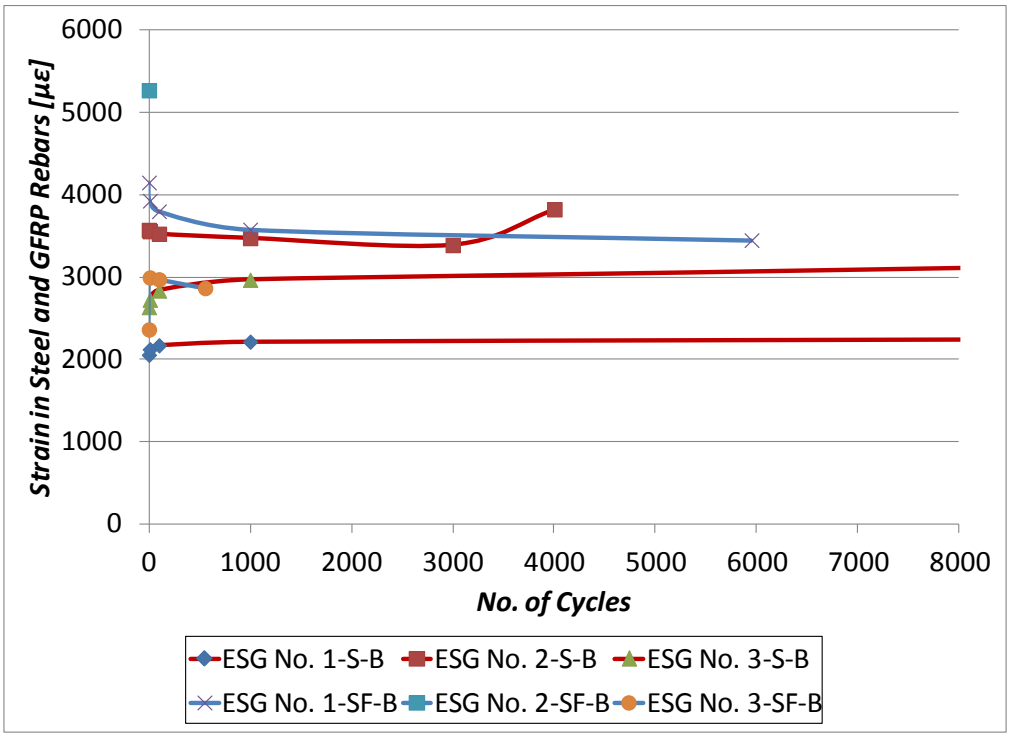

Figure 6.3b Comparison plot between maximum strain in bottom transverse steel and GFRP bars in Segments A and B respectively vs. number of cycles; covering 8,000 cycles

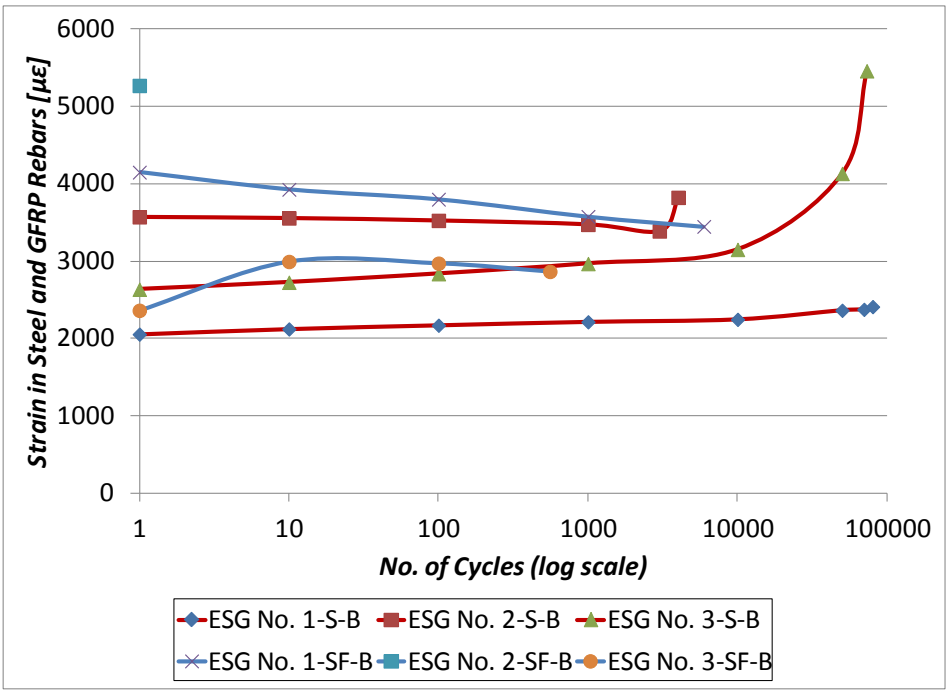

Figure 6.3c Comparison plot between maximum strain in bottom transverse steel and GFRP bars in Segments A and B respectively vs. number of cycles (log scale); covering 100,000 cycles

Maximum strain versus no. of cycles for internal bottom longitudinal reinforcement in Segments A and B is plotted in Figure 6.4a, 6.4b, and 6.4c (log scale). ESG No's 4-S-B, 5-S-B, and 6-S-B were attached to the internal bottom longitudinal steel reinforcement in Segment A, and ESG No's 4-SF-B, and 5-SF-B were attached to the internal bottom longitudinal GFRP reinforcement in Segment B, for the purpose of recording internal reinforcement strain. See previous Figure 4.7 for a plan view layout of the electronic strain gauge program mentioned above.

The strain gauges attached to the bottom longitudinal reinforcement in Segments A and B stayed below 2,000 με for the majority of their life span. The magnitude of strain in both types of bottom longitudinal reinforcement was more or less comparable. The major difference is that the steel reinforcement lasted several hundred thousand cycles longer than the GFRP reinforcement before failing.

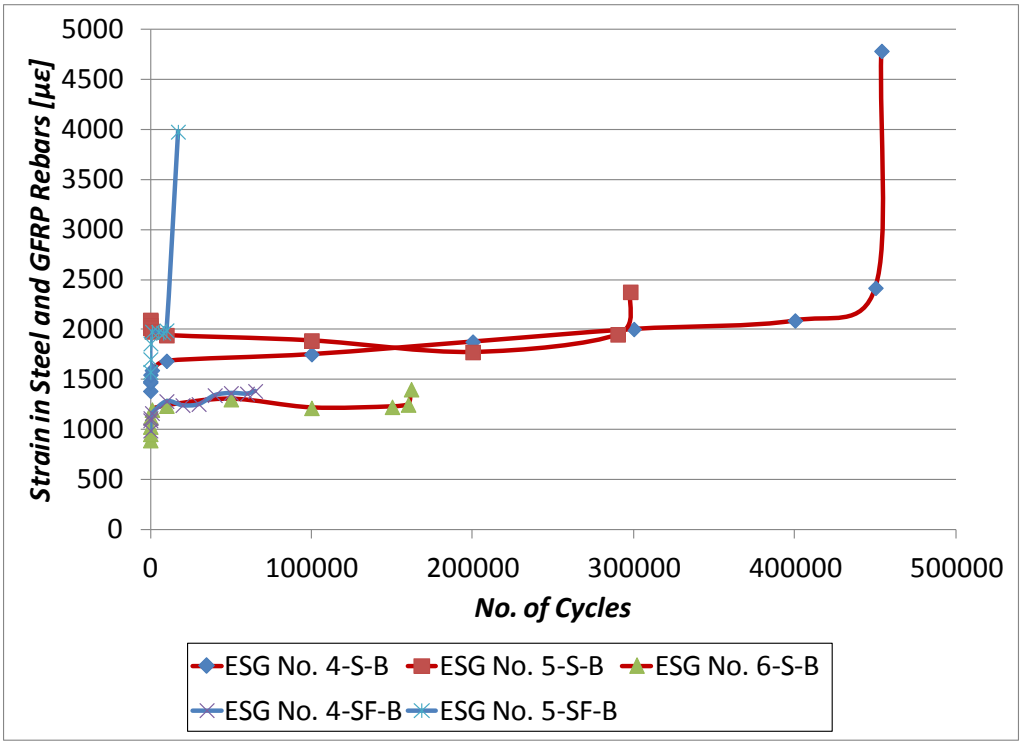

Figure 6.4a Comparison plot between maximum strain in bottom longitudinal steel and GFRP bars in Segments A and B respectively vs. number of cycles; covering 500,000 cycles

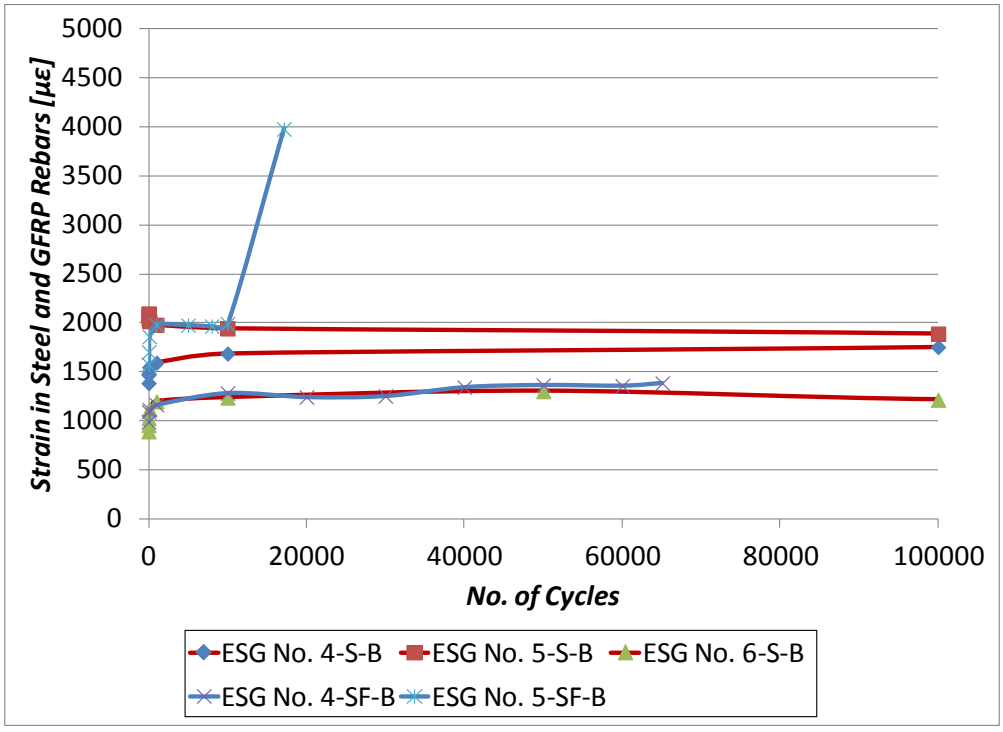

Figure 6.4b Comparison plot between maximum strain in bottom longitudinal steel and GFRP bars in Segments A and B respectively vs. number of cycles; covering 100,000 cycles

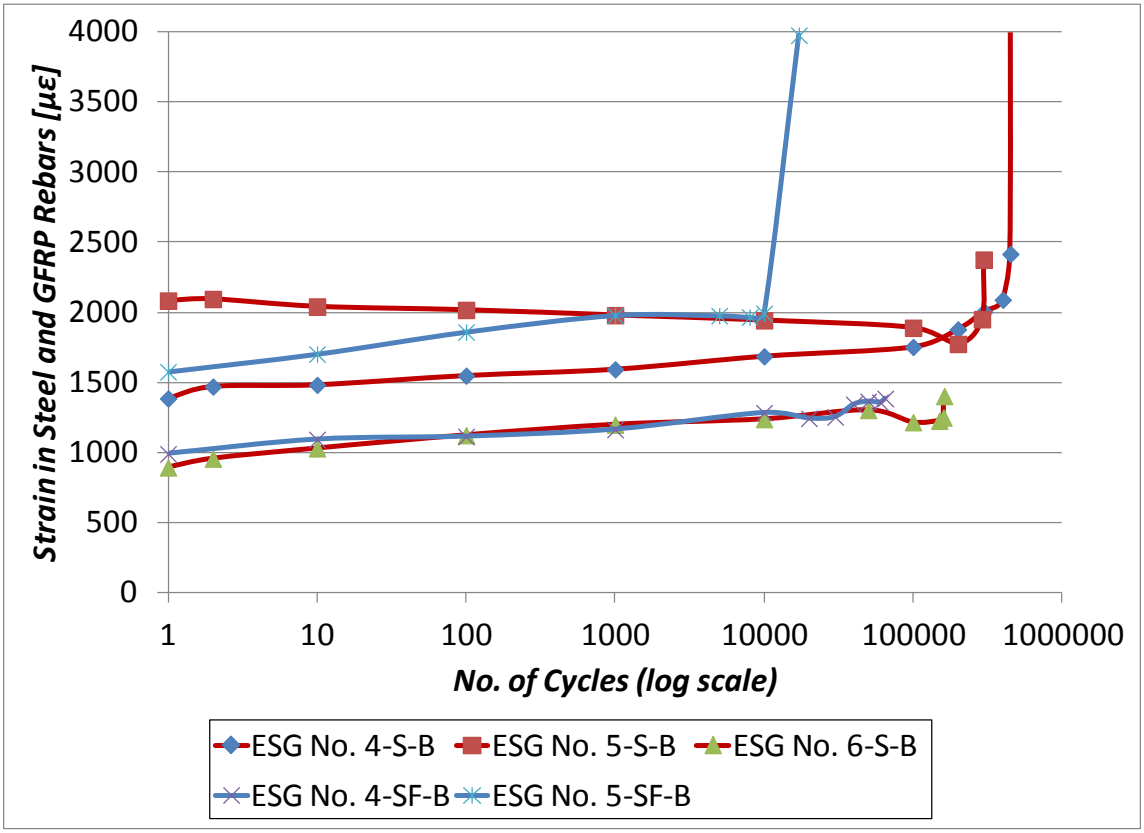

Figure 6.4c Comparison plot between maximum strain in bottom longitudinal steel and GFRP bars in Segment A and B respectively vs. number of cycles (log scale); over 1,000,000 cycles

Maximum strain versus no. of cycles for internal top transverse reinforcement in Segments A and B is plotted in Figure 6.5a, 6.5b, and 6.5c (log scale). ESG No's 1-S-T, 2-S-T, 3-S-T, 4-S-T, and 5-S-T were attached to the internal top transverse steel reinforcement in Segment A, and ESG No's 1-SF-T, 2-SF-T, 3-SF-T, 4-SF-T, and 5-SF-T were attached to the internal top transverse GFRP reinforcement in Segment B, for the purpose of recording internal reinforcement strain. See previous Figure 4.8 for a plan view layout of the electronic strain gauge program mentioned above.

For the first 100,000 cycles the strain in the steel reinforcement in Segment A remained below 500 με and the GFRP reinforcement in Segment B remained below 1,000 με (except for the readings coming

from ESG No. 3-SF-T). Only ESG No's 5-S-T and 3-SF-T recorded strains above 2,000 με at any point during the two tests done on Segments A and B. All the electronic strain gauges in Segment B failed in and around 300,000 cycles, while all the electronic strain gauges in Segment A failed between 600,000 and 1,100,000 cycles.

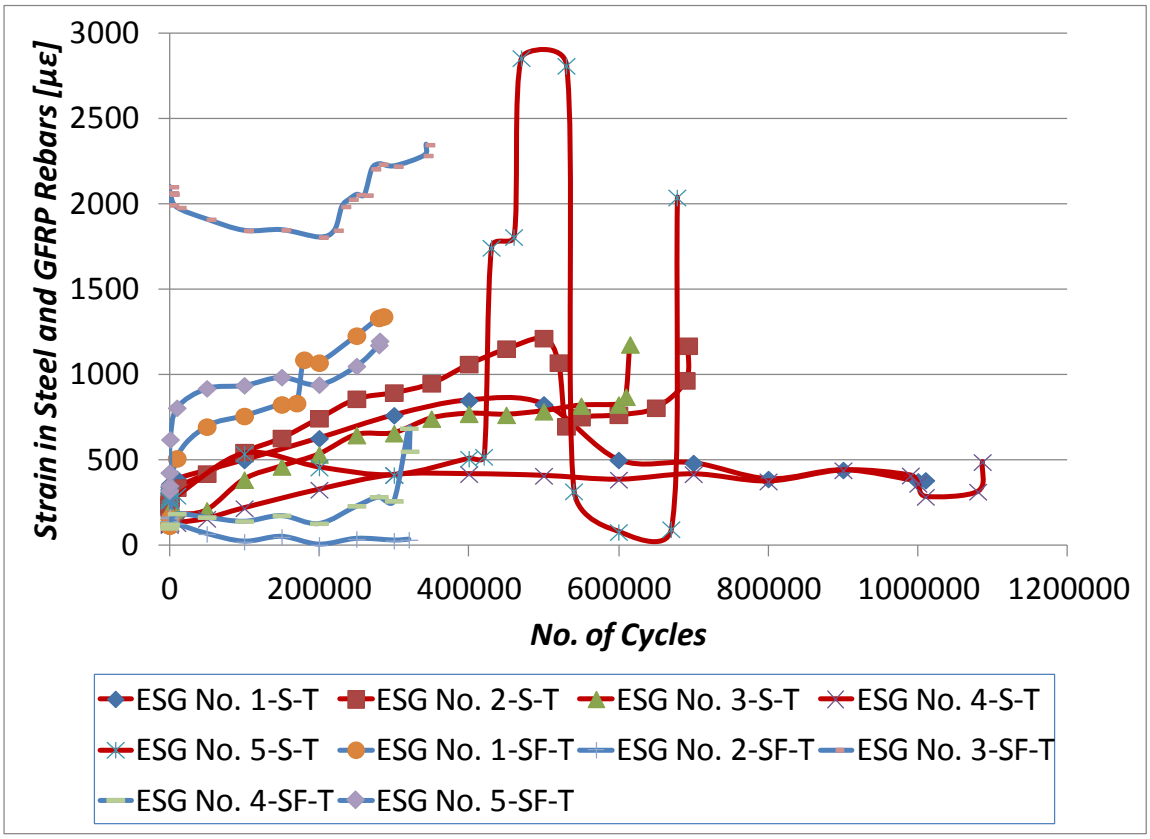

Figure 6.5a Comparison plot between maximum strain in top transverse steel and GFRP bars in Segments A and B respectively vs. number of cycles; covering 1,200,000 cycles

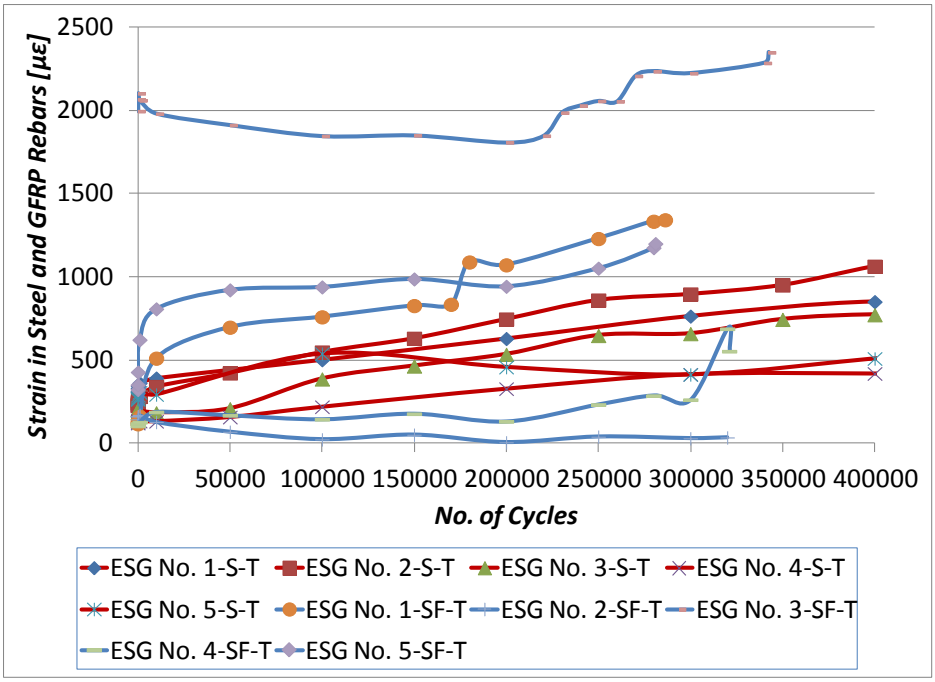

Figure 6.5b Comparison plot between maximum strain in top transverse steel and GFRP bars in Segments A and B respectively vs. number of cycles; covering 400,000 cycles

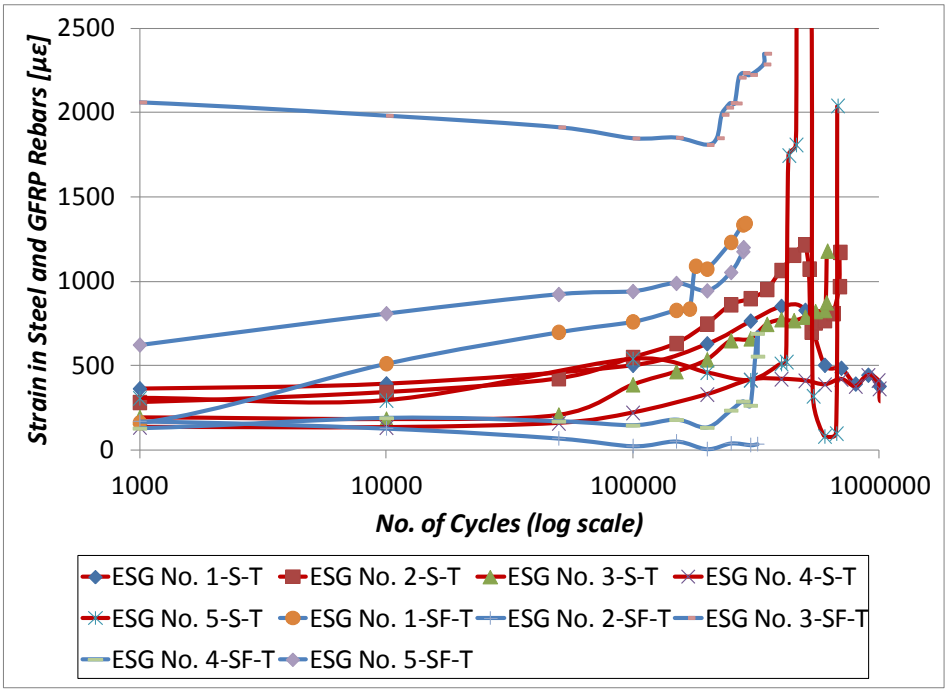

Figure 6.5c Comparison plot between maximum strain in top transverse steel and GFRP bars in Segments A and B respectively vs. number of cycles (log scale); covering 1,000,000 cycles

6.3.4 Comparison between Internal Bottom Transverse Steel Reinforcement (Segment A) and External Steel Strap Reinforcement (Segment B) in terms of Strain Behavior

Maximum strain versus no. of cycles for internal bottom transverse steel reinforcement in Segment A and external steel strap reinforcement in Segment B is plotted in Figure 6.6. ESG No's 1-S-B, 2-S-B, and 3-S-B were attached to the internal bottom transverse steel reinforcement in Segment A, and Strap ESG No's 1, 2, 3, and 4 were attached to the external steel strap reinforcement in Segment B. See previous Figures 4.7 and 4.10 for a plan view layout of the electronic strain gauge programs mentioned above.

The steel straps in Segment B barely exceeded 1,000 με during their entire life span in terms of number of cycles, which was for all intensive purposes 414,223 cycles for Strap No's 1 and 4, 261,100 cycles for Strap No. 3, and 227,000 cycles for Strap No.2. On the other hand, not one bottom transverse reinforcing bar in Segment A (of those being monitored) achieved 80,000 cycles before failing. Aside from steel Strap No's 2 and 3 rupturing prematurely due to weakened cross-sections near the stud welds, the steel straps in Segment B undoubtedly outperformed the bottom transverse steel rebar in Segment A in terms of safe strain levels and number of cycles achieved.

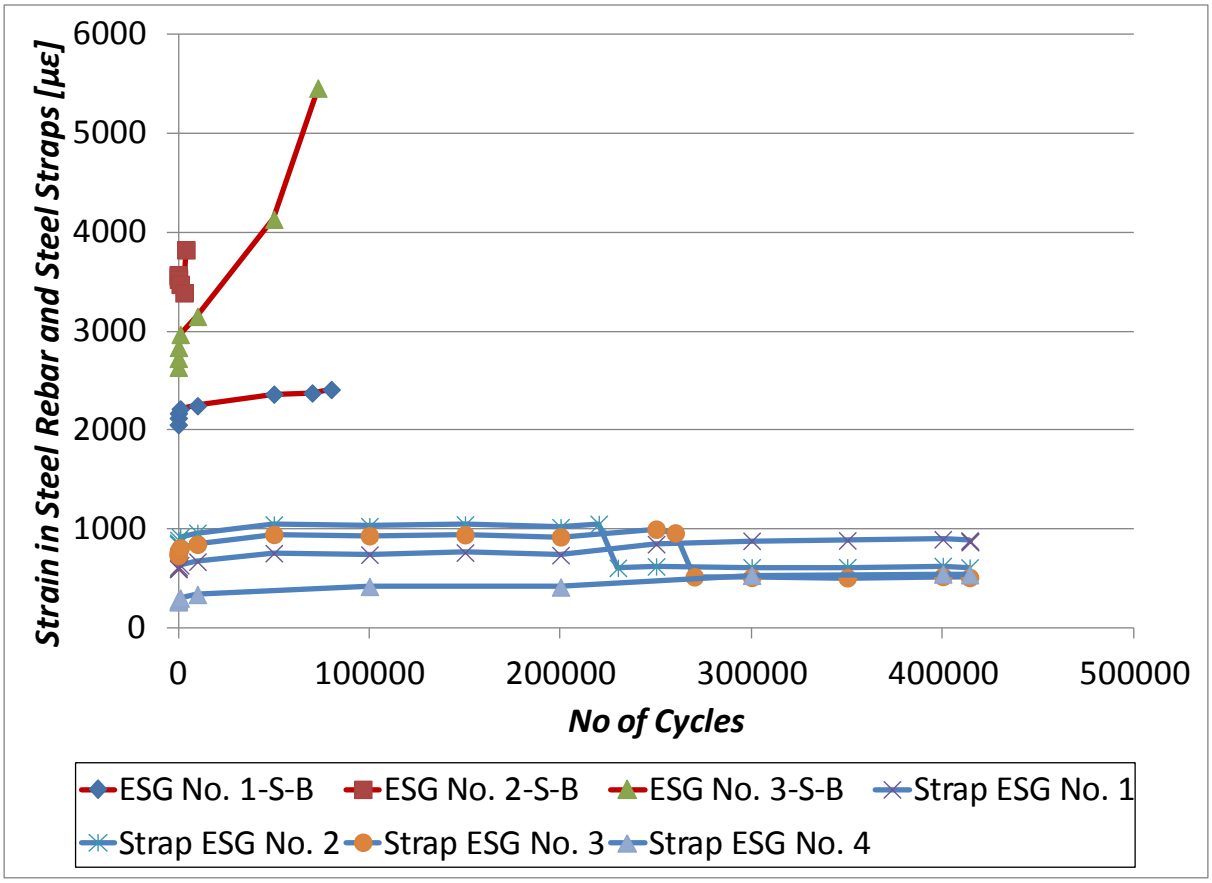

Figure 6.6 Comparison plot between maximum strain in bottom transverse steel rebar in Segment A and external transverse steel straps in Segment B vs. number of cycles; covering 500,000 cycles

6.3.5 Concrete Strain Comparison of Segments A and B

Maximum top of deck concrete strain versus no. of cycles for Segments A and B is plotted in Figure 6.7. See previous Figure 4.14 for a plan view layout of the electronic strain gauge program for concrete strain.

The compressive strain in concrete in Segment B jumped to almost double that of Segment A during the first cycle of loading to 570 kN, as shown in Figure 6.7. After only 8,011 cycles, the concrete strain gauge in Segment B stopped functioning either because the electronic strain gauge reached its ultimate capacity or the glued connection to the concrete failed due to fatigue exposure. On the contrary, the concrete strain gauge in Segment A survived 2,000,000 cycles and the compressive strain in the concrete remained at fairly low, but increasing, maximum values throughout its lifespan.

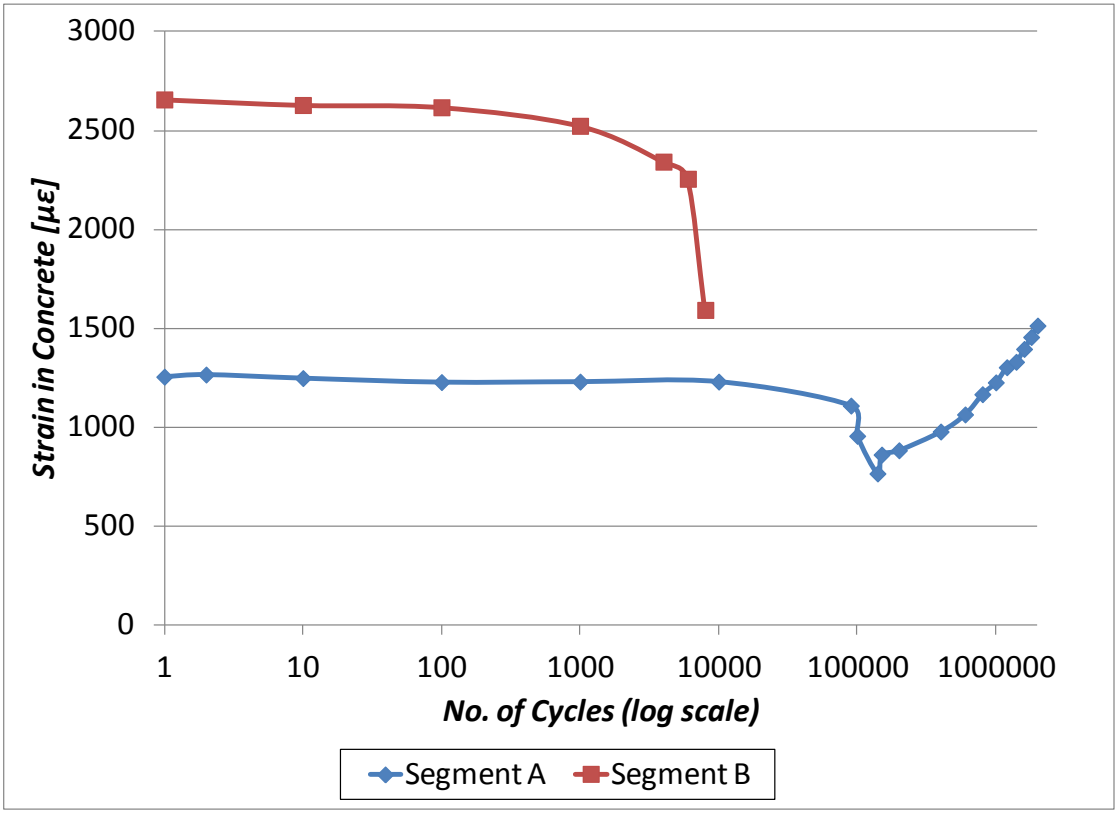

Figure 6.7 Comparison plot between maximum strain in concrete in Segments A and B vs. number of cycles; covering 1,000,000 cycles

6.4 Limit States Requirements and Comparison of Segments A and B

The fatigue load applied to Segments A and B for this experiment (570 kN) was several magnitudes larger than any realistic single dual tire load that would ever be present on a bridge deck in Canada. Therefore, it is more applicable to extract the data from the very first load cycle to 570 kN, at magnitudes corresponding to the Ultimate Limit State (ULS), Serviceability Limit State (SLS), and Fatigue Limit State (FLS) design loads, and compare the values with limits provided in appropriate design codes and standards. The scope here is limited to the Canadian Highway Bridge Design Code, in particular, the CAN/CSA-S6-00 and the CAN/CSA-S6-06. However, the CAN/CSA-S6-00/06 do not specify limits for several categories in deflection, crack width and reinforcing strain, thus, the American Concrete Institute (ACI

440.1R-01) and the ISIS Canada Research Network Design Manual No. 3 (Reinforcing Concrete Structures with Fibre Reinforced Polymers) are also referenced in this section. As previously discussed, Segments A and B were designed as a full scale concrete bridge deck based on CAN/CSA-S6-00 requirements, however, in recognition that all concrete bridge decks are now designed based on requirements provided in the most recent CAN/CSA-S6-06, both codes are examined for the purpose of showing that the bridge deck in this experiment is compatible with both code requirements in terms of design, serviceability, and fatigue limits. Fortunately, the main criteria examined in this study was in terms of deflection, crack width, reinforcement strain and concrete strain, and it just so happens that the design, serviceability and fatigue limits for the criteria listed above are identical for both CAN/CSA-S6-00 and CAN/CSA-S6-06 at respective Ultimate Limit State, Serviceability Limit State, and Fatigue Limit State design loads. Design loads and load factors are also identical for both CAN/CSA-S6-00 and CAN/CSA-S6-06. The Ultimate Limit State, Serviceability Limit State, and Fatigue Limit State design loads and corresponding load factors, for both CAN/CSA-S6-00 and CAN/CSA-S6-06, are presented in Table 6.1. The maximum allowable wheel load on a concrete bridge deck, as specified in the CAN/CSA-S6-00/06, is 87.5 kN.

Table 6.1 CAN/CSA-S6-00/06 maximum allowable wheel load for a concrete bridge deck, with corresponding design loads at Ultimate Limit State (ULS), Serviceability Limit State (SLS), and Fatigue Limit State (FLS)

	Ultimate Limit State (ULS)	Serviceability Limit State (SLS)	Fatigue Limit State (FLS)
Max Wheel Load (kN) P	87.5	87.5	87.5
Max Live Load Factor α_L	1.7	0.9	1
Max Impact Factor I	1.4	1.4	1.4
Design Load (kN) $=P*\alpha_L*I$	208	110	122

6.4.1 Deflection Limit Criteria

The CAN/CSA-S6-00/06 do not specify any maximum serviceability deflection limit for a slab-on-girder bridge deck, therefore the ACI 440.1R-01 is referenced in this case. The ACI 440.1R-01 specifies the maximum serviceability deflection limit to be span/600, where the span is equal to the perpendicular distance between the supporting girders center lines, and span is in millimeters. For the sake of comparison, and the goal of comparing Segments A & B to a deflection limit, the maximum deflection limit in the ACI 444.1R-01 will be used as the base reference, although this may not necessarily be the true accepted limit. Both Segments A and B had spans of 2,500 mm; therefore, the maximum serviceability deflection limit was 4.17 mm. The maximum vertical deflections corresponding to the maximum allowable wheel load, the Ultimate Limit State (ULS) design load, the Serviceability Limit State (SLS) design load, and the Fatigue Limit State (FLS) design load for LVDT No. 1-S and LVDT No. 2-S of Segment A, and LVDT No. 1-SF and LVDT No. 2-SF of Segment B are all shown in Table 6.2. The largest deflection recorded at any of the load states was 2.86 mm, and it was recorded by LVDT No. 1-SF at the Ultimate Limit State (ULS) design load of 208 kN. What this signifies is that even at the Ultimate Limit State (ULS) design load, which is almost double the Serviceability Limit State (SLS) design load, the deflections in both Segments A and B were well below the maximum serviceability deflection limit of 4.17 mm. Overall, the deflections in Segment A were smaller than those of Segment B; however, both Segments recorded maximum deflections well below the maximum serviceability deflection limit for all load states.

Table 6.2 Comparison between the serviceability concrete bridge deck deflection limit and the maximum vertical deflection in Segments A and B at corresponding CAN/CSA-S6-00/06 maximum allowable wheel load, Ultimate Limit State (ULS) design load, Serviceability Limit State (SLS) design load, and Fatigue Limit State (FLS) design load, recorded during the first cycle of loading

		Maximum Vertical Deflection (mm)			
		Segment A (Steel Reinforced)		Segment B (Steel-Free)	
Load Designation	Load (KN)	LVDT No. 1-S	LVDT No. 2-S	LVDT No. 1-SF	LVDT No. 2-SF
Max Wheel Load (P)	87.5	0.02	0.35	0.60	0.42
SLS Load	110	0.03	0.48	0.80	0.60
FLS Load	122	0.02	0.54	1.17	1.03
ULS Load	208	1.02	1.67	2.86	2.73
	Serviceability Deflection Limit (mm) [span/600]	≤ 4.17	≤ 4.17	≤ 4.17	≤ 4.17

6.4.2 Crack Width Limit Criteria

The CAN/CSA-S6-00/06 and the ACI 440.1R-01 specifies the maximum serviceability crack width limit for a slab-on-girder bridge deck to be 0.5 mm; this is not necessarily the case for empirically designed concrete bridge decks, however for the sake of comparison it will be used in reference as well. The maximum crack widths corresponding to the maximum allowable wheel load, the Ultimate Limit State (ULS) design load, the Serviceability Limit State (SLS) design load, and the Fatigue Limit State (FLS) design load for Pi Gauge No's. 1-S, 2-S, 3-S, and 4-S of Segment A, and Pi Gauge No's. 1-SF, 2-SF, 3-SF, and 4-SF of Segment B, are all shown in Table 6.3. The largest crack width recorded at any of the load states was 1.067 mm, and was recorded by Pi Gauge No. 1-SF at the Ultimate Limit State (ULS) design load of 208 kN. Although 1.067 mm exceeds 0.5 mm, the maximum serviceability crack width limit is designated for

Serviceability Limit State (SLS) design loads. The largest crack width under Serviceability Limit State (SLS) design load was 0.195 mm (recorded by Pi Gauge No. 2-S at the Serviceability Limit State (SLS) design load of 110 kN), which is significantly smaller than 0.5 mm. All deflection recordings, except for one (1.067 mm mentioned above), were below 0.5 mm and therefore.

Table 6.3 Comparison between the serviceability concrete bridge deck crack width limit and the maximum crack width in Segments A and B at corresponding CAN/CSA-S6-00/06 maximum allowable wheel load, Ultimate Limit State (ULS) design load, Serviceability Limit State (SLS) design load, and Fatigue Limit State (FLS) design load, recorded during the first cycle of loading

		Maximum Crack Width (mm)							
		Segment A (Steel Reinforced)				Segment B (Steel-Free)			
Load Designation	Load (KN)	Pi Gauge No. 1-S	Pi Gauge No. 2-S	Pi Gauge No. 3-S	Pi Gauge No. 4-S	Pi Gauge No. 1-SF	Pi Gauge No. 2-SF	Pi Gauge No. 3-SF	Pi Gauge No. 4-SF
Max Wheel Load (P)	87.5	0.055	0.177	0.058	N/A	0.069	0.027	0.018	0.007
SLS Load	110	0.066	0.195	0.066	N/A	0.121	0.039	0.021	0.008
FLS Load	122	0.071	0.202	0.070	N/A	0.333	0.039	0.031	0.012
ULS Load	208	0.242	0.242	0.206	N/A	1.067	0.040	0.044	0.047
	Serviceability Crack Width Limits (mm)	≤ 0.5	≤ 0.5	≤ 0.5	≤ 0.5	≤ 0.5	≤ 0.5	≤ 0.5	≤ 0.5

6.4.3 Internal Reinforcement Strain Limit Criteria

The CAN/CSA-S6-00/06 specifies the maximum steel reinforcement serviceability strain limit to be 1,200 με and the yielding strain of steel reinforcement to be 2,000 με. The maximum steel reinforcement strain corresponding to the maximum allowable wheel load, the Ultimate Limit State (ULS) design load, the Serviceability Limit State (SLS) design load, and the Fatigue Limit State (FLS) design load for the eleven electronic strain gauges installed to the internal steel reinforcement in Segment A is shown in Table 6.4.

The largest steel reinforcement strain recorded at the Serviceability Limit State (SLS) design load of 110 kN was 154.15 με, and was recorded by ESG No. 5-S-B. Therefore, all maximum steel reinforcement strains recorded at the Serviceability Limit State (SLS) design load were below the maximum steel reinforcement serviceability strain limit of 1,200 με. The largest steel reinforcement strain recorded at the Ultimate Limit State (ULS) design load of 208 kN was 1,071.41 με, and was recorded by ESG No. 5-S-B. Therefore, all maximum steel reinforcement strains recorded at the Ultimate Limit State (ULS) design load were below the yielding strain of steel, which is 2,000 με.

Table 6.4 Comparison between the steel reinforcement serviceability strain limit and the steel reinforcement strain in Segment A at corresponding CAN/CSA-S6-00/06 maximum allowable wheel load, Ultimate Limit State (ULS) design load, Serviceability Limit State (SLS) design load, and Fatigue Limit State (FLS) design load, recorded during the first cycle of loading

		Strain in Steel Reinforcement (με) - Segment A										
		BTM Transverse Bar ESG			BTM Longitudinal Bar ESG			TOP Transverse Bar ESG				
Load Designation	**Load (KN)**	**ESG No. 1-S-B**	**ESG No. 2-S-B**	**ESG No. 3-S-B**	**ESG No. 4-S-B**	**ESG No. 5-S-B**	**ESG No. 6-S-B**	**ESG No. 1-S-T**	**ESG No. 2-S-T**	**ESG No. 3-S-T**	**ESG No. 4-S-T**	**ESG No. 5-S-T**
Max Wheel Load (P)	87.5	108.83	167.01	81.93	70.60	135.19	37.01	105.61	65.28	-9.04	57.99	90.61
SLS Load	110	132.23	197.11	99.59	81.91	154.15	44.35	108.95	61.19	-25.97	54.54	96.21
FLS Load	122	145.23	215.85	108.79	90.98	167.75	48.11	112.07	59.68	-33.30	53.46	99.45
ULS Load	208	880.33	1,068.45	174.91	233.10	1,071.41	172.35	139.02	70.78	-24.68	51.09	134.48
	Serviceability Strain Limit (με)	≤ 1,200	≤ 1,200	≤ 1,200	≤ 1,200	≤ 1,200	≤ 1,200	≤ 1,200	≤ 1,200	≤ 1,200	≤ 1,200	≤ 1,200
	Steel Yielding Strain (με)	≤ 2,000	≤ 2,000	≤ 2,000	≤ 2,000	≤ 2,000	≤ 2,000	≤ 2,000	≤ 2,000	≤ 2,000	≤ 2,000	≤ 2,000

Note: Negative values signify compressive stresses

The CAN/CSA-S6-00/06 do not specify a maximum GFRP reinforcement serviceability strain limit for a slab-on-girder bridge deck, therefore the ISIS Canada Research Network Design Manual No. 3 (Reinforcing Concrete Structures with Fibre Reinforced Polymers) is referenced in this case. The ISIS Canada Research Network Design Manual No. 3 (Reinforcing Concrete Structures with Fibre Reinforced Polymers) specifies

the maximum GFRP reinforcement serviceability strain limit to be 2,000 με. While the ultimate GFRP reinforcement strain limit for the specific GFRP material (V-Rod) used for this experiment is 18,500 με. The maximum GFRP reinforcement strain corresponding to the maximum allowable wheel load, the Ultimate Limit State (ULS) design load, the Serviceability Limit State (SLS) design load, and the Fatigue Limit State (FLS) design load for the ten electronic strain gauges installed to the internal GFRP reinforcement in Segment B is shown in Table 6.5. The largest GFRP reinforcement strain recorded at the Serviceability Limit State (SLS) design load of 110 kN was 458.30 με, and was recorded by ESG No. 2-SF-B. Therefore, all maximum GFRP reinforcement strains recorded at the Serviceability Limit State (SLS) design load were below the maximum GFRP reinforcement serviceability strain limit of 2,000 με. The largest GFRP reinforcement strain recorded at the Ultimate Limit State (ULS) design load of 208 kN was 3,012.33 με, and was recorded by ESG No. 2-SF-B. Therefore, all maximum GFRP reinforcement strains recorded at the Ultimate Limit State (ULS) design load were below the ultimate GFRP reinforcement strain limit of 18,500 με.

Table 6.5 Comparison between the GFRP reinforcement serviceability strain limit and the GFRP reinforcement strain in Segment B at corresponding CAN/CSA-S6-00/06 maximum allowable wheel load, Ultimate Limit State (ULS) design load, Serviceability Limit State (SLS) design load, and Fatigue Limit State (FLS) design load, recorded during the first cycle of loading

		Strain in GFRP Reinforcement (με) - Segment B									
		BTM Transverse Bar ESG			BTM Longitudinal Bar ESG		TOP Transverse Bar ESG				
Load Designation	Load (KN)	ESG No. 1-SF-B	ESG No. 2-SF-B	ESG No. 3-SF-B	ESG No. 4-SF-B	ESG No. 5-SF-B	ESG No. 1-SF-T	ESG No. 2-SF-T	ESG No. 3-SF-T	ESG No. 4-SF-T	ESG No. 5-SF-T
Max Wheel Load (P)	87.5	38.90	237.76	32.25	31.19	31.86	13.35	-24.82	-48.69	-33.22	22.46
SLS Load	110	57.24	458.30	49.83	39.07	46.85	19.07	-29.46	-44.59	-39.27	29.05
FLS Load	122	100.91	1,381.72	38.08	24.72	148.99	14.43	-35.49	212.47	-40.56	32.94
ULS Load	208	2,216.39	3,012.33	73.22	53.84	1,326.47	30.19	-27.73	753.79	-29.44	80.12
	Serviceability Strain Limit (με)	≤ 2,000	≤ 2,000	≤ 2,000	≤ 2,000	≤ 2,000	≤ 2,000	≤ 2,000	≤ 2,000	≤ 2,000	≤ 2,000
	Ultimate Strain (με)	≤ 18,500	≤ 18,500	≤ 18,500	≤ 18,500	≤ 18,500	≤ 18,500	≤ 18,500	≤ 18,500	≤ 18,500	≤ 18,500

Note: Negative values signify compressive stresses

In comparison, the strain in the GFRP reinforcement of Segment B was on average lower than the strain in the steel reinforcement of Segment A, at the Serviceability Limit State (SLS) design load. Well on the other hand, the strain in the steel reinforcement of Segment A was on average lower than the strain in the GFRP reinforcement of Segment B, at the Ultimate Limit State (ULS) design load. All reinforcement strain recordings, at every loading state, were below their respective strain limits and therefore, Segments A and B can be considered safe designs in terms of internal reinforcement strain limit criteria.

6.4.4 External Reinforcement Strain Limit Criteria

Only Segment B had external reinforcement incorporated into its design and it was in the form of steel straps. The CAN/CSA-S6-00/06 specifies the maximum steel serviceability strain limit to be 1,200 με and the yielding strain of steel to be 2,000 με. The maximum steel strap strain corresponding to the maximum allowable wheel load, the Ultimate Limit State (ULS) design load, the Serviceability Limit State (SLS) design load, and the Fatigue Limit State (FLS) design load for Strap ESG No's. 1, 2, 3, and 4 of Segment B is shown in Table 6.6. The largest steel strap strain recorded at the Serviceability Limit State (SLS) design load of 110 kN was 83.76 με, and was recorded by Strap ESG No. 2. Therefore, all maximum steel strap strains recorded at the Serviceability Limit State (SLS) design load were below the maximum steel serviceability strain limit of 1,200 με. The largest steel strap strain recorded at the Ultimate Limit State (ULS) design load of 208 kN was 317.76 με, and was recorded by Strap ESG No. 2. Therefore, all maximum steel strap strains recorded at the Ultimate Limit State (ULS) design load were below the yielding strain of steel, which is 2,000 με. The strains recorded in the steel straps at any load state were significantly lower than the serviceability and yielding strain limits of steel. This large difference in actual strain and specified strain limits demonstrates the enormous loading capacity which the steel-free slab-on-girder bridge deck design offers, and also the large margin of safety provided in the external steel strap reinforcement. Due to the impressive nature of the steel straps in terms of strain behavior, in particular remaining several

magnitudes below the serviceability and yielding strain of steel, Segment B can be considered an exceedingly safe design in terms of external reinforcement strain limit criteria.

Table 6.6 Comparison between the steel strap serviceability strain limit and the steel strap strain in Segment B at corresponding CAN/CSA-S6-00/06 maximum allowable wheel load, Ultimate Limit State (ULS) design load, Serviceability Limit State (SLS) design load, and Fatigue Limit State (FLS) design load, recorded during the first cycle of loading

Load Designation	Load (KN)	Strain in Steel Strap Reinforcement (με)			
		Transverse Steel Strap ESG			
		Strap ESG No. 1	Strap ESG No. 2	Strap ESG No. 3	Strap ESG No. 4
Max Wheel Load (P)	87.5	48.85	63.59	42.37	9.78
SLS Load	110	62.66	83.76	54.99	11.94
FLS Load	122	86.19	127.24	84.02	14.96
ULS Load	208	204.13	317.76	249.97	65.13
	Serviceability Strain Limit (με)	≤ 1,200	≤ 1,200	≤ 1,200	≤ 1,200
	Steel Yielding Limit (με)	≤ 2,000	≤ 2,000	≤ 2,000	≤ 2,000

6.4.5 Concrete Strain Limit Criteria

The CAN/CSA-S6-00/06 specifies the ultimate compressive strain in concrete to be 3,500 με. The maximum compressive strain in concrete corresponding to the maximum allowable wheel load, the Ultimate Limit State (ULS) design load, the Serviceability Limit State (SLS) design load, and the Fatigue Limit State (FLS) design load for CONC ESG S of Segment A, and CONC ESG SF of Segment B, are shown in Table 6.7. Strain values in Table 6.7 are negative because they are in compression. The largest compressive

concrete strain recorded at any of the load states was 1,356.85 με, and was recorded by CONC ESG SF at the Ultimate Limit State (ULS) design load of 208 kN. Therefore, all the concrete strains recorded at all load stages were below the ultimate compressive strain in concrete, which is 3,500 με. The compressive strain in concrete for Segment B is noticeably larger than that of Segment A; however, both segments show strains several magnitudes smaller than the ultimate compressive strain in concrete, and therefore can both be considered as safe designs in terms of concrete strain limit criteria.

Table 6.7 Comparison between the ultimate concrete serviceability strain limit and the maximum concrete strain in Segments A and B at corresponding CAN/CSA-S6-00/06 maximum allowable wheel load, Ultimate Limit State (ULS) design load, Serviceability Limit State (SLS) design load, and Fatigue Limit State (FLS) design load, recorded during the first cycle of loading

		Maximum Concrete Strain (με)	
		Segment A (Steel Reinforced)	Segment B (Steel-Free)
Load Designation	**Load (KN)**	**CONC ESG S**	**CONC ESG SF**
Max Wheel Load (P)	87.5	-66.89	-272.69
SLS Load	110	-94.51	-367.61
FLS Load	122	-109.18	-555.34
ULS Load	208	-245.14	-1,356.85
	Ultimate Concrete Strain (με)	≥ -3,500	≥ -3,500

Note: Negative values signify compressive stresses

Chapter 7

Conclusion

7.1 General

In the spirit of comparing the two concrete bridge decks tested in this experimental program, namely

1) Segment A: Conventional steel reinforced concrete bridge deck, and
2) Segment B: Steel-free concrete bridge deck (second generation),

only one of the segments will be concluded superior in each of the following categories: endurance, durability, mode of failure, deflection, crack width, reinforcement strain, concrete strain, and overall performance. Conclusions in Section 7.2 will be based solely on the test results observed in this study.

Segments A and B will also be concluded as safe designs in section 7.3, in terms of serviceability and ultimate limit state criteria as presented in the CAN/CSA-S6-00/06, as well as the ACI 440.1R-01 and the ISIS Canada Research Network Design Manual No. 3 (Reinforcing Concrete Structures with Fibre Reinforced Polymers).

Finally, an overall conclusion will be provided in Section 7.4 that encompasses the results acquired in this experimental program.

7.2 Conclusion by Category

7.2.1 Endurance

Segment A endured 2,000,000 cycles with no immediate signs of failing before having to be statically loaded to failure. Segment B endured only 414,223 cycles before succumbing to fatigue induced punching shear failure. Segment A was clearly the prevalent bridge deck in terms of endurance.

However, it should be noted that Segment B failed prematurely, and hadn't its two main steel reinforcing straps ruptured at the weakened shear stud weld locations at such an early stage in the loading of the structure, there is strong evidence to support that Segment B would have continued to resist loading for a prolonged period of time.

7.2.2 Durability

Although Segment B endured less than a quarter of the cycles of Segment A, segment A appeared to sustain a higher percentage of visible damage during that equivalent period. Segment B had both less wide spread cracking and significantly less spalling of concrete.

7.2.3 Mode of Failure

Both segments failed in the preferred mode of failure, which is punching shear failure. The only difference was Segment A failed in punching shear failure due to an ultimate static load of 926 kN, whereas Segment B failed in punching shear failure under fatigue loading at a consistent cyclic load of 570 kN.

7.2.4 Deflection

In the very early stages of loading, Segment B showed slightly higher maximum deflections compared to Segment A. For the remaining lifespan of Segment B, there was almost zero increase in maximum deflection, except for the two instances where Segment B's critical steel reinforcing straps ruptured prematurely. Segment A maintained a constant increase in maximum deflection throughout its lifespan.

Overall, Segment B performed better in terms of deflection considering it maintained a near zero increase in slope in maximum deflection for the majority of its lifespan, except for the following three instances:

1) initial loading,
2) when Straps 2 and 3 ruptured, and
3) at failure.

7.2.5 Crack Width

On average, maximum crack width sizes in Segment B were smaller than those in Segment A. Visually, Segment B also had less wide spread cracking compared to Segment A. Fewer cracks in Segment B meant reduced spalling of concrete on the soffit of the deck, whereas Segment A had a greater proportion of spalling concrete, which lead to several reinforcing bars becoming exposed. Segment B consisted of smaller maximum crack widths and fewer cracks overall.

7.2.6 Reinforcement Strain

The steel reinforcement in Segment A generally sustained less maximum strain compared to the GFRP reinforcement in Segment B, at similar cycles. Furthermore, the GFRP in Segment B ruptured at only a fraction of the cycles which it took for the reinforcing steel in Segment A to rupture. These results are not overly surprising considering the GFRP in Segment B was only designed for crack control and not as a primary reinforcement. The GFRP in Segment B was also spaced at greater intervals compared to the reinforcing steel in Segment A. In addition, the modulus of elasticity of GFRP is significantly smaller than that of steel; therefore it is normal for GFRP to see higher strains compared to steel in similar loading and design situations. Nonetheless the steel reinforcement in Segment A outperformed the GFRP reinforcement in Segment B in that it had lower maximum strains and had a longer lifespan.

The real comparison in terms of strain is best done between the bottom transverse steel rebar in Segment A and the external steel straps in Segment B. Both of these reinforcements provided the main restraint

stiffness in the bridge decks that contributes to the arching action. The maximum strain level remained below 1,000 με in all four steel straps in Segment B, while the three steel bottom transverse rebars monitored in Segment A recorded maximum strains upwards of 2,000 με during the first cycle of loading; this signifies that the rebar in Segment A yielded only one cycle into loading. All three rebar being monitored in Segment A eventually ruptured at very early stages in the loading after reaching strains as high as 4,000-5,000 με. Two of the steel straps in Segment B ruptured before ever reaching yielding strain, signifying the straps ruptured prematurely due to a fatigue induced weakened cross-section at the shear stud weld locations. Overall, the external steel straps in Segment B outperformed the bottom internal transverse steel rebar in Segment A in terms of safe maximum strain levels and number of cycles achieved.

7.2.7 Concrete Strain

The maximum concrete strain in Segment B was nearly double that of Segment A, and the strain gauge either exceeded its capacity or became unglued at 8,011 cycles. The concrete strain gauge in Segment A continued functioning for the entire 2,000,000 cycles and showed satisfactory strain levels in the concrete throughout the entire period. Segment A was superior in terms of concrete strain in that it maintained safe maximum strain levels throughout its cyclic lifespan.

7.3 Serviceability and Ultimate Limit States Criteria Conclusion

7.3.1 Deflection Limits

According to ACI 440.1R-01, the maximum acceptable serviceability deflection limit for is 4.17 mm. Instrumentation in Segment A registered deflections of 0.03 mm and 0.48 mm at Serviceability Limit State (SLS) load of 110 kN; and 1.02 mm and 1.67 mm at Ultimate Limit State (ULS) load of 208 kN. Instrumentation in Segment B registered deflections of 0.8 mm and 0.6 mm at Serviceability Limit State (SLS) load of 110 kN; and 2.86 mm and 2.73 mm at Ultimate Limit State (ULS) load of 208 kN. Overall, the maximum deflections in Segment A were smaller than those of Segment B at respective limit state levels.

7.3.2 Crack Width Limits

According to CAN/CSA-S6-00/06 and the ACI 440.1R-01, the maximum acceptable serviceability crack width limit is 0.5 mm. Instrumentation in Segment A registered crack widths of 0.066 mm, 0.195 mm, and 0.066 mm at Serviceability Limit State (SLS) load of 110 kN; and 0.242 mm, 0.242 mm, and 0.206 mm at Ultimate Limit State (ULS) load of 208 kN. Instrumentation in Segment B registered crack widths of 0.121 mm, 0.039 mm, 0.021 mm, and 0.008 mm at Serviceability Limit State (SLS) load of 110 kN; and 1.067 mm, 0.040 mm, 0.044 mm, and 0.047 mm at Ultimate Limit State (ULS) load of 208 kN. For the most part, Segment B showed smaller crack widths; however, both segments recorded maximum crack widths well below the maximum serviceability crack width limit for all load states (except for one pi gauge in Segment B that recorded 1.067 mm at Ultimate Limit State (ULS) load of 208 kN).

7.3.3 Reinforcement Strain Limits

According to CAN/CSA-S6-00/06, the maximum acceptable steel reinforcement serviceability strain limit for Segment A is 1,200 με. The largest maximum steel reinforcement strain recorded at the Serviceability Limit State (SLS) design load of 110 kN was 154.15 με. According to CAN/CSA-S6-00/06, the yielding strain of steel reinforcement is 2,000 με. The largest maximum steel reinforcement strain recorded at the Ultimate Limit State (ULS) design load of 208 kN was 1,071.41 με. In both cases, the maximum steel reinforcement strains were well below the CAN/CSA-S6-00/06 requirements.

According to ISIS Canada Research Network Design Manual No. 3 (Reinforcing Concrete Structures with Fibre Reinforced Polymers), the maximum acceptable GFRP reinforcement serviceability strain limit for Segment B is 2,000 με. The largest maximum GFRP reinforcement strain recorded at the Serviceability Limit State (SLS) design load of 110 kN was 458.30 με. The ultimate GFRP reinforcement strain limit for the specific GFRP material used for this experiment is 18,500 με. The largest maximum GFRP reinforcement strain recorded at the Ultimate Limit State (ULS) design load of 208 kN was 3,012.33 με. In

both cases, the maximum GFRP reinforcement strains were below the ISIS Canada Research Network Design Manual No. 3 (Reinforcing Concrete Structures with Fibre Reinforced Polymers) requirements and the ultimate GFRP reinforcement strain limit, respectively.

According to CAN/CSA-S6-00/06, the maximum acceptable steel strap serviceability strain limit for Segment B is 1,200 με. The largest maximum steel strap strain recorded at the Serviceability Limit State (SLS) design load of 110 kN was 83.76 με. According to CAN/CSA-S6-00/06, the yielding strain of a steel strap is 2,000 με. The largest maximum steel strap strain recorded at the Ultimate Limit State (ULS) design load of 208 kN was 317.76 με. In both cases, the maximum steel strap strains were well below the CAN/CSA-S6-00/06 requirements.

Overall, Segment B demonstrated the most desirable maximum reinforcement strains at respective Serviceability (SLS) and Ultimate Limit States (ULS). This is most evident in the considerably low strains observed in the steel straps of Segment B at the respective limit states. Both segments recorded maximum reinforcement strains well below their respective maximum serviceability reinforcement stain and yielding limits, and therefore can be considered safe designs in terms of reinforcement strain limit criteria.

7.3.4 Concrete Strain Limits

According to CAN/CSA-S6-00/06, the ultimate compressive strain in concrete is 3,500 με. Instrumentation in Segment A registered a compressive concrete strain of 94.51 με at serviceability limit state load of 110 kN; and 245.14 με at ultimate limit state load 208 kN. Instrumentation in Segment B registered a compressive concrete strain of 367.61 με at serviceability limit state load of 110 kN; and 1,356.85 με at ultimate limit state load of 208 kN. Overall, the maximum concrete strains in Segment A were smaller than those of Segment B at respective limit state levels; however, both Segments recorded maximum concrete strains well below the ultimate compressive strain in concrete for all load states, and therefore can be considered safe designs in terms of deflection limit criteria.

7.4 Overall Conclusion

The following overall conclusions were drawn from this experimental program:

Relatively speaking,

- Segment A outperformed in endurance
- Segment B outperformed in durability
- Segments A and B were more or less equal in mode of failure
- Segment B outperformed in deflection
- Segment B outperformed in crack width size and spread
- Segment A outperformed in reinforcement strain; internal steel rebar versus internal GFRP reinforcement
- Segment B outperformed in reinforcement strain; external steel straps versus internal steel rebar
- Segment A outperformed in concrete strain

The remarkable endurance of the Segment B, even after it had been compromised with the loss of its two central steel straps, confirmed two important characteristics of a steel-free slab-on-girder bridge deck system:

1. There are other components that contribute to the arching action in addition to the exterior steel straps. This suggests that a significant portion of the restraint stiffness in the steel-free slab-on-girder bridge deck system comes from the composite action between the girders and the concrete deck.
2. Even after the two central steel reinforcing straps ruptured in Segment B, there remained a considerable amount of restraint stiffness in the structure to prevent the deck from failing

instantaneously. Instead, Segment B continued to resist loading for an extended period of time, which theoretically would have allowed for proper maintenance or rehabilitation to take place in the field before the deck actually failed.

Segment A did not fail under fatigue loading, and showed no immediate indication that it was going to fail, and therefore was statically loaded to failure under increasing load. Ultimately, this concludes that Segment A outperformed in fatigue life, however, Segment B showed many properties that were superior in nature as discussed previously in this chapter, and outperformed Segment A in many areas.

In a sense, the results captured from the testing program carried out on Segment B are more or less inconclusive due to the fact that Segment B showed clear signs of premature failure. Nonetheless, without a doubt, both Segments proved to be safe and reliable designs based on experimental results and accepted engineering principles, codes and standards. Conventional steel reinforced concrete bridge decks have long proven themselves as safe and reliable designs. With the results captured in this experimental program, and all those of past studies, it is recommended that steel-free concrete bridge deck systems also become widely considered as a viable option in all applicable bridge design situations.

References

AASHTO (1996). *American Association of State Highway and Transportation Officials, Standard Specifications for Highway Bridges.* Washington, D.C., U.S.A.

ACI (2001). *American Concrete Institute,* Guide *for the Design and Construction of Concrete Reinforced with FRP Bars.* Reported by ACI Committee 440. USA.

Bakht, B., and Agarwal, A.C., 1995. Deck Slab of Skew Girder Bridges. Canadian Journal of Civil Engineering, Vol. 22(3), pp. 514-523.

Bakht, B., and Lam, C., 2000. Behaviour of Transverse Confining System for Steel-Free Deck Slabs. ASCE Journal of Bridge Engineering, Vol, 5(2), pp. 139-147.

Bakht, B., and Markovic, S., 1986. Accounting for Internal Arching in Deck Slab Design. Journal of the Institution of Engineers (India), Vol. 67(CI1), pp. 18-25.

Bakht, B., and Mufti, A.A., 1998. Five Steel-Free Bridge Deck Slabs in Canada. Journal of the International Association for Bridge and Structural Engineering (IABSE), Vol. 8, No. 3, pp. 196-200.

Bakht, B., and Selvadurai, A.P.S., 1996. Performance of Steel-Free Deck Slabs under Simulated Rolling Wheel Loads. Second International Conference on Advanced Composite Materials in Bridges and Structures, held in Montreal, pp. 767-776.

CHBDC (2000). *Canadian Highway Bridge Design Code, Canadian Standards Association International.* Toronto, Ontario, Canada.

CHBDC (2006). *Canadian Highway Bridge Design Code, Canadian Standards Association International.* Toronto, Ontario, Canada.

CSA (1994). *Limit States Design for Steel Structures,* CSA/CAN-S16.1. Canadian Standards Association, Rexdale, Ontario, Canada.

Dorton, R.A., Holowka, M., and King, J.P.C., 1977. The Connestogo River Bridge Design and Testing. Canadian Journal of Civil Engineering, Vol. 4(1), pp. 18-39.

El-Ragaby, A., Salakawy, E., and Benmokrane, B., 2007. Fatigue Life Evaluation of Concrete Bridge Deck Slabs Reinforced with Glass FRP Composite Bars. ASCE Journal of Composites for Construction, pp. 258-268.

Hewitt, B.E., and Batchelor, B. de V., 1975. Punching Shear Strength of Restrained Slabs. ASCE Journal of the Structural Division, 101(ST9): 1827-1853.

ISIS Canada. (2007). *"Reinforcing Concrete Structures with Fibre Reinforced Polymers,"* ISIS-M03-07, Canadian Network of Centers of Excellence on Intelligent Sensing for Innovative Structures, University of Manitoba, Winnipeg, Manitoba.

Kinnunen, S., and Nylander, H., 1960. Punching of Concrete Slab without Shear Reinforcement. *Transactions of the Royal Institute of Technology, Stockholm, Sweden.* No. 158.

Limaye, N.V., 2004. *Steel Free Bridge Decks Under Cyclic Loading: A Study of Crack Propagation and Strength Degradation,* Doctor of Philosophy Thesis, DalTech-Dalhousie University, Halifax, Nova Scotia, Canada.

Matsui, S., Tokai, D., Higashiyama, H., and Mizukoshi, M., June 2001. Fatigue Durability of Fiber Reinforced Concrete Decks Under Running Wheel Load. Proceedings of the Third International Conference on Concrete Under Severe Conditions, CONSEC'01, June 18-20, 2001, Vancouver, British Columbia, Vol. 1, pp. 982-991.

Memon, A.H., 2005. *Comparative Fatigue Performance of Steel-Reinforced and Steel-Free Concrete Bridge Deck Slabs.* (Thesis)

Memon, A.H., Mufti, A.A., and Bakht, B., Crack Control with GFRP Bars in Steel-Free Concrete Deck Slab, CSCE Conference, June 4-7, 2003.

Mufti, A.A., Bakht, B., and Jaegar, L.G., 1991. Fibre RC Deck Slabs with Diminished Steel Reinforcement. Proceedings, IABSE Symposium held in Leningrad, pp. 388-389.

Mufti, A.A., Jaegar, L.G., Bakht, B., and Wegner, L.D., 1993. Experimental Investigation of FRC Deck Slabs without Internal Steel Reinforcement. Canadian Journal of Civil Engineering. 20 (3), pp. 398-406.

Mufti, A.A., Memon, A.H., Bakht, B., and Banthia, N., Fatigue Investigation of Steel-Free Bridge Deck Slabs, (ACI) ACI International, Special Publications, 2002.

Mufti, A.A., and Newhook, J.P., 1998. Punching Shear Strength of Restrained Concrete Bridge Deck Slabs. ACI Structures Journal, 95(4), pp. 375-381.

Mufti, A.A., Newhook, J.P., and Khanna, O.S., 1999. Predicting the Punching Behaviour of Reinforced Concrete Bridge Decks. Proceedings of the 1999 Canadian Society for Civil Engineering Annual Conference, Vol. I, pp. 325-334.

Mufti, A.A., Newhook, J.P., and Mahoney, M.A., 1999. Salmon River Bridge Field Assessment. Proceedings of the 1999 Canadian Society for Civil Engineering Annual Conference, Vol. I, pp. 51-61.

Newhook, J.P., 1997. *The Behaviour of Steel-Free Concrete Bridge Deck Slabs under Static Loading Conditions, Doctor of Philosophy Thesis,* Technical University of Nova Scotia, Halifax, Nova Scotia, Canada.

Newhook, J.P., and Mufti, A.A., 1996. A Reinforced Steel-Free Concrete Deck Slab for the Salmon River Bridge. Concrete International, Vol. 18(6), pp. 30-34.

Newhook, J.P., Mufti, A.A., and Wegner, L.D., 1995. Fibre-Reinforced Concrete Deck Slabs Without Internal Reinforcement – Half-Scale Testing and Mathematical Formulation, Research Report No. 1-1995, Technical University of Nova Scotia, Nova Scotia CAD/CAM Center.

OHBDC 1979. Ontario Highway Bridge Design Code, Ministry of Transportation of Ontario, Downsview, Ontario, Canada.

OHBDC 1992. Ontario Highway Bridge Design Code, Ministry of Transportation of Ontario, Downsview, Ontario, Canada.

Perdikaris, P.C., and Beim, S., 1988. RC Bridge Decks under Pulsating and Moving Load. ASCE, Journal of Structural Engineering, Vol, 114(3), pp. 591-607.7

Selvadurai, A.P.S., and Bakht, B., 1996. Simulation of Rolling Wheel Loads on an FRC Deck Slab. Proceedings, 2nd University-Industry Workshop of FRC held in Toronto, pp. 273-287.

Thorburn, J., and Mufti, A.A., 1995. Full-Scale Testing of Externally Reinforced FRC Bridge Decks On Steel Girders. Proceedings of the Canadian Society of Civil Engineering Annual Conference, Ottawa, ON, Vol. II, pp. 543-552.

Thorburn, J., and Mufti, A.A., 2001. Design Recommendations for Externally Restrained Highway Bridge Decks. Journal of Bridge Engineering, ASCE, pp. 243-249.

Wegner, L.D., and Mufti, A.A., 1994. Finite Element Investigation of Fibre-Reinforced Concrete Deck Slabs Without Internal Steel Reinforcement. Canadian Journal of Civil Engineering, Vol. 21, No.2, pp. 231-236.

Young, S.G., and Chang, S.P., 1998. Behaviour of Composite Bridge Decks Subjected to Static and Fatigue Loading. ACI Structural Journal, Vol. 95(3), pp. 249-258.